

Washington University in St. Louis

## Washington University Open Scholarship

---

All Theses and Dissertations (ETDs)

---

January 2010

### Frustrated Magnetism In Distorted Triangular Lattice Materials; & Extraordinary Electroconductance In Iii-V Metal Semiconductor Hybrid Structures

Jian Wu

*Washington University in St. Louis*

Follow this and additional works at: <https://openscholarship.wustl.edu/etd>

---

#### Recommended Citation

Wu, Jian, "Frustrated Magnetism In Distorted Triangular Lattice Materials; & Extraordinary Electroconductance In Iii-V Metal Semiconductor Hybrid Structures" (2010). *All Theses and Dissertations (ETDs)*. 384.

<https://openscholarship.wustl.edu/etd/384>

This Dissertation is brought to you for free and open access by Washington University Open Scholarship. It has been accepted for inclusion in All Theses and Dissertations (ETDs) by an authorized administrator of Washington University Open Scholarship. For more information, please contact [digital@wumail.wustl.edu](mailto:digital@wumail.wustl.edu).

WASHINGTON UNIVERSITY IN SAINT LOUIS

Department of Physics

Dissertation Examination Committee:

Stuart A. Solin, Chair

Philip Barlay

Victor Gruev

Zohar Nussinov

Alexander Seidel

Ralf Wessel

FRUSTRATED MAGNETISM IN DISTORTED TRIANGULAR LATTICE

MATERIALS;

& EXTRAORDINARY ELECTROCONDUCTANCE IN III-V METAL

SEMICONDUCTOR HYBRID STRUCTURES

by

Jian Wu

A dissertation presented to the  
Graduate School of Arts and Sciences  
of Washington University in St. Louis  
in partial fulfillment of the  
requirement of the degree  
of Doctor of Philosophy.

December 2010

Saint Louis, Missouri

Copyright by

Jian Wu

2010

This work is licensed under the Creative Commons  
Attribution-Noncommercial-Share Alike 3.0 Unported License.

To view a copy of this license, visit

<http://creativecommons.org/licenses/by-nc-sa/3.0/>

or send a letter to

Creative Commons,

171 Second Street, Suite 300,

San Francisco, California,

94105, USA.



# Abstract

## PART I:

We have synthesized a series of spin  $S = 1/2$  distorted triangular lattice materials  $\text{Cu}_{2(1-x)}\text{Zn}_{2x}(\text{OH})_3\text{NO}_3$  ( $0 \leq x \leq 0.65$ ) and their long chain alkyl carboxylic group intercalated derivatives,  $\text{Cu}_{2(1-x)}\text{Zn}_{2x}(\text{OH})_3(\text{C}_7\text{H}_{15}\text{COO}) \cdot m\text{H}_2\text{O}$  ( $0 \leq x \leq 0.29$ ). Their structural properties, magnetic properties and specific heat have been carefully studied in this thesis. We found that antiferromagnetic-type long-range order develops in all the nitrate group compounds below the Neel temperatures  $T_N$ , which decreases with increasing Zn content. For the organic long chain intercalated samples, the temperature dependence of magnetic susceptibility suggests that the low temperature state is a spin-glass-like phase, or more specifically, a cluster glass. Typical glassy behaviors are also observed in the time evolution of the remanent magnetization data. The specific heat data displays no visible peaks, which agrees with many spin-glass-like materials. Moreover, we found that the susceptibility follows power laws  $\chi \propto T^{-a}$  with two different exponents  $a$  in two successive regimes above the freezing temperature  $T_f$ , from which we propose that quantum Griffiths phases could exist in the intermediate temperature regime.

## PART II:

Extraordinary Electroconductance (EEC) belongs to a class of geometry driven interfacial effects EXX, where E = extraordinary and, to date, XX = magnetoresistance (MR), piezoconductance (PC) and optoconductance (OC). EEC is defined to be the percentage change in the device conductance with and without an external electric field. A well-designed EEC device can be used as a sensitive electric field sensor. In our study, a maximum 5.3% of EEC under an electric field of 2.5kV/cm at 300K has been obtained. The central part of our EEC devices is the vertical Au/Ti-GaAs metal-semiconductor Schottky interface. We found that the change in the sample conductance is due to the change in the depletion width under an external electric field. A two-layer analytical model was built to quantitatively explain the field dependence and geometrical dependence of the EEC effect. The predictions of this one adjustable parameter model agree very well the experimental results.

# Acknowledgements

First and foremost, I would like to thank Prof. Stuart A Solin for his guidance, inspiration and encouragement through the duration of my graduate study. His deep understanding of physics, optimistic attitude and strong determination always helped me to conquer the difficulties in my road of research.

I would like to thank Prof. Zohar Nussinov and Prof. Alexander Seidel, for their guidance and the collaboration on the frustrated magnetism project. I also would like to thank Dr. A. K. Gangopadhyay, for the collaboration on the magnetism project and teaching me to use many experimental tools.

I would like to thank Prof. James Schillings for allowing me to use the experimental facilities in his lab.

I would like to thank my collaborators, Dr. Yun Wang, Dr. A. K. M. Newaz, Fletcher Werner, Julia S. Wildeboer and Pongsakorn Kanjanaboos for their essential contributions to our projects. I also would like to thank other group members, Marla M Means, Dr. Yue Shao, Dr. Kristopher A. Wieland and Lauren Edge, for their warm help in the lab. With them, I could have a fruitful and joyful life during the last five years.

I would like to thank Wenli Bi, Dihui Lai and Ke Zhang for their help and useful discussion on experiments and computational work.

I also want to thank my friends at Washington University in St Louis, Lei Zhang, Wei Zhang (M), Xining Du, Tianyu Zhao, Wei Zhang (F), Wei Wang, Zhenyu Zhou, Shouting Huang and Dandan Hu. I really enjoy the wonderful time I share with them.

Lastly, and most importantly, my deepest gratitude goes to my father, Haishen Wu and my mother, Moli Zhang for their love, guidance and support throughout my whole life.

# Contents

<b>Abstract</b>	<b>iii</b>
<b>Acknowledgements</b>	<b>v</b>
<b>List of Figures</b>	<b>x</b>
<b>List of Tables</b>	<b>xiv</b>
<b>Preface</b>	<b>xv</b>
<b>Part I Frustrated Magnetism in distorted triangular lattice materials .....</b>	<b>1</b>
<b>1 Fundamentals of Magnetism.....</b>	<b>2</b>
<b>1.1 Atomic origin of magnetism.....</b>	<b>3</b>
1.1.1 Single electron .....	3
1.1.2 Many-electron System .....	7
<b>1.2 The inter-atomic interactions.....</b>	<b>10</b>
1.2.1 Dipole-dipole interaction .....	10
1.2.2 Exchange Interactions.....	11
1.2.3 Super-exchange.....	13
1.2.4 Dzyaloshinskii-Moriya interactions.....	15
<b>1.3 Magnetic structures .....</b>	<b>15</b>
1.3.1 Paramagnetism.....	15
1.3.2 Ferromagnetism and Antiferromagnetism .....	18
1.3.3 Frustration.....	21
1.3.4 Spin glass .....	26
<b>1.4 Experimental techniques.....</b>	<b>27</b>
1.4.1 DC susceptibility.....	29
1.4.2 AC susceptibility.....	29
<b>Bibliography .....</b>	<b>33</b>
<b>2 Magnetic Properties of <math>S = 1/2</math> quasi-triangular lattice materials:</b>	
<b><math>\text{Cu}_{2(1-x)}\text{Zn}_{2x}(\text{OH})_3\text{NO}_3/(\text{C}_7\text{H}_{15}\text{COO})\cdot m\text{H}_2\text{O}</math> .....</b>	<b>34</b>
<b>2.1 Abstract.....</b>	<b>34</b>
<b>2.2 Introduction.....</b>	<b>35</b>
<b>2.3 Experimental Details .....</b>	<b>38</b>
2.3.1 Sample Preparation.....	38
2.3.2 Measurement Details .....	39
<b>2.4 Results and Discussion.....</b>	<b>40</b>



2.4.1	Structure Analysis .....	40
2.4.2	Magnetic Susceptibility .....	45
2.4.3	Discussion .....	50
<b>2.5</b>	<b>Conclusions</b> .....	<b>52</b>
<b>2.6</b>	<b>Acknowledgements</b> .....	<b>53</b>
	<b>Bibliography</b> .....	<b>54</b>
<b>3</b>	<b>Spin glassiness and power law scaling in anisotropic triangular spin-1/2 antiferromagnets</b> .....	<b>57</b>
<b>3.1</b>	<b>Abstract</b> .....	<b>57</b>
<b>3.2</b>	<b>Introduction</b> .....	<b>58</b>
<b>3.3</b>	<b>Structure and preparation</b> .....	<b>61</b>
<b>3.4</b>	<b>DC and AC susceptibility</b> .....	<b>61</b>
<b>3.5</b>	<b>Time dependent magnetization</b> .....	<b>65</b>
<b>3.6</b>	<b>Specific heat</b> .....	<b>67</b>
<b>3.7</b>	<b>Discussion</b> .....	<b>70</b>
<b>3.8</b>	<b>Acknowledgements</b> .....	<b>72</b>
	<b>Bibliography</b> .....	<b>73</b>
<b>4</b>	<b>Magnetism and specific heat of 2D distorted triangular lattice materials: <math>\text{Cu}_{2(1-x)}\text{Zn}_{2x}(\text{OH})_3\text{NO}_3/(\text{C}_7\text{H}_{15}\text{COO})_m\text{H}_2\text{O}</math></b> .....	<b>75</b>
<b>4.1</b>	<b>Abstract</b> .....	<b>76</b>
<b>4.2</b>	<b>Introduction</b> .....	<b>76</b>
<b>4.3</b>	<b>Experiment</b> .....	<b>80</b>
4.3.1	Sample preparation .....	80
4.3.2	Experiment procedures .....	81
<b>4.4</b>	<b>Results and Discussion</b> .....	<b>82</b>
4.4.1	Crystal structure .....	83
4.4.2	Magnetic properties .....	84
4.4.3	Specific heat .....	94
<b>4.5</b>	<b>Conclusions</b> .....	<b>97</b>
<b>4.6</b>	<b>Acknowledgements</b> .....	<b>98</b>
	<b>Bibliography</b> .....	<b>99</b>
<b>5</b>	<b>Summary</b> .....	<b>101</b>
<b>Part II</b>	<b>Extraordinary Electroconductance in metal-semiconductor hybrid structures</b> .....	<b>104</b>
<b>6</b>	<b>Introduction to Extraordinary Effects</b> .....	<b>105</b>
<b>6.1</b>	<b>General principle</b> .....	<b>105</b>
<b>6.2</b>	<b>Extraordinary Magnetoresistance</b> .....	<b>107</b>
<b>6.3</b>	<b>Extraordinary Piezoconductance</b> .....	<b>110</b>
<b>6.4</b>	<b>Extraordinary Optoconductance</b> .....	<b>112</b>
<b>6.5</b>	<b>The Schottky Interface</b> .....	<b>112</b>

	<b>Bibliography .....</b>	<b>116</b>
<b>7</b>	<b>Extraordinary Electroconductance in Metal-Semiconductor Hybrid Structures .....</b>	<b>117</b>
	<b>7.1 Abstract.....</b>	<b>117</b>
	<b>7.2 Introduction.....</b>	<b>118</b>
	<b>7.3 Device Preparation.....</b>	<b>118</b>
	<b>7.4 Experiment .....</b>	<b>119</b>
	<b>7.5 A 2-Layer Analytical Model.....</b>	<b>123</b>
	<b>7.6 Conclusion .....</b>	<b>128</b>
	<b>7.7 Acknowledgements .....</b>	<b>128</b>
	<b>Bibliography .....</b>	<b>129</b>
<b>8</b>	<b>Transport measurements and analytical modeling of extraordinary electroconductance in Ti-GaAs metal-semiconductor hybrid structures .....</b>	<b>131</b>
	<b>8.1 Abstract.....</b>	<b>131</b>
	<b>8.2 Introduction.....</b>	<b>132</b>
	<b>8.3 Experimental Procedure .....</b>	<b>136</b>
	8.3.1 Sample design and fabrication.....	136
	8.3.2 Experimental setup.....	138
	<b>8.4 Experimental Observations.....</b>	<b>139</b>
	8.4.1 Schottky I-V.....	139
	8.4.2 EEC 4-lead Resistance under Direct Bias.....	143
	8.4.3 EEC 4-lead Resistance under External Electric Field and its Field Sensitivity .....	146
	<b>8.5 Analytical Modeling.....</b>	<b>149</b>
	8.5.1 Field Dependence of the Depletion Width.....	149
	8.5.2 The 2-layer Model.....	150
	<b>8.6 Comparison between EEC and JFET/MESFET .....</b>	<b>157</b>
	<b>8.7 Summary.....</b>	<b>158</b>
	<b>8.8 Acknowledgements .....</b>	<b>159</b>
	<b>Bibliography .....</b>	<b>160</b>
	<b><i>Curriculum Vitae.....</i></b>	<b>162</b>

# List of Figures

1.1	A circulating current loop .....	3
1.2	The dipole-dipole interaction between two magnetic moments .....	11
1.3	The super-exchange interactions in MnO .....	14
1.4	The randomly orientated moments in Paramagnet and each of them are fluctuating with time .....	16
1.5	(a) Ferromagnet; (b) Antiferromagnet; (c) Ferrimagnet; (d) Canted-antiferromagnet .....	19
1.6	Ising spins on a square lattice with competing interactions ( $J > 0$ ). The fourth spin is in a frustrated state .....	20
1.7	Frustrated plaquettes: (a) Ising spins on a (Left) triangular plaquette (Right) the tetrahedron. (b) The 2D Heisenberg (XY) spins on a triangle. The interactions between spins are antiferromagnetic .....	22
1.8	2D and 3D frustrated lattice .....	23
1.9	The experimental manifestation of frustration for the systems with antiferromagnetic interactions .....	25
1.10	(a) Frozen spin moments in spin glass (b) cluster glass .....	25
1.11	The magnetic flux of a dipole through a loop just above it .....	27
1.12	The schematic view of a vibrating sample magnetometer .....	28
1.13	A schematic view of a mutual inductance AC magnetometer .....	30
1.14	(a) The design of a mutual inductance AC magnetometer coil form (b) The real photo .....	31

1.15	The superconducting transition of a lead sample resolved by the home-made AC magnetometer shown in Fig. 1.14 .....	32
2.1	The left hand panel shows a perspective view of the basal unit of $\text{Cu}_2(\text{OH})_3\text{NO}_3$ . The right hand panel shows a c-axis view of the Cu layer and its planar unit cell (dark rectangle). $a_1 = 3.03 \text{ \AA} \neq a_2 = 3.17 \text{ \AA}$ .....	37
2.2	(a) The X-ray powder diffraction patterns of 7 different $\text{Cu}_{2(1-x)}\text{Zn}_{2x}(\text{OH})_3\text{NO}_3$ samples are shown from above to bottom: $x = 0, 0.13, 0.19, 0.29, 0.43, 0.55, 0.65$ . (b) A zoom in view of reflection peaks of $x = 0$ and $x = 0.29$ .....	41
2.3	Cell parameters of 7 nitrate samples obtained from the Le Bail analysis .....	42
2.4	The X-ray powder diffraction pattern of $\text{Cu}_{2(1-x)}\text{Zn}_{2x}(\text{OH})_3(\text{C}_7\text{H}_{15}\text{COO})\cdot\text{mH}_2\text{O}$ for $x = 0.19$ .....	43
2.5	Main panel: 2-100K temperature dependence of the DC magnetic susceptibility of 7 nitrate anion compounds $\text{Cu}_{2(1-x)}\text{Zn}_{2x}(\text{OH})_3\text{NO}_3$ .....	44
2.6	(a) The calculated effective moment and g factor for $0 \leq x \leq 0.65$ nitrate group samples. (b) The calculated Curie-Weiss temperature and Néel temperature for $0 \leq x \leq 0.65$ nitrate group samples.....	47
2.7	(a) 2-300K temperature dependence of DC susceptibility $\chi$ and its Reciprocal for $x = 0$ $\text{Cu}_{2(1-x)}\text{Zn}_{2x}(\text{OH})_3(\text{C}_7\text{H}_{15}\text{COO})\cdot\text{mH}_2\text{O}$ (b) 0-20K ZFC and FC susceptibility of $x = 0, 0.13$ and $0.19$ (c) A zoom-in view of ZFC and FC susceptibility for $x = 0.29$ .....	48
3.1	The structure of the CHN compound. a) A perspective view of the basal unit. b) c-axis view of the Cu layer and its planar unit cell (dark rectangle)..	60
3.2	$\ln(\chi)$ vs. $\ln(T)$ for DC susceptibility.....	62
3.3	AC susceptibility of $x = 0$ sample at $T = 10\text{K}$ .....	64
3.4	Isothermal remanent magnetization $M_{\text{ZFC}}(t)$ vs. $\log(t)$ at $5000 \text{ Oe}$ .....	66
3.5	Specific heat divided by temperature, for diluted CHN (a) and LOC (b) samples, with and without an applied magnetic field of $B = 5\text{T}$ .....	68

4.1	(a) The P2 <sub>1</sub> (4) crystal structure of Cu <sub>2(1-x)</sub> Zn <sub>2x</sub> (OH) <sub>3</sub> NO <sub>3</sub> (b) The c-axis view of the triangular Cu layers.....	78
4.2	The temperature dependence of magnetic susceptibility for 7 different Cu <sub>2(1-x)</sub> Zn <sub>2x</sub> (OH) <sub>3</sub> NO <sub>3</sub> samples .....	83
4.3	The log-log plot of temperature dependence of magnetic susceptibility for x = 0 long chain intercalated sample.....	85
4.4	(a) The difference between $\chi_{FC}$ and $\chi_{ZFC}$ in 2K < T < 20K (b) The difference between $\chi_{FC}$ and $\chi_{ZFC}$ at different fields.....	87
4.5	The log-log plot of $\chi_{ZFC}$ vs. temperature for 4 organic long chain intercalated samples .....	89
4.6	(a) The M(H) curves at T = 2K. (b) The M(H) curves at T = 10K.....	91
4.7	(a) The scaled quantity M <sub>ZFC</sub> (t)/M <sub>ZFC</sub> (0) measured under H = 5000Oe (b) The scaled quantity M <sub>ZFC</sub> (t)/M <sub>ZFC</sub> (0) of x = 0.29 measured under H = 500Oe, 5000Oe, 10000Oe and 20000Oe .....	93
4.8	The specific heat data for 6 nitrate group samples and 4 organic long chain intercalated samples .....	95
6.1	General principle of EXX effects. ....	106
6.2	(a) A schematic diagram of a homogeneous InSb vdP disk (radius $r_b$ ) with a embedded cylindrical Au inhomogeneity (radius $r_a$ ). (b) The observed RM EMR versus filling factor, $\alpha$ , of the above hybrid structure under different magnetic fields. ....	109
6.3	The strain dependence of the piezoconductance measured in metal-semiconductor hybrid structure with several different values of $\alpha$ at room temperature. ....	111
6.4	Main panels: The position (x) dependent voltage measurements, V <sub>23</sub> , of (a) an In-GaAs device and (b) a bare GaAs sample acquired under identical conditions at T = 15 K and with 20 mW of 476.5 nm laser radiation focused onto the sample surface.....	113

6.5	(a) The band diagram of isolated metal and semiconductor. (b) The band diagram of the metal and n-type semiconductor junction.....	115
7.1	(a) and (b) Schematics, respectively, of the top view and side view of an EEC device (c) Room temperature I – V characteristic of the Schottky interface.....	120
7.2	Room temperature 4-lead resistance under external electric field and the device sensitivity.....	122
7.3	The geometry dependence of the EEC effect .....	124
7.4	Theory and experiment comparison of the 4-lead resistance under reverse bias .....	126
8.1	A 3D schematic of the EEC Devices .....	134
8.2	A schematic diagram of the experimental setup.....	137
8.3	The room temperature I-V characteristic of the Schottky interface .....	140
8.4	The four lead resistance of devices with 60 $\mu\text{m}$ mesa radius and different values under a direct shunt bias voltage .....	145
8.5	(a) 4-point resistance of an EEC device measured with respect to an external electric field. Inset (b) shows the device sensitivity at the corresponding shunt biases. Panel (c)-EEC effects in four different devices with $\alpha = 1/16; 5/16; 10/16; 14/16$ .....	147
8.6	A 3D schematic of the 2 layer structure when the EEC device .....	151
8.7	The comparison of the curvature between the measured 4-point resistance of the EEC device of $\alpha = 7/16$ and the values calculated from the 2-layer analytical model for different $\beta$ s .....	153
8.8	The comparison between the 2-layer model and experiment .....	155

# List of Tables

1.1	The ground states of $\text{Cu}^{2+}$ and $\text{Zn}^{2+}$ predicted by Hund's rules .....	9
-----	--	---

# Preface

Some Chapters have been published or are submitted for publication, as follows:

- Chapter 2: Magnetic Properties of  $S = 1/2$  quasi-triangular lattice materials:  $\text{Cu}_{2(1-x)}\text{Zn}_{2x}(\text{OH})_3(\text{C}_7\text{H}_{15}\text{COO})\cdot m\text{H}_2\text{O}$ ,” Jian Wu, A. K. Gangopadhyay, P. Kanjanaboos and S. A. Solin, **J.Phys.:Condens. Matter.** 22, 334211 (2010).
- Chapter 3: Spin glassiness and power law scaling in anisotropic triangular spin-1/2 antiferromagnets, Jian Wu, Julia S. Wildeboer, Fletcher Werner, Alexander Seidel, Z. Nussinov, and S. A. Solin, submitted for Physical Review Letters.
- Chapter 7: Extraordinary electroconductance in metal-semiconductor hybrid structures, Yun Wang, A. K. M. Newaz, Jian Wu, S. A. Solin, V. R. Kavasseri, N. Jin, I. S. Ahmad, and I. Adesida, Applied Physics Letters, **92**, 262106 (2008).
- Chapter 8: Transport measurements and analytical modeling of extraordinary electroconductance in Ti-GaAs metal-semiconductor hybrid structures, A. K. M. Newaz, Yun Wang, **Jian Wu**, S. A. Solin, V. R. Kavasseri, I. S. Ahmen, and I. Adesida, Phys. Rev. B **79**, 195308 (2009).



# **Part I**

## **Frustrated Magnetism in distorted triangular lattice materials**

# Chapter 1

## Fundamentals of Magnetism

The discovery of magnetic materials and phenomena dates back to thousands of years ago according to the ancient Chinese and Greek literature. The first prominent application is the compass, which is considered as one of the major technological prerequisites for the Age of exploration starting in the 15<sup>th</sup> century. Since the rise of modern science, great efforts have been invested to systematically study Magnetism, which finally leads to Maxwell's unifying theory of electromagnetism. However, the microscopic basis of magnetism has never been established until the discovery of Quantum Theory, which provides an effective tool to describe small objects such as atoms, electrons, phonons and etc.

Magnetism is also a central subject of condensed matter physics. On one hand, the study of magnetism closely relates to the deep collective physics of a large ensemble of atoms and electrons. This is still considered as the stiffest puzzle in physics, even the laws of the individual atom and electron are quite clear. On the other hand, magnetic

materials play a very important role in modern electronics. Nowadays, the widely used magnetic devices such as flash drives and hard drives have made the storage and quick access of mass information possible.

This chapter is organized as follows. Section 1.1 discusses the atomic origin of local magnetic moments. Section 1.2 will review several important inter-atomic interactions. Several magnetic structures will be discussed in Section 1.3. Finally, in section 1.4, the experimental techniques used to measure DC and AC magnetic susceptibility will be covered.

## **1.1 Atomic origin of magnetism**

### **1.1.1 Single electron**

The magnetic moments of atoms and ions arise from two contributions: the circular motion of electrons and the intrinsic spin term. The atomic nuclei also have magnetic spins but their influence is only important in some special cases.

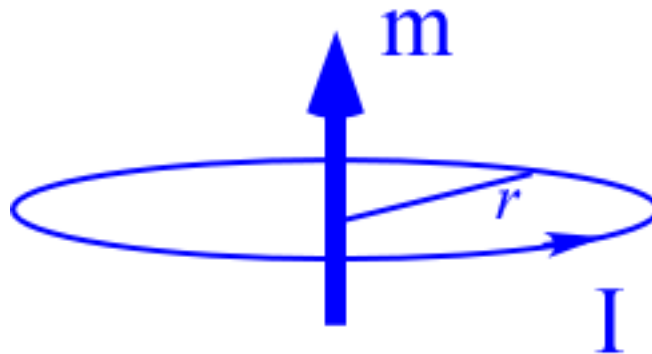


Figure 1.1 A circulating current loop

As shown in Fig 1.1, the classical picture of magnetic dipole is a circulating current loop, where the magnetic moment  $m = I\pi r^2$  (SI unit). If the current is actually originated from a moving particle with charge  $q$ , velocity  $v$  and mass  $M$ , then the magnetic moment can be expressed as

$$m = \frac{q}{2M} Mrv = \frac{q}{2M} L \quad (1.1)$$

in which the angular momentum  $L$  is directly related to the magnetic moment. The magnetic moment of an electron in an atom is more or less similar to this picture. But we should resort to Quantum Mechanics to correctly determine the orbital angular momentum of an electron.

Let us consider the Hydrogen-like atom with only one outer shell electron. The influence of the nuclei and other inner shell electrons is simplified into a central Coulomb potential  $V = -\frac{Ze^2}{4\pi\epsilon_0 r}$ . Thus, the electron wave function will be governed by the

Schrödinger Equation,

$$H\psi = \left(-\frac{\hbar^2}{2m_e}\nabla^2 + V\right)\psi = E\psi \quad (1.2)$$

where the  $m_e$  is the mass of electron. In spherical coordinates, the operator is

$$\nabla^2 = \frac{1}{r} \frac{\partial^2}{\partial r^2} r + \frac{1}{r^2} \left[ \frac{1}{\sin^2 \theta} \frac{\partial^2}{\partial \phi^2} + \frac{1}{\sin \theta} \frac{\partial}{\partial \theta} \left( \sin \theta \frac{\partial}{\partial \theta} \right) \right] \quad (1.3)$$

As discussed in many classical Quantum Mechanics text books [1], the bound state solution to Eqn (1.2) can be separated into radial term and angular term as

$$\psi_{nlm_l}(r, \theta, \phi) = R_{nl}(r) Y_{lm_l}(\theta, \phi) \quad (1.4)$$

The numbers  $n$ ,  $l$  and  $m_l$  are principal, angular momentum and magnetic quantum numbers, respectively. A set of three quantum numbers uniquely specifies one spatial wave function. The quantum numbers are integers that comply with the following rules:

$$\begin{aligned} n &= 1, 2, 3, \dots \\ l &= 0, 1, 2, \dots, n-1 \\ m_l &= -l, -l+1, \dots, l-1, l \end{aligned} \quad (1.5)$$

To investigate the orbital angular momentum of the above wave functions, we should introduce 2 new operators,

$$L^2 \equiv -\hbar^2 \left\{ \frac{1}{\sin \theta} \frac{\partial}{\partial \theta} \left( \sin \theta \frac{\partial}{\partial \theta} \right) + \frac{1}{\sin^2 \theta} \frac{\partial^2}{\partial \phi^2} \right\} \quad (1.6)$$

and

$$L_z = \frac{\hbar}{i} \frac{\partial}{\partial \phi} \quad (1.7)$$

The wave functions  $\psi_{nlm_l}(r, \theta, \phi)$  are also their eigen functions:

$$L^2 \psi_{nlm_l}(r, \theta, \phi) = l(l+1)\hbar^2 \psi_{nlm_l}(r, \theta, \phi) \quad (1.8)$$

$$L_z \psi_{nlm_l}(r, \theta, \phi) = m_l \psi_{nlm_l}(r, \theta, \phi) \quad (1.9)$$

The magnitude of orbital angular moment  $|L|$  is then given by

$$|L| = \sqrt{l(l+1)}\hbar \quad (1.10)$$

The projection of orbital angular momentum with respect to the z direction of the spherical coordinate is  $m_l \hbar$ . In this case, the choice of the z direction is arbitrary. However, if an external magnetic field is switched on and the field direction is set to z, the different  $m_l$  means different energy levels. That is why they are called magnetic

quantum numbers. Substituting Eqn. (1.10) into Eqn. (1.1), we will obtain the orbital contribution to magnetic moment of an electron in the wave function  $\psi_{nlm_l}(r, \theta, \phi)$ ,

$$m = -\sqrt{l(l+1)} \frac{e\hbar}{2m_e} = -\sqrt{l(l+1)}\mu_B \quad (1.11)$$

where  $\mu_B = \frac{e\hbar}{2m_e}$  is Bohr magneton. In some cases, the more useful quantity is the projection of magnetic moment with respect to z direction (field direction),  $m_z = m_l\mu_B$ .

In addition to 3 quantum numbers describing the spatial wave function, each electron also has the intrinsic property called spin. The spin of the electron gives rise to a spin angular momentum,

$$|S| = \sqrt{s(s+1)}\hbar \quad (1.12)$$

in which s is spin quantum number, and is always equal to 1/2 for electrons. One more quantum number  $m_s (= \pm \frac{1}{2})$  is required to give the projection of spin angular momentum with respect to the z direction. However, unlike the orbital angular moment case, the spin magnetic moment with respect to the z direction is

$$m = -g_s m_s \mu_B \quad (1.13)$$

where the  $g_s$  is a constant called Landé g-factor. The g-factor has the value 2 for the electron spin and 1 for the orbital angular momentum.

The spin and orbital magnetic moment of electrons are actually coupled by so called spin-orbit interactions. If the spin-orbit terms are included in Eqn. (1.2), then the total angular momentum instead of spin or orbital angular moment becomes good quantum

number. The total angular momentum quantum number  $J$  and its projection on the  $z$  axis is determined by

$$\begin{aligned} J &= L + S, L + S - 1, \dots, |L - S| \\ M_J &= -J, -J + 1, \dots, J - 1, J \end{aligned} \quad (1.14).$$

The projection of the magnetic moment on the  $z$  axis is

$$m = -gm_J\mu_B \quad (1.15)$$

where the Landé  $g$ -factor  $g$  is [2],

$$g = 1 + \frac{J(J+1) + S(S+1) - L(L+1)}{2J(J+1)} \quad (1.16)$$

## 1.1.2 Many-electron System

The extension of the above method Many-electron system is not trivial. In principle, we could solve the many-electron Schrödinger Equation to obtain the total angular momentum of any other atoms or ions. However, it is impractical to solve these equations analytically. The compromising methods people have taken are either introducing approximations to build an affordable theory or summarizing a set of rules based on experimental results.

One of most used approximation is called the “Hartree-Fock method” [3]. The total Hamiltonian can be written as in the sum of several one-electron Hamiltonians,

$$H = \sum_i H_i = -\frac{\hbar^2}{2m} \sum_i \nabla_i^2 + \sum_i \frac{Ze^2}{4\pi\epsilon_0 r_i} + \sum_i V_i \quad (1.17)$$

The influence of other electrons is approximated by static spherical symmetrical Coulomb potentials  $V_i$ . At this moment, the spin orbit and other interaction are

neglected. Usually an iterative procedure will be applied: The wave function solved using above Hamiltonian will be used to improve the form of potentials  $V_i$ . These steps are repeated until the minimal energy solution is obtained.

In principle, we could apply the above Hartree-Fock method and find out  $N$  lowest energy wave functions,  $\Psi_1(\mathbf{r},\sigma), \Psi_2(\mathbf{r},\sigma), \dots, \Psi_N(\mathbf{r},\sigma)$ , where  $\sigma$  is the spin coordinate. For simplicity, we assume that these  $N$  states are not degenerate. To construct a correct ground state wave function, the Pauli Exclusion Principle should be considered, which requires that total wave function of electrons must be anti-symmetrical. The correct wave function can be expressed as a determinant [3],

$$\Psi = \begin{vmatrix} \Psi_1(r_1, \sigma_1) & \Psi_2(r_1, \sigma_1) & \dots & \Psi_N(r_1, \sigma_1) \\ \Psi_1(r_2, \sigma_2) & \Psi_2(r_2, \sigma_2) & \dots & \Psi_N(r_2, \sigma_2) \\ \dots & \dots & \dots & \dots \\ \dots & \dots & \dots & \dots \\ \Psi_1(r_N, \sigma_N) & \Psi_2(r_N, \sigma_N) & \dots & \Psi_N(r_N, \sigma_N) \end{vmatrix} \quad (1.18)$$

The above theoretical treatment is successful when applied to the lightest atoms, such as Helium. However, the theorem fails to explain electron configurations of the heavier atoms because it is too simplified. Fortunately, a group of three Hund's rules, which are based on atomic spectroscopic experiments, has been discovered and used to determine the ground state configurations for many-electron atoms. The 3 Hund's rules are:

1. **First rule:** The electron configurations with the largest total spin quantum number  $S$  lie lowest in energy.
2. **Second rule:** For a given spin arrangement selected by first rule, the ground states maximize the value of the total angular momentum quantum number  $L$ .



3. **Third rule:** For the  $L$  and  $S$  values selected by the first and second rules, the total angular momentum quantum number favors the minimum value  $|L-S|$  for less than half filled shells and the maximum value  $L+S$  for more than half filled shells.

The detailed discussion can be found in ref. 4. The basic assumption of Hund's rule is that the spin-orbit interactions are small compared to spin-spin interactions and orbit-orbit interactions. In this thesis, the most discussed ions are  $\text{Cu}^{2+}$  and  $\text{Zn}^{2+}$ . According to Hund's rules, the ground states of them are listed in Table 1.1.

Name	$l_z=2$	1	0	-1	-2	S	L	J	Symbol
$\text{Cu}^{2+}$	$\uparrow\downarrow$	$\uparrow\downarrow$	$\uparrow\downarrow$	$\uparrow\downarrow$	$\uparrow$	1/2	2	5/2	$^2D_{5/2}$
$\text{Zn}^{2+}$	$\uparrow\downarrow$	$\uparrow\downarrow$	$\uparrow\downarrow$	$\uparrow\downarrow$	$\uparrow\downarrow$	0	0	0	$^1S_0$

Table 1.1 The ground states of  $\text{Cu}^{2+}$  and  $\text{Zn}^{2+}$  predicted by Hund's rules (After ref. 4).

The  $\text{Zn}^{2+}$  has a closed shell configuration and thus possesses a total angular momentum  $J = 0$ . As a result, the ground state of  $\text{Zn}^{2+}$  is nonmagnetic. However, the total angular momentum  $J = 5/2$  of  $\text{Cu}^{2+}$  doesn't agree with experimental results. Instead, the measured value of  $J$  is close to 1/2. It seems that the total orbital angular momentum takes the value 0. This phenomenon is well known as "the quenching of orbital angular momentum", which is a common effect of all iron (3d) group ions with a strong crystal field effect. The reason is that the crystal fields of neighboring ions are strong enough to lift the degeneracy of the total orbital momentum L-multiplet. In addition, a closer observation would tell us that the real angular momentum of  $\text{Cu}^{2+}$   $J$  is always slightly

larger than 1/2. (See Chapter 2). This is due to the spin-orbit interaction, which will re-introduce a small component of orbital angular momentum in spite of the quenching.

In this section, we discussed the localized magnetism of an isolated atom or ion. The local magnetic moment is due to angular momentum, including spin and orbital angular momentum. The addition of individual angular momentum to total angular momentum  $J$  depends on the relative strength of spin-spin, orbit-orbit and spin-orbit interactions. The magnetic moment associating with  $J$  is  $m = gm_J\mu_B$ , in which the Landé  $g$ -factor depends on both intra-and inter-atomic interactions. In insulating solids, the angular momentum of one individual ion or atom can be roughly treated as a vector. It is important to note that the inter-atomic interactions and external fields determine the relative orientations of neighboring atoms or ions' angular momentum.

## 1.2 The inter-atomic interactions

The atoms and ions in the solid state are not isolated. Instead they interact with each other through dipole-dipole, exchange, super-exchange and other long-range interactions. In the following subsections, we will introduce three of them.

### 1.2.1 Dipole-dipole interaction

The long-range dipole-dipole interaction is a purely magnetic interaction which can be well understood in the context of classical electromagnetism. For two local magnetic moments, the interaction energy between them is,

$$E = \frac{\mu_0}{4\pi r_{ij}^3} \left( \mathbf{m}_1 \cdot \mathbf{m}_2 - 3 \frac{(\mathbf{m}_1 \cdot \mathbf{r}_{ij})(\mathbf{m}_2 \cdot \mathbf{r}_{ij})}{r_{ij}^2} \right) \quad (1.19)$$

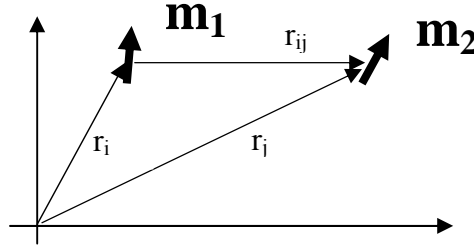


Figure 1.2 The dipole-dipole interaction between two magnetic moments

The energy  $E$  decreases as  $1/r_{ij}^3$ , and will die out rapidly. Let us examine a simple case in which  $\mathbf{m}_1$  and  $\mathbf{m}_2$  are parallel to each other and have the value of 1 Bohr magneton. Assume that they are 2 Å apart from each other which is a pretty common value in a solid. Then the energy  $E$  will be much less than  $10^{-4}$  eV, which is also much smaller than the intra-atomic interaction energy scale. Thus, this effect is only important when the temperature is very low ( $< 1\text{K}$ ). But the magnetic ordering has been found to occur at much higher temperatures ( $> 300\text{K}$ ) in many materials, in which the exchange interactions originating from quantum effects effectively couple the neighboring ions.

## 1.2.2 Exchange Interactions

The exchange interaction is caused by the interplay of the Pauli Exclusion Principle and Coulomb interaction. The simplest model to apply to the exchange interaction is a two-electron model. We can write a Hamiltonian with only electron-electron and electron-nucleus Coulomb interactions,

$$H = -\frac{\hbar}{2m_e}(\nabla_1^2 + \nabla_2^2) - \frac{e^2}{4\pi\epsilon_0}\left(\frac{1}{r_1} + \frac{1}{r_2}\right) + V = H_1 + H_2 + V \quad (1.20)$$

Where

$$H_i = -\frac{\hbar}{2m_e}\nabla_i^2 - \frac{e^2}{4\pi\epsilon_0 r_i} \quad (1.21)$$

and the potential  $V$  includes all the other Coulomb interactions. For simplicity, we only consider the two lowest energy single-electron spatial wave functions of  $H_i$ ,  $\psi_a(r_1)$  and  $\psi_b(r_2)$ . According to the Pauli Exclusion Principle, there are only two possibilities for the total wave function: a symmetric spatial wave function with a singlet spin state (anti-symmetric) or an anti-symmetric spatial wave function with a triplet spin state (symmetric). The total wave functions are [5]:

$$\psi_S = \frac{1}{\sqrt{2}}(\psi_a(r_1)\psi_b(r_2) + \psi_a(r_2)\psi_b(r_1))\chi_S \quad (1.22)$$

$$\psi_T = \frac{1}{\sqrt{2}}(\psi_a(r_1)\psi_b(r_2) - \psi_a(r_2)\psi_b(r_1))\chi_T \quad (1.23)$$

Where the  $\chi_S$  and  $\chi_T$  are singlet and triplet spin states. The energies of the two states are  $E_S$  and  $E_T$ , respectively. If we limit our considerations to the above four states, an effective Hamiltonian can be written as [5]

$$H = \frac{1}{4}(E_S + E_T) - (E_S - E_T)\mathbf{S}_1 \cdot \mathbf{S}_2 \quad (1.24)$$

By defining the zero point, the Hamiltonian can further simplified as

$$H = -J\mathbf{S}_1 \cdot \mathbf{S}_2 \quad (1.25)$$

where the energy splitting between singlet and triplet state is  $J = E_S - E_T$ . From Eqn. (1.25), we can clearly see a spin-dependent form although there is no spin-dependent

term in the original Hamiltonian (Eqn. (1.20)). The wave functions  $\psi_a(r_1)$  and  $\psi_b(r_2)$  could be two single-electron states in one atom or two neighboring atoms. If it is the latter case, this spin-dependent Hamiltonian means an inter-atomic interaction. If  $J > 0$  ( $< 0$ ), the triplet (singlet) states are energetically favored. The Hamiltonian (1.25) can be generalized to many-electron systems, in which  $S_1$  and  $S_2$  will be given new physical meanings, atomic spins [6]. If the above scheme is applied to any pairs of atomic spins in a solid, we could arrive at the so-called Heisenberg model Hamiltonian,

$$H = -\sum_{ij} J_{ij} \mathbf{S}_i \cdot \mathbf{S}_j \quad (1.26)$$

which is the starting point for many theoretical works.

### 1.2.3 Super-exchange

The exchange interactions described in the previous section are also called direct exchange because they are the consequence of direct Coulomb interactions between electrons from neighboring ions. However, in many materials, such as transition metal oxides MeO, the magnetic ions are well separated by a nonmagnetic ion (such as  $O^{2-}$ ). It is impossible to have a direct exchange interaction that is big enough to account for magnetic order. In these materials, an indirect exchange arises, which is mediated by the  $O^{2-}$  in between the metal ions. One example of super-exchange interactions is shown in Fig. 1.3 for Mn-O-Mn.

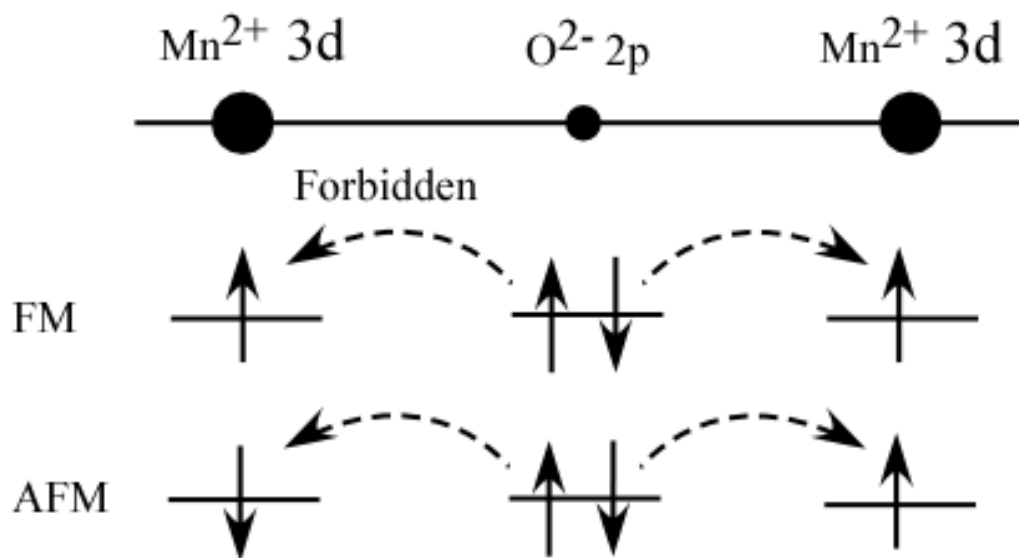


Figure. 1.3 The super-exchange interactions in MnO

The  $\text{Mn}^{2+}$  ion has 5 half filled 3d orbitals. The 5 electrons all have the same spin orientation due to Hund's first rule. The center  $\text{O}^{2-}$  has fully occupied 2p orbitals with two antiparallel electron spins. The  $\text{O}^{2-}$  2p electrons can spread into two neighboring  $\text{Mn}^{2+}$ 's 3d orbitals to lower the kinetic energy. However, if the two neighboring  $\text{Mn}^{2+}$ 's atomic spins are parallel, one of the above spreading is forbidden by Pauli Exclusion Principle. So in this case, the antiparallel configuration is favored energetically. The parallel configurations are also possible in some other situations.

The super-exchange interaction can also be described by a Heisenberg Hamiltonian as (1.26). The sign and strength of the coupling constant,  $J$ , are very sensitive to the Me-O-Me bond length and bond angle. The bond angle dependence of super-exchange is given by the well-known Goodenough-Kanamori-Anderson rules [7]: Me-O-Me bonds of  $180^\circ$  and  $90^\circ$  lead to strong antiferromagnetic and ferromagnetic interactions while the intermediate angle case is ambiguous.

## 1.2.4 Dzyaloshinskii-Moriya interactions

In some low symmetry crystals, an anisotropic exchange interaction, Dzyaloshinskii-Moriya (DM), could arise from the interplay of the spin-orbit interaction and the super-exchange interaction [8]. The DM interaction is described by the Hamiltonian,

$$H = -\mathbf{D} \cdot (\mathbf{S}_i \times \mathbf{S}_j) \quad (1.27)$$

where  $\mathbf{D}$  is a vector along a high-symmetry axis [6]. The DM interaction would cant two antiparallel spins although it is usually about two orders of magnitude less than the super-exchange interaction.

# 1.3 Magnetic structures

In the previous section, we have discussed several inter-atomic interactions, which would finally lead to various magnetic structures. The search for the magnetic ground states of various materials and excitations at finite temperature is always one of the central themes of condensed matter physics. In this section, I will discuss the paramagnetism, which exists in high temperature states for most magnetic materials, and the ferromagnetism, antiferromagnetism and spin glass states.

## 1.3.1 Paramagnetism

As discussed in section 1.1, many atoms or ions possess a permanent magnetic moment. There are many good examples in transition metal oxides, such as CuO, NiO, CoO and

etc. Although the magnetic moments are coupled by various inter-atomic interactions, the thermal energy could cause random alignments of magnetic moments when the temperature  $T$  is high enough. If an external magnetic field  $H$  is applied, a small magnetic susceptibility  $\chi = M/H$  will be observed. At temperature high enough, the magnetization exhibits  $1/T$  temperature dependence.

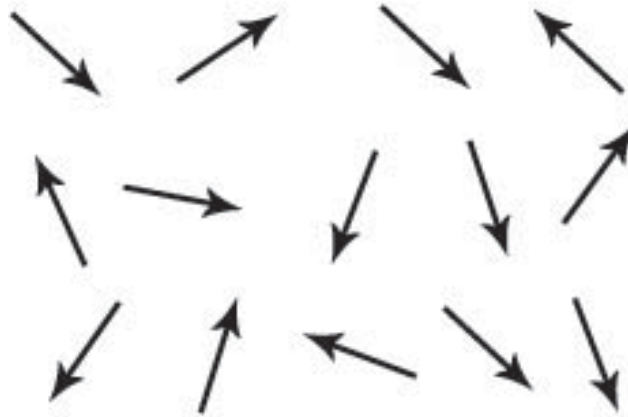


Figure 1.4 The randomly orientated moments in a Paramagnet and each of them are fluctuating with time.

Using the knowledge of Statistical Mechanics, the temperature dependence of the susceptibility can be explained. Let us consider  $N$  non-interacting ions with total magnetic momentum  $J$ . If an external magnetic field  $B$  is applied, then there are  $2J+1$  possible energy levels (SI units),

$$E = \mu_0 \mu_B g m_J H = \lambda m_J H, \quad \lambda = \mu_0 \mu_B g \quad (1.28)$$

where  $m_J = -J, -J+1, \dots, J-1, J$ . The partition function for this system is



$$Z = \sum_{m_J=-J}^J \exp(-\beta \lambda m_J H) \quad (1.29)$$

Where  $\beta = 1/kT$ . According to Statistical Mechanics, the magnetization  $M$  for  $N$  ions is given by

$$M = -\frac{N}{\mu_0 \beta} \frac{\partial \ln Z}{\partial H} = N \lambda J B_J(\beta \lambda J H) \quad (1.30)$$

where the Brillouin function  $B_J$  is

$$B_J(x) = \frac{2J+1}{2J} \coth \frac{2J+1}{2J} x - \frac{1}{2J} \coth \frac{1}{2J} x \quad (1.31)$$

When  $\lambda H \ll kT$ , the molar susceptibility is given by [4]

$$\chi_m = N_A \frac{\mu_0 (g \mu_B)^2}{3} \frac{J(J+1)}{k_B T} \quad (1.32)$$

This is well-known Curie-Law. In real applications, sometimes we use the effective magnetic moment

$$\mu_{eff} = g[J(J+1)]^{1/2} \mu_B \quad (1.33)$$

which is often expressed in unit of the Bohr magneton  $\mu_B$ . Experimentally we could fit the temperature dependence of the susceptibility to  $\chi_m = C/T$ , where the Curie constant  $C$  is

$$C = N_A \frac{\mu_0 (\mu_{eff})^2}{3k_B} \quad (1.34)$$

From the Curie constant, the effective moment can be estimated. In many cases, we will use CGS units instead of SI units. If  $\chi_m$  is given in the units of emu/Oe-mol, there is a useful empirical expression for the effective moment

$$\mu_{\text{eff}} = 2.828\sqrt{C}\mu_B \quad (1.35)$$

## 1.3.2 Ferromagnetism and Antiferromagnetism

If the ions in a solid are strongly coupled by the inter-atomic interactions discussed in section 1.2, various magnetic ordered structures could form at low temperature. Let us consider a system, in which the interactions between magnetic ions are described by the nearest neighbor Heisenberg Hamiltonian,

$$H = -\sum_{ij} J_{ij} \mathbf{S}_i \cdot \mathbf{S}_j \quad (1.36)$$

when  $J_{ij} > 0$  for all cases, the neighboring spins tend to align parallel to each other. At zero temperature, all the atomic spins in the solid are aligned parallel as shown in Fig. 1.5(a). This material is named a ferromagnet. If the coupling constant  $J_{ij} < 0$  for all cases, the atomic spins are aligned antiparallel as in shown in Fig. 1.5(b). This is so-called antiferromagnet.

The ferromagnet exhibits spontaneous magnetization at a critical temperature,  $T_C$  (Curie temperature) even without an external magnetic field. One alternative view point of an antiferromagnet is that it consists of two interpenetrating sub-lattices. Both of them are spontaneously magnetized but in opposite directions below a so-called Neel temperature,  $T_N$ . The net magnetization is 0 due to the cancellation of the two sub-lattice magnetizations. If the external magnetic field is applied, the susceptibility follows the Curie-Weiss Law above the critical temperature  $T_C$  ( $T_N$ ),

$$\chi = \frac{C}{T - \Theta_{cw}} \quad (1.37)$$

where the Curie-Weiss temperature  $\Theta_{cw}$  is related to coupling constants by the mean field theory [4],

$$|\Theta_{cw}| = S(S+1)z|J|/3k_B \quad (1.38)$$

where  $z$  denotes the number of nearest neighbors one ion has. For the ferromagnet (antiferromagnet),  $\Theta_{cw} > 0 (< 0)$ .

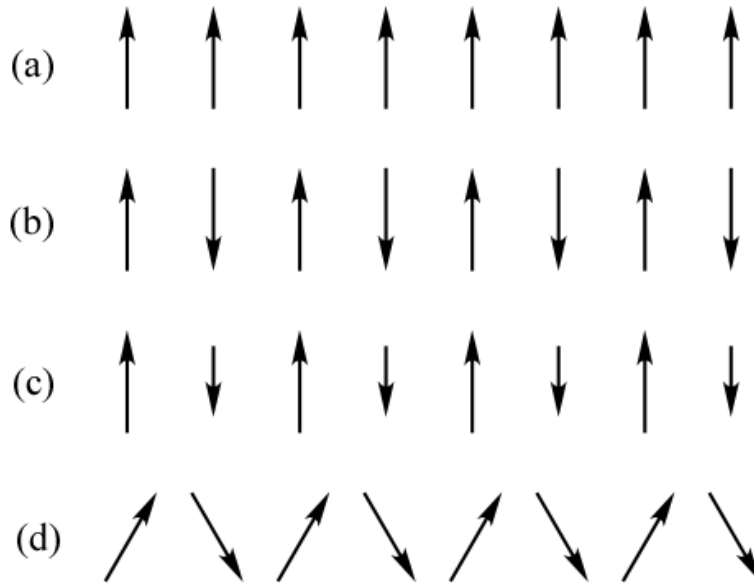


Figure 1.5 (a) Ferromagnet; (b) Antiferromagnet; (c) Ferrimagnet; (d) Canted-antiferromagnet

In an ideal antiferromagnet, the magnetization at  $T=0\text{K}$  must be 0. In real materials, there are some non-ideal “antiferromagnets”. As shown in Fig. 1.6(c), in a ferrimagnet, the magnitudes of two neighboring spin moments are not equal, which results in a net spontaneous magnetization. Another case is that two adjacent spin moments are canted from their original antiparallel alignments as shown in Fig. 1.6(d). This is called a canted-antiferromagnet in which the cancellation of two sub-lattices’ magnetization is also incomplete.

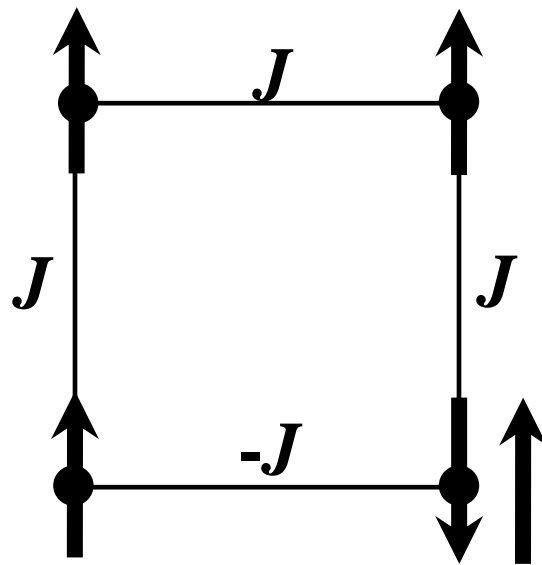


Figure 1.6 Ising spins on a square lattice with competing interactions ( $J > 0$ ). The fourth spin is in a frustrated state.

### 1.3.3 Frustration

In the above ferromagnets and antiferromagnets, the lowest energy configuration is achieved by the parallel or antiparallel alignments of neighboring spins. However, in some situations, it is impossible to minimize the energy for all the interactions between neighboring pairs of atomic moments. This phenomenon is called frustration. One origin of frustration is competing interactions. One example of that is shown in Fig. 1.6. Four identical Ising spins are arranged on a square lattice in which 3 bonds are ferromagnetic ( $J>0$ ) and the fourth one is antiferromagnetic ( $-J<0$ ). No matter how you arrange the fourth spin, there is always one unsatisfied bond.

Geometrical frustration is another class of frustration effects, which arises from the contradiction between long-range magnetic order and lattice geometry. Geometrical frustration usually occurs in triangle-based geometries with antiferromagnetically coupled Ising spins. In Fig 1.7(a) left, only two of the three bonds can be satisfied simultaneously for the triangular lattice. As shown in Fig 1.7(a) right, the 3D building block of frustrated lattices is a tetrahedron, which is made up by 4 edge-sharing triangles. In this case, two of four bonds can be satisfied. Various 2D and 3D frustrated lattices, based on the triangle and tetrahedron blocks, have already been found (See Fig. 1.8). The 2D examples are the triangular and Kagomé lattices. The Kagomé lattice is built from corner-sharing triangles. Fig. 1.8 also shows the 3D analogue of triangular and Kagome lattice, face-centered-cubic (FCC) and pyroclore lattice, which are built from edge-sharing and corner-sharing tetrahedrons, respectively.

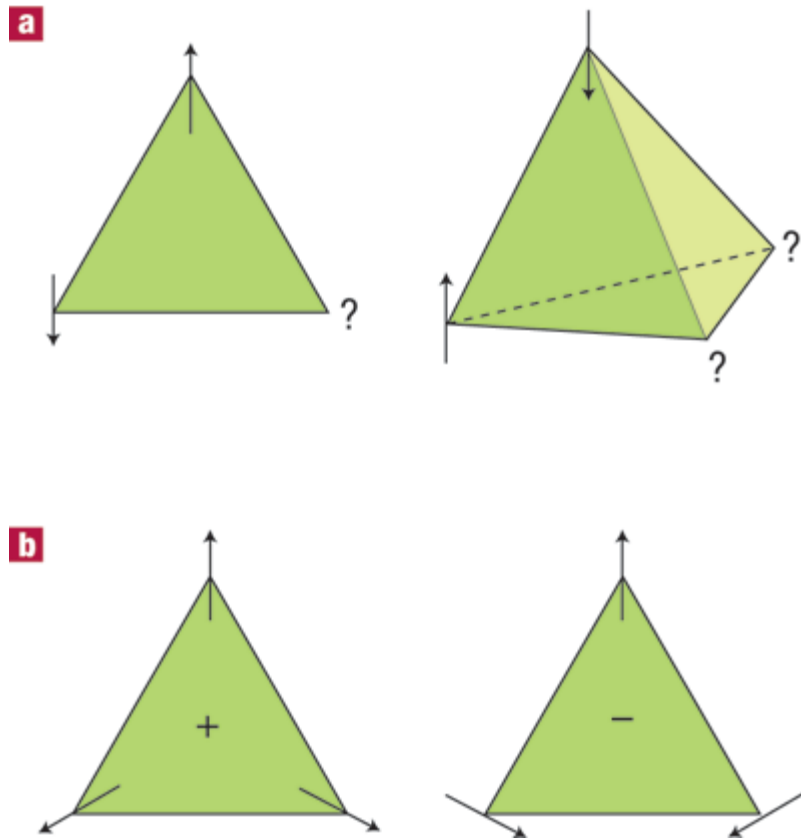


Figure 1.7 Frustrated plaquettes: (a) Ising spins on a (Left) triangular plaquette (Right) the tetrahedron. (b) The 2D Heisenberg (XY) spins on a triangle. The interactions between spins are antiferromagnetic (After ref [9]).

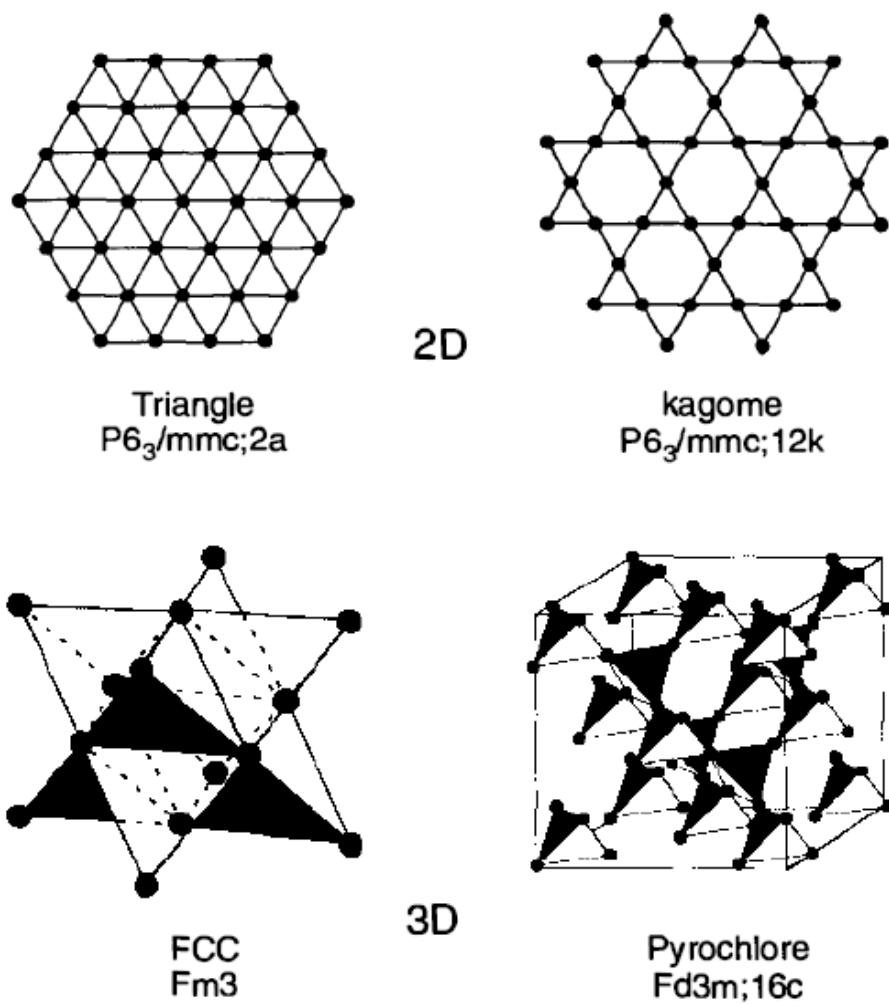


Figure 1.8 2D and 3D frustrated lattice (After ref. [10]).

If the Ising spins on a triangle are replaced by the XY spins, there are two fold degenerate ground states, in which the spins are arranged  $120^\circ$  relative to neighboring spins, as shown in Fig. 1.7(b). The two states distinguish themselves from each other by their different chirality. For the triangular lattice, this chirality extends to the whole lattice, which results in a long-range ordered ground state with 3 sub-lattices (so called Neel-type states). However, the Kagomé lattice is still frustrated since the chirality of one triangle could not extend to its neighboring corner-sharing triangles, which could have different chiralities.

The frustration affords a system with macroscopically degenerate ground states. The degree of degeneracy varies with different geometries and the different nature of spins (Ising, XY or isotropic Heisenberg) [11]. Experimentally, the frustration effect would reduce the long-range magnetic order or even completely remove it. One example is shown in Fig. 1.9 for the systems with antiferromagnetic interactions ( $\Theta_{cw} < 0$ ). Without frustration, the onset of long range antiferromagnetic order appears at Neel temperature  $T_N \sim |\Theta_{cw}|$ . However, in a frustrated system, the Neel temperature  $T_N \ll |\Theta_{cw}|$  or even the ordering disappears. Thus the ratio

$$f = |\Theta_{cw}| / T_N \quad (1.39)$$

is often used as the measure of the degree of magnetic frustration [10]. The Neel temperature  $T_N$  can be replaced by other critical temperatures where a magnetic order appears.



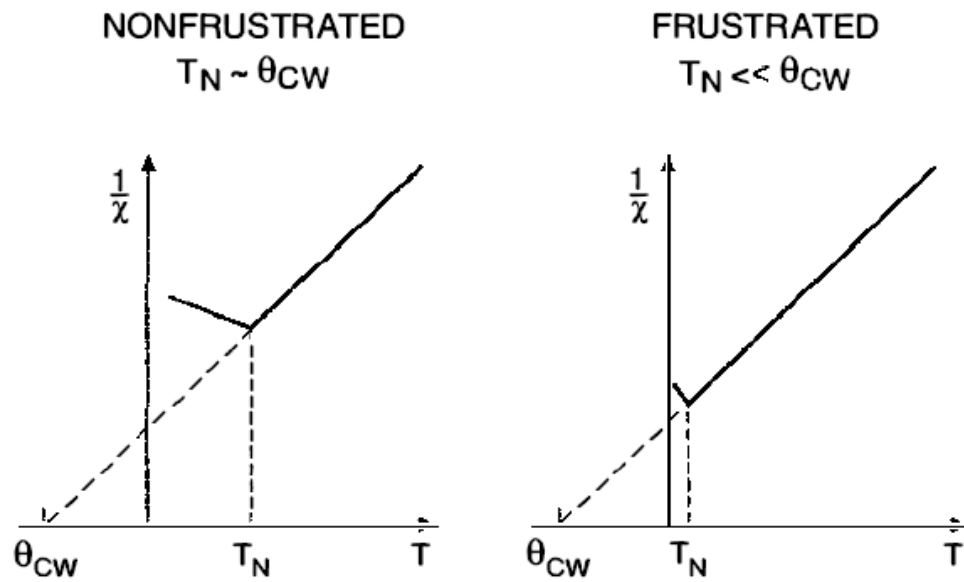


Figure 1.9 The experimental manifestation of frustration for the systems with antiferromagnetic interactions (After [10]).

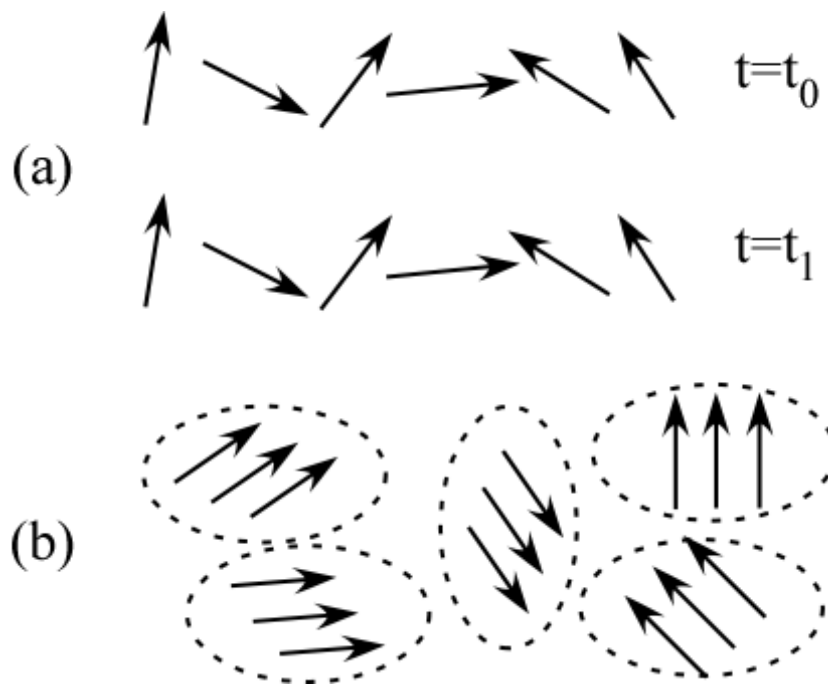


Figure 1.10 Frozen spin moments in (a) a spin glass at a time  $t_0$  and a later time  $t_1$  (b) a cluster glass

### 1.3.4 Spin glass

In a paramagnet, the atomic moment on each lattice point is fluctuating due to thermal excitations. In a ferromagnet or antiferromagnet at  $T = 0$ , each moment is frozen into one particular direction, and there is prevailing magnetic order throughout the lattice. Spin glass, which is different from the above two cases, has randomly orientated frozen local moments as shown in Fig. 10(a). But below the freezing temperature  $T_f$ , the total

magnetization  $\sum_i \langle S_i \rangle_t = 0$  and the staggered

magnetization  $\frac{1}{N} \sum_i \langle S_i \rangle_t \exp(i\mathbf{k} \cdot \mathbf{R}_i) = 0$  ( $N \rightarrow \infty$ ) [12], which means that there is no

long-range order present in the whole lattice. It is possible that the local magnetic order develops in a spin-glass-like state. As shown in Fig. 10(b), a cluster glass is one example.

The spin glass state arises from the interplay of the frustration effect and stochastic disorder, which was firstly discovered in diluted magnetic alloys CuMn. The spin glass state has also been discovered in many other materials, such as those with strong geometrical frustration. The most prominent common feature for various spin glass or spin-glass-like materials is thermal magnetic irreversibility, which manifests itself as a large difference between the field-cooled (FC) and zero-field-cooled (ZFC) magnetization (See Chapter 2, 3 and 4). Other experimental results that characterize a spin glass have been reviewed in ref. 12. However, there is one question that people are still speculating about: whether a purely frustrated system without disorder could afford a spin glass state or not. No final consensus has been achieved.

## 1.4 Experimental techniques

One of the most widely used techniques for detecting material magnetization is based on the well-known Faraday's law of induction,

$$V = -\frac{d\phi}{dt} \quad (1.40)$$

in which the electromotive force  $V$  induced in a loop is proportional to the rate of change in magnetic flux enclosed by the loop. Due to the small size, the samples are usually modeled as a magnetic dipole, which induces a magnetic field given by

$$B(\mathbf{r}) = \frac{\mu_0}{4\pi r^3} \left( \frac{3(\mathbf{m} \cdot \mathbf{r})\mathbf{r}}{r^2} - \mathbf{m} \right) + \frac{2\mu_0}{3} \mathbf{m} \delta^3(\mathbf{r}) \quad (1.41)$$

As shown in Fig. 1.11, the flux of a dipole moment through a loop with radius  $R$  is

$$\phi = \frac{\mu_0 m}{2} \frac{R^2}{(Z^2 + R^2)^{3/2}} \quad (1.42)$$

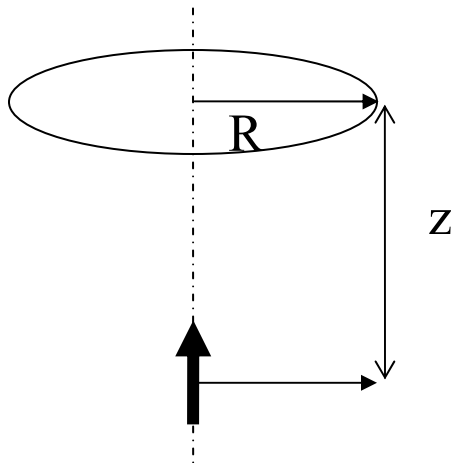


Figure 1.11 The magnetic flux of a dipole through a loop just above it

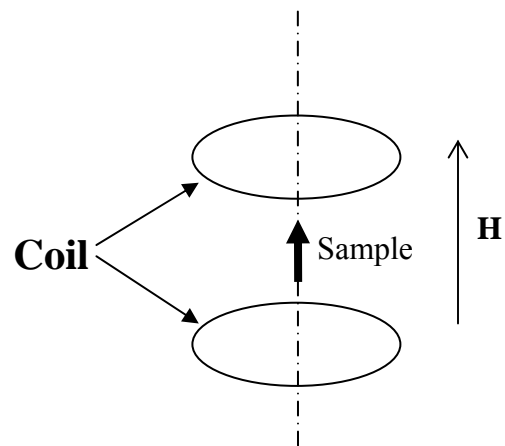


Figure 1.12 A schematic view of a vibrating sample magnetometer.

### 1.4.1 DC susceptibility

The susceptibility of a sample in a static magnetic field  $H$  is  $\chi = M/H$ , which is called DC magnetic susceptibility. One of tools used to measure the DC susceptibility is a vibrating sample magnetometer (VSM). Fig. 1.12 shows a schematic view of a VSM, in which a magnetic field  $H$  is supplied by a superconducting magnet and the sample is vibrating between the two signal pick-up coils. Usually the sample is vibrated sinusoidally with a low frequency  $f$  (e.g. 40Hz). The voltage signal induced by the sample movement is then sent to a lock in amplifier using a reference signal with the frequency and phase of the sample movement. A commercial VSM made by Quantum Design can measure a magnetization  $<10^{-6}$  emu [13].

### 1.4.2 AC susceptibility

If an alternating magnetic field  $H = H_{ac} \sin(\omega t)$  is applied to the sample, then the magnetization of the sample generally has a phase lag  $\varphi$  behind the driving field. Thus the so called AC susceptibility  $\chi$  has two components: the in-phase (real)  $\chi'$  component and out-of-phase (imaginary) component  $\chi''$ . The two components are given by,

$$\begin{aligned}\chi' &= \chi \cos(\varphi) \\ \chi'' &= \chi \sin(\varphi)\end{aligned}\tag{1.43}$$

The AC susceptibility can be measured by a mutual inductance AC magnetometer, which consists of a primary coil and two secondary pick-up coils as shown in Fig. 1.13.

The primary coil provides the driving magnetic field  $H$ . Two counter-wound pick-up coils are connected in series in order to cancel the background signal. The signal is then sent back to a dual channel lock-in amplifier using the driving signal as a reference. The real component  $\chi'$  and imaginary component  $\chi''$  are separated into the two channels of lock-in amplifier.

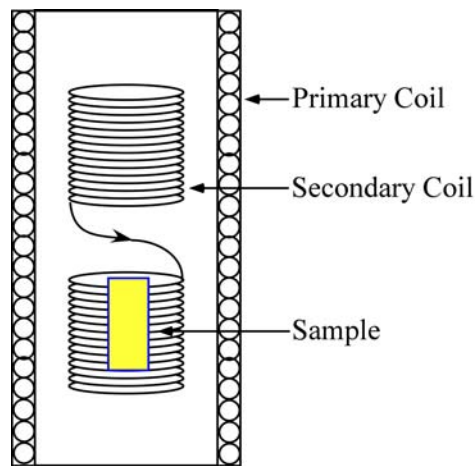


Figure 1.13 A schematic view of mutual inductance AC magnetometer

Fig. 1.14 shows a design and a photo of our home-made AC magnetometer. The coils are wound on a G10 coil form using  $60\mu\text{m}$  copper wires. The detailed dimensions of the coil form are shown in Fig. 1.14(a). The 10-layer primary coil has 5549 turns and the two 11-layer secondary has 1200 turns. After the cancellation, the background signal is  $<0.2\%$  of that without cancellation. The Keithley current source 6221 is used to drive the primary coil and the signal is picked up by a Stanford SR830 Lock in amplifier. The signal from the superconducting transition of a 30mg lead ball sample taken by this AC magnetometer is shown in Fig. 1.15. A commercial model of AC susceptometer is also offered by Quantum Design with a sensitivity  $2 \times 10^{-8}$  emu at 10kHz [13]. The sensitivity is decreasing with decreasing measure frequency.

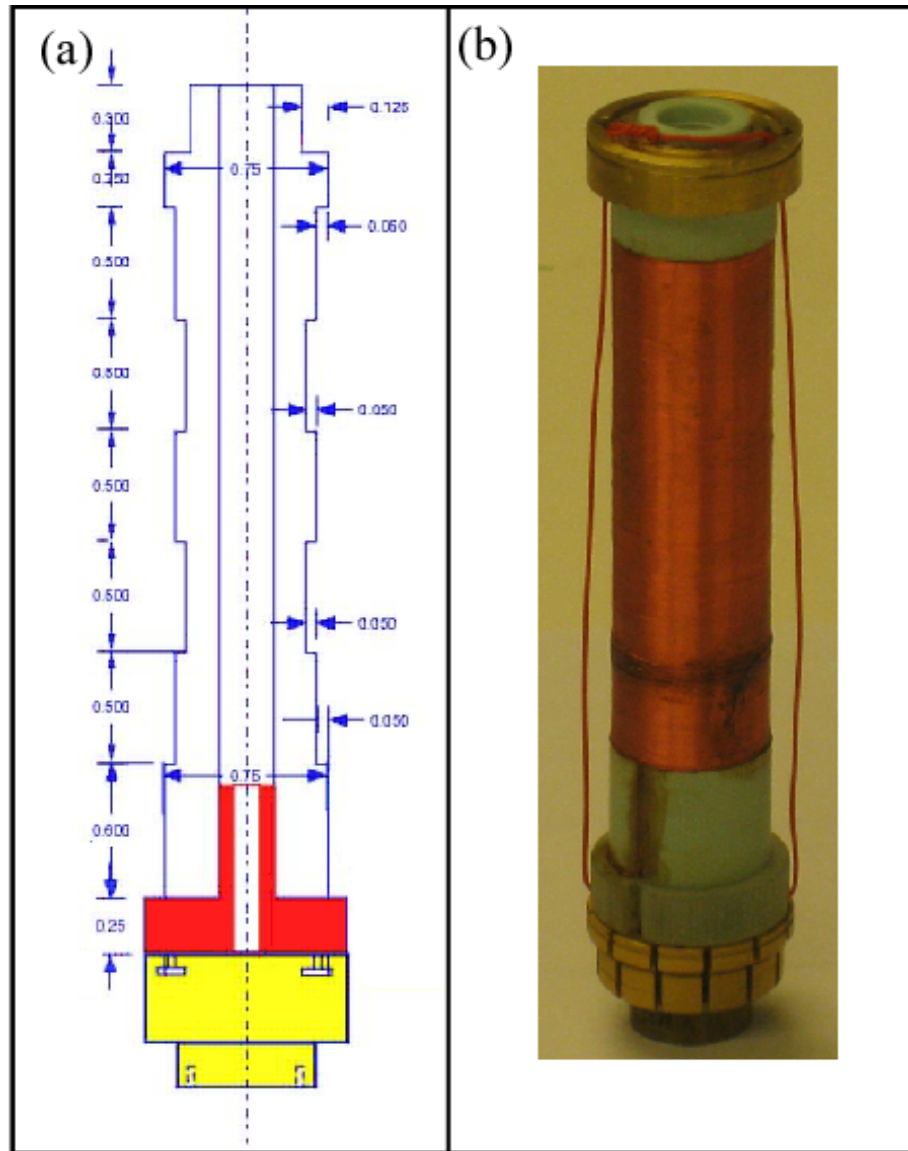


Figure 1.14 (a) The design of a mutual inductance AC magnetometer coil form (b) The real photo

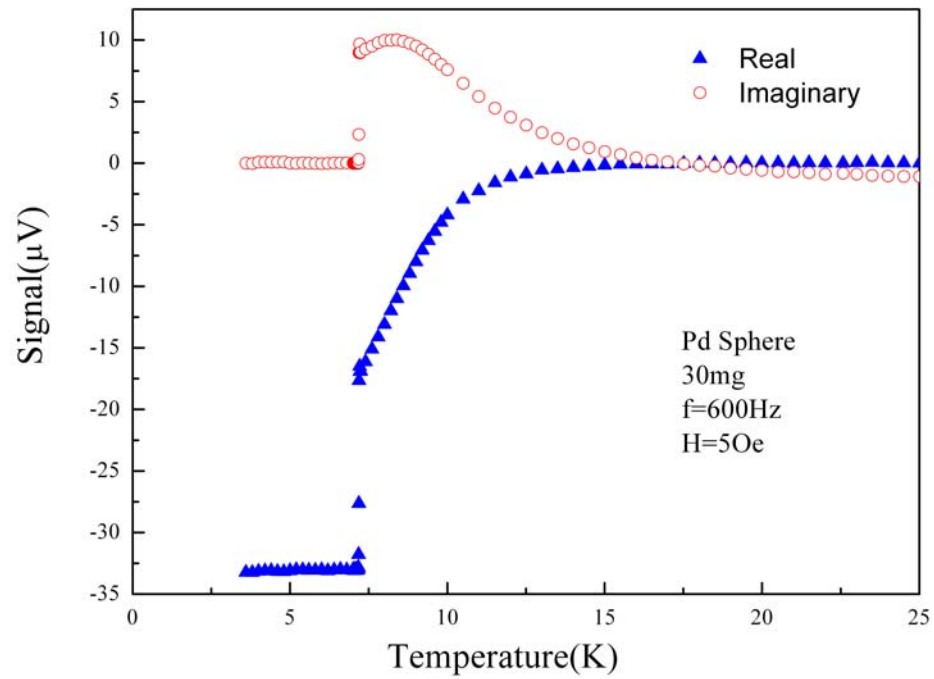


Figure 1.15 The superconducting transition of a lead sample resolved by the home-made AC magnetometer shown in Fig. 1.14.



# Bibliography

- [1] E. S. Abers, *Quantum Mechanics*, (Pearson Education, Inc., New Jersey, 2004).
- [2] N. Spaldin, *Magnetic Materials*, (Cambridge University Press, Cambridge, 2006).
- [3] D. H. Martin, *Magnetism in solids*, (ILIFFE Ltd., London, 1967)
- [4] N. W. Ashcroft and N. D. Mermin, *Solid state physics*, (Holt, Rinehart and Winston, New York, 1976).
- [5] M. Getzlaff, *Fundamentals of Magnetism*, (Springer, Berlin, 2008).
- [6] J. M. D. Coey, *Magnetism and magnetic materials*, (Cambridge University Press, New York, 2010).
- [7] M. A. Gîrțu, C. M. Wynn, W. Fujita, K. Awaga, and A. J. Epstein, *Phys. Rev. B* **61**, 4117 (2000).
- [8] D. Coffey, T. M. Rice, and F. C. Zhang, *Phys. Rev. B* **44**, 10112–10116 (1991).
- [9] B. D. Gaulin, *Nature Materials* **4**, 269 - 270 (2005).
- [10] A. P. Ramirez, *Annu. Rev. Matter. Sci.* **24**, 453 (1994).
- [11] R. Moessner, and J. T. Chalker, *Phys. Rev. B.* **58**, 12049 (1998).
- [12] K. Binder and A. P. Young, *Rev. Mod. Phys.* **58**, 801 (1986).
- [13] Quantum Design Inc. website

[http://www.qdusa.com/sitedocs/appNotes/vsmappnote\\_5-09.pdf](http://www.qdusa.com/sitedocs/appNotes/vsmappnote_5-09.pdf)

## **Chapter 2**

### **Magnetic Properties of $S = 1/2$**

#### **quasi-triangular lattice materials:**



### **2.1 Abstract**

We have investigated the structural and magnetic properties of two classes of spin  $S = 1/2$  antiferromagnetic quasi-triangular lattice materials:  $\text{Cu}_{2(1-x)}\text{Zn}_{2x}(\text{OH})_3\text{NO}_3$

( $0 \leq x \leq 0.65$ ) and its long chain organic derivatives  $\text{Cu}_{2(1-x)}\text{Zn}_{2x}(\text{OH})_3(\text{C}_7\text{H}_{15}\text{COO})\cdot\text{mH}_2\text{O}$  ( $0 \leq x \leq 0.29$ ). The series of layered structure compounds constitute a substitutional magnetic system, in which spin  $S = 1/2$   $\text{Cu}^{2+}$  ions and nonmagnetic  $\text{Zn}^{2+}$  ions are arranged on a 2D quasi-triangular lattice. For the nitrate compounds, we found that the substitution of  $\text{Zn}^{2+}$  ions can continuously decrease the Néel temperature,  $T_N$ , but never completely remove the magnetic order. In addition, the frustration effect in these materials is suppressed by a 3D interlayer interaction. On the other hand, the corresponding long-chain alkyl carboxylic acid group of intercalated materials,  $\text{Cu}_{2(1-x)}\text{Zn}_{2x}(\text{OH})_3(\text{C}_7\text{H}_{15}\text{COO})\cdot\text{mH}_2\text{O}$ , show spin-glass like behavior, which is caused by the interplay of geometric frustration and mixed sign interactions. A tentative explanation for these findings is proposed in terms of a cluster-glass picture.

## 2.2 Introduction

The study of frustrated interacting spin systems with unconventional magnetic ordering has attracted intense theoretical and experimental attention [1-3]. Geometric frustration, which endows the system with a macroscopically degenerate classical ground state, is believed to be one key factor that will destroy the formation of classical antiferromagnetic type order at a temperature determined by the spin coupling strength. Many materials with frustrated geometry such as layered triangular antiferromagnets [4], Kagomé magnets [5] and pyrochlore compounds [6, 7] have been shown to display a plethora of exotic low temperature phenomena including disordered spin liquid states, “order by disorder” and zero temperature Quantum Phase transitions, etc.

The triangular Quantum Heisenberg Antiferromagnet (TQHAF) is an ideal geometrically frustrated system that has attracted heavy theoretical interest during the past 25 years [8-11]. A prime focus of this interest has been the fluctuations in the  $S = 1/2$  quantum system which were postulated to reduce the non-collinear Néel-type spin order (three-sublattice order) leading to a spin liquid phase without long range order. Although extensive theoretical effort has been invested and some model materials [12-16] have been put forward, no final consensus has been achieved regarding the disordered liquid like ground states. New spin  $S = 1/2$  triangular lattice materials, especially those with tunable geometry and spin orders, will enable us to explore the low temperature phases of the TQHAF and help address the above issue. Accordingly, we report here our study on two classes of mixed metal ion quasi-triangular materials with adjustable magnetic ion concentration and interlayer distance, namely  $\text{Cu}_{2(1-x)}\text{Zn}_{2x}(\text{OH})_3\text{NO}_3$  and  $\text{Cu}_{2(1-x)}\text{Zn}_{2x}(\text{OH})_3(\text{C}_7\text{H}_{15}\text{COO})_m\text{H}_2\text{O}$  ( $m$  is the number of water molecules).

The botallackite-type monoclinic (see below) compound  $\text{Cu}_2(\text{OH})_3\text{NO}_3$ , is a layered structure hydroxy double salt in which the spin- $1/2$   $\text{Cu}^{2+}$  ions are on a quasi-triangular lattice similar to the perfect triangular lattice of  $\text{Mg}^{2+}$  ions in  $\text{Mg}(\text{OH})_2$ . As schematically shown in Fig. 2.1, the in-plane lattice of the  $\text{Cu}^{2+}$  ions is almost triangular except for the slight 3% difference in the lattice vectors  $\mathbf{a}_1$  and  $\mathbf{a}_2$ . This distortion results because  $\text{Cu}^{2+}$  ions favor a 4-coordinated square lattice exhibited by many high temperature superconductors [17] rather than a 6-coordinated triangular lattice. In each layer,  $\text{Cu}^{2+}$  sites can be categorized into two different groups Cu(I) and Cu(II) by the different octahedral environments they encounter. The adjacent Cu layers are widely

separated by 2 layers of  $\text{NO}_3$  groups, which can be replaced by even longer alkyl carboxylic acid anions to increase the  $c$ -axis basal spacing and enhance the 2D character. The parent compound  $\text{Cu}_2(\text{OH})_3\text{NO}_3$  and its organic derivatives have been studied by Linder *et al.* [18] and Gîrțu *et al.* [19], respectively. However, to our knowledge, the mixed ion compounds have not previously been studied.

The non magnetic Zn ion can be introduced into the copper layers to study the effect

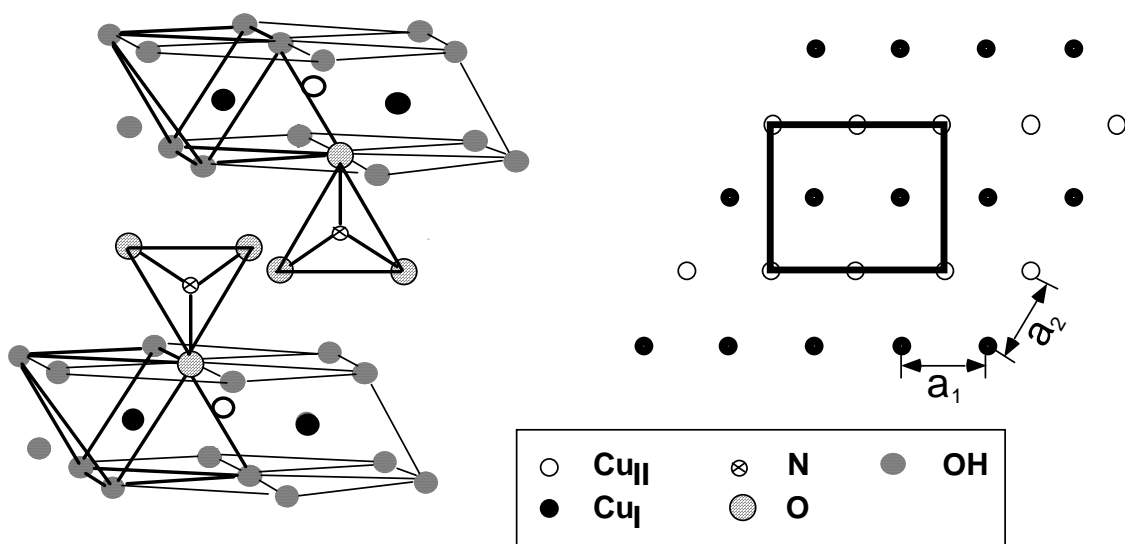


Figure 2.1 The left hand panel shows a perspective view of the basal unit of  $\text{Cu}_2(\text{OH})_3\text{NO}_3$ . The right hand panel shows a  $c$ -axis view of the Cu layer and its planar unit cell (dark rectangle).  $a_1 = 3.03 \text{ \AA} \neq a_2 = 3.17 \text{ \AA}$ .

of geometric frustration with reduced magnetic order in both the  $\text{NO}_3$  compounds and  $\text{C}_7\text{H}_{15}\text{COO}$  compounds. In this paper, we will report the structural and magnetic properties of the two classes of mixed ion compounds  $\text{Cu}_{2(1-x)}\text{Zn}_{2x}(\text{OH})_3\text{NO}_3$  and  $\text{Cu}_{2(1-x)}\text{Zn}_{2x}(\text{OH})_3(\text{C}_7\text{H}_{15}\text{COO})\cdot m\text{H}_2\text{O}$  as a function of increased Zn concentration in the copper layers.

## 2.3 Experimental Details

### 2.3.1 Sample Preparation

The preparation of powder samples of  $\text{Cu}_{2(1-x)}\text{Zn}_{2x}(\text{OH})_3\text{NO}_3$  follows the common synthesis routes of Hydroxy Double Salts  $[\text{M}_{1-x}\text{M}'_x]_2(\text{OH})_3\text{X}$  (here X represents univalent anions, such as  $\text{Cl}^-$ ,  $\text{NO}_3^-$  etc.), in which one metal oxide  $\text{M}'\text{O}$  is reacted with the water solution of another metal salt  $\text{MX}_2$  under hydrothermal conditions [20]. In our study, we found that the metal oxide  $\text{M}'\text{O}$  can also be replaced by metal hydroxide  $\text{M}'(\text{OH})_2$ . The  $x = 0$  base compound  $\text{Cu}_2(\text{OH})_3\text{NO}_3$  was synthesized through reaction of 200mg  $\text{Cu}(\text{OH})_2$  and 20 ml 1M  $\text{Cu}(\text{NO}_3)_2$  aqueous solution at  $65^\circ\text{C}$  for 3 days. The pale blue precipitate was separated by filtering and washing by distilled water 6 times, and then dried at  $75^\circ\text{C}$  in air for 24 hours. Single crystal samples can be obtained if the above hydrothermal reactions are carried out in an autoclave at  $T = 220^\circ\text{C}$  for 2 weeks [18]. The  $x = 0.13$  (0.19, 0.29, 0.43, 0.55, 0.65) mixed ion compounds were made by similar reactions, replacing the  $\text{Cu}(\text{OH})_2$  by 1.35g (1.48g, 1.79g, 1.95g, 2.44g, 3.26g) of ZnO powders. The interlayer nitrate ions can be substituted by long-chain anions such as carboxylic acid anions in anion exchange reactions. To prepare long-chain organic derivatives,  $\text{Cu}_{2(1-x)}\text{Zn}_{2x}(\text{OH})_3(\text{C}_7\text{H}_{15}\text{COO})\cdot\text{mH}_2\text{O}$ , 200 mg of the  $\text{Cu}_{2(1-x)}\text{Zn}_{2x}(\text{OH})_3\text{NO}_3$  powder samples were dispersed into 40ml 0.5M  $\text{C}_7\text{H}_{15}\text{COONa}$  water solution. The products were then filtered and washed 3 times in distilled water and 3 times in ethanol, and then dried at  $75^\circ\text{C}$  in air for 24 hours. The Zn concentrations of the mixed metal

ion compounds were determined by an Agilent 7500 ce Inductively Coupled Plasma Mass Spectrometer (ICP-MS) after the powder samples were dissolved in nitric acid.

## 2.3.2 Measurement Details

The powder X-ray diffraction (XRD) was performed with an automated Rigaku D-MAX Diffractometer with Cu-K $\alpha$  radiation ( $\lambda = 1.54 \text{ \AA}$ ). The X-ray tube was operated at 35kV and 30mA. The intensity data was collected over a scan over  $10^\circ - 90^\circ$  in steps of  $0.03^\circ$  at room temperature. Before measurement, the as-prepared powder samples were ground in a mortar and pestle to maintain uniform grain size and then affixed to a glass sample holder with a thin layer of Vaseline. This procedure resulted in a visually observable preferential planar orientation of the platelet like crystallites of the long chain samples with the  $c$ -axis normal to the plane of the glass holder. In most experiments, the scan speed was set to 1/2 degree per minute.

The 2-300K DC magnetization data was collected with a vibrating sample magnetometer (VSM, PPMS, Quantum Design) with a 9-T superconducting magnet. The powder samples were compressed into 10 – 20 mg cylindrical pellets with 3 mm diameter and 2-4 mm length by a hydraulic press under 50 psi pressure. The temperature dependence of the magnetic susceptibility was taken using two different protocols. The field-cooled (FC) susceptibility data were collected during the cooling process from room temperature under a 100 – 5000 Oe applied static magnetic field.

We can also cool the sample to the lowest temperature only under the residual field of

the superconducting magnet ( $\sim 2$  Oe). The zero-field-cooled (ZFC) data were then taken during warming under an applied field.

## 2.4 Results and Discussion

### 2.4.1 Structure Analysis

Fig. 2.2 shows the XRD patterns for 7 powder samples of  $\text{Cu}_{2(1-x)}\text{Zn}_{2x}(\text{OH})_3\text{NO}_3$ . The prominent reflections of the  $x = 0$  parent compound can be indexed to a monoclinic structure P21(4) with the unit cell parameters ( $\text{\AA}$ ):  $a = 5.594$ ,  $b = 6.071$ ,  $c = 6.923$  and  $\beta = 94.68^\circ$  [21]. Since the ionic radius of  $\text{Zn}^{2+}$  ( $0.74 \text{ \AA}$ ) is very close to that of  $\text{Cu}^{2+}$  ( $0.73 \text{ \AA}$ ) [22], the Zn doped samples are expected to inherit the basic framework of the parent compound with little distortion. As can be seen from Fig. 2.2, the (001) and (002) peaks are lined up for all the samples indicating nearly identical c-axis lattice parameters. Due to the limited number and width of the diffraction lines and the low symmetry of the doped powder samples, a complete structural analysis was not possible. However, if random Cu/Zn occupancy of the P21(4) space group is assumed for the doped compounds, as can be expected, their cell parameters can be calculated by a LeBail analysis [23]. Using this approach we find an expansion of the b-axis, a slight contraction of the a-axis, an x-independent c-axis, and a slight reduction in b with increasing Zn concentration as can be seen from Fig. 2.3. Moreover, the overlap of some ZnO reflections with reflections from the doped compounds further complicates the





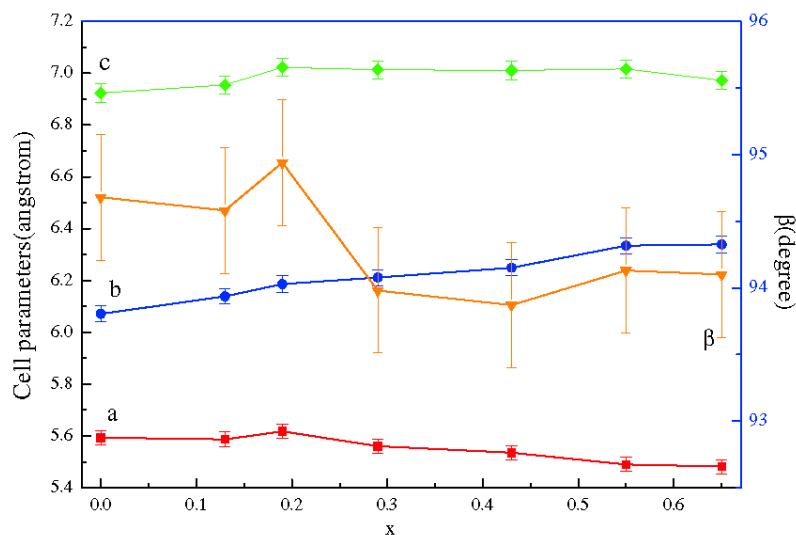
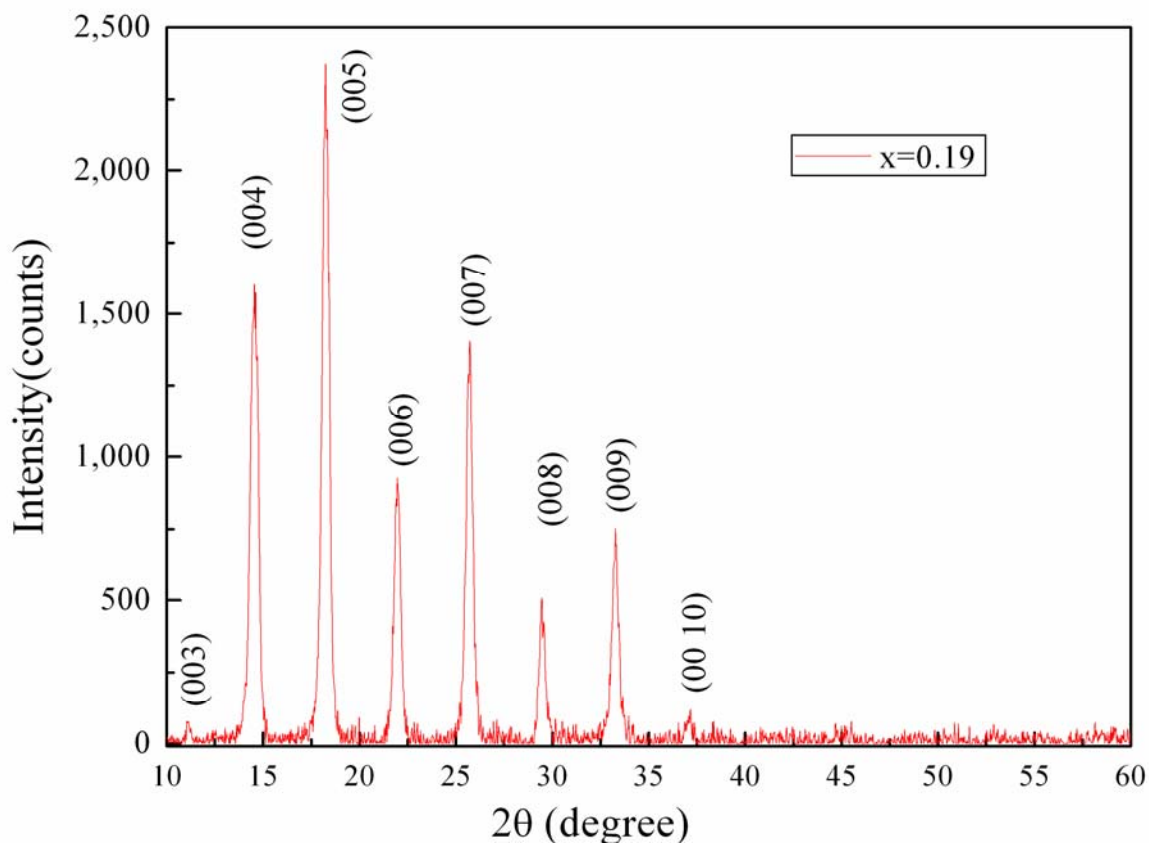


Figure. 2.3. Cell parameters of 7 short chain samples obtained from the Le Bail analysis. Fitting quality are as follow (x, Rp, Rwp): (0, 6.213, 8.812), (0.13, 6.653, 8.922), (0.19, 6.910, 9.244), (0.29, 6.324, 8.955), (0.43, 6.075, 8.634), (0.55, 5.788, 7.723), (0.65, 5.551, 7.243) In the fit, the similar quality fit could be obtained with slightly different cell parameters (about 0.5%). So the 0.5% error bars were added in the figure.

the X-ray analysis. Nevertheless, the susceptibility we measured for ZnO is from one to two orders of magnitude below that of our sample, which guarantees that ZnO impurities, if present, will not have a detectable effect on the magnetic aspects of our study.

A typical XRD pattern of the Zn-substituted intercalated long-chain organic group compound is shown in Fig. 2.4 for  $x = 0.19$ . A series of intense (00 $l$ ) reflections, with no other detectable diffraction lines point to the strong two dimensional character of this compound and preferential  $c$ -axis orientation of our sample. The interlayer distance of the long-chain samples determined from the (00 $l$ ) reflections is 24.2 Å (consistent with the previously reported value [24]) and does not change with Zn concentration.



**Figure. 2.4.** The X-ray powder diffraction pattern of  $\text{Cu}_{2(1-x)}\text{Zn}_{2x}(\text{OH})_3(\text{C}_7\text{H}_{15}\text{COO})\cdot n\text{H}_2\text{O}$  for  $x = 0.19$

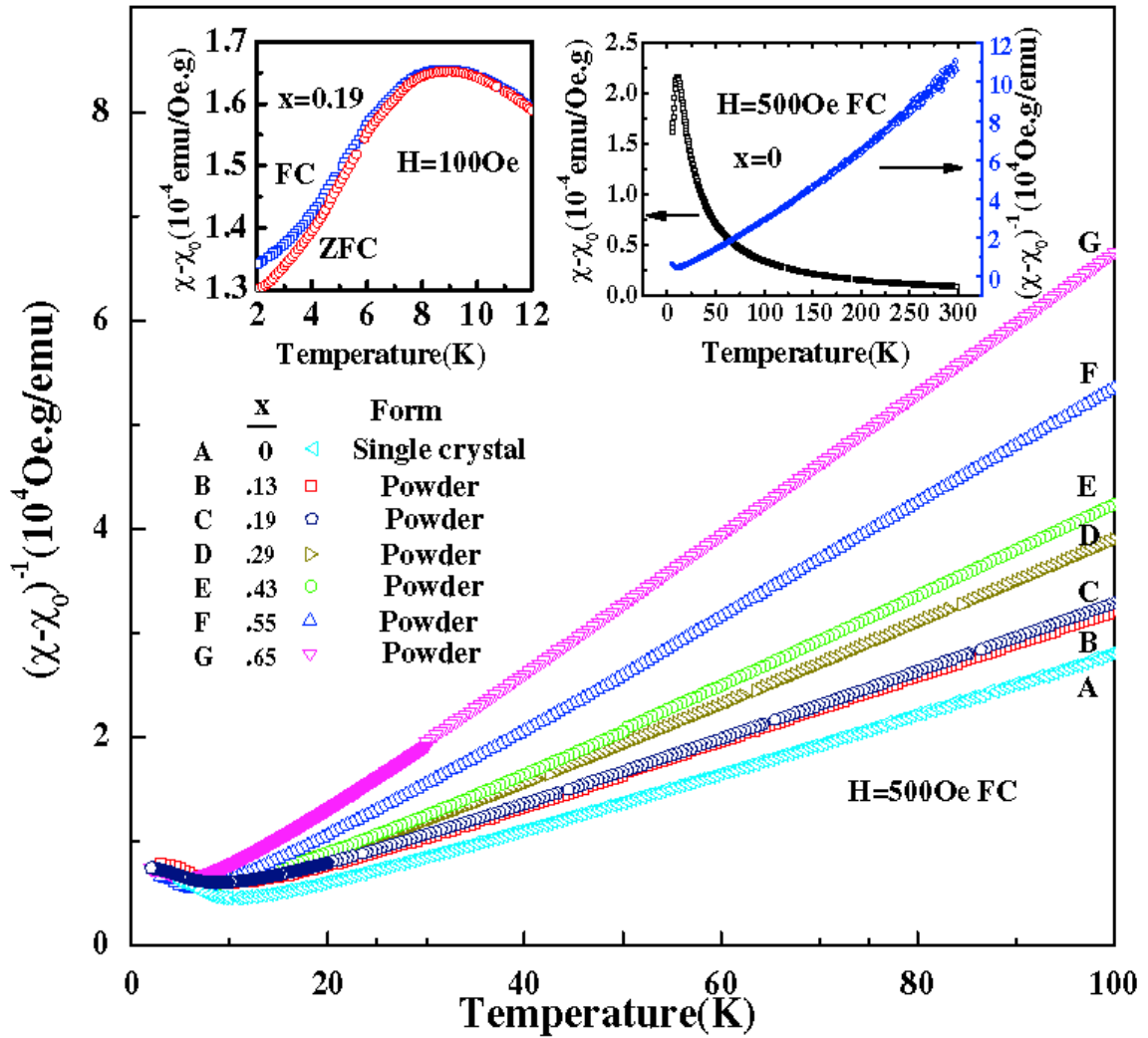


**Figure 2.5.** Main panel: 2-100K temperature dependence of the DC magnetic susceptibility of 7 nitrate anion compounds  $\text{Cu}_{2(1-x)}\text{Zn}_{2x}(\text{OH})_3\text{NO}_3$ . From bottom to top:  $x = 0, 0.13, 0.19, 0.29, 0.43, 0.55, 0.65$ . Left inset: a slight difference between ZFC and FC susceptibility of the  $x = 0.19$  sample. Right inset: 2-300K temperature dependence of  $\chi$  and its reciprocal for  $x = 0$  crystal sample. The temperature independent susceptibilities are  $(x, \chi_0 \times 10^{-7} \text{ emu/Oe.g})$ : (0, 13.491), (0.13, 0.562), (0.19, -1.918), (0.29, -3.302), (0.43, -3.369), (0.55, -0.524), (0.65, -1.830).

## 2.4.2 Magnetic Susceptibility

The temperature dependence of DC magnetic susceptibility of  $\text{Cu}_{2(1-x)}\text{Zn}_{2x}(\text{OH})_3\text{NO}_3$  ( $0 \leq x < 0.65$ ) is shown in Fig. 2.5. For the  $x = 0$  base copper compound, the difference in data acquired with FC and ZFC procedures is indistinguishable, indicating that the ground state is not glassy. At  $T = 11\text{K}$ , a broad peak appears as usually seen in low dimension antiferromagnets [25]. The anisotropic behavior of the  $x = 0$  samples was observed in previous study, and supports the notion that long-range AF ordering develops [18]. The Neel temperature  $T_N$  defined as the maximum value of  $|d\chi/dT|$  [26] is  $7.3\text{K}$ , which is lower than the peak position. The high temperature data above  $50\text{K}$  fits very well with the Curie-Weiss formula,  $\chi = C/(T - \Theta_{cw}) + \chi_0$ , in which  $\chi_0$  is included to incorporate the temperature independent contributions such as core diamagnetism and Van Vleck paramagnetism [27]. The parameters are: the Curie Constant  $C = 3.462 \times 10^{-3}$  emu.K/Oe.g, the Curie-Weiss Temperature  $\Theta_{cw} = -2.9\text{K}$  and  $\chi_0 = 1.349 \times 10^{-6}$  emu/Oe.g. From the Curie Constant, we can calculate the effective moment and g-factor to be  $\mu_{\text{eff}} = 1.823 \mu_B$  and  $g = 2.11$ , respectively. The value of the g-factor is close to the isotropic Landé g factor of 2 for the electron which supports the idea that spin coupling is of the Heisenberg-type.

The onset of antiferromagnetic ordering at low temperature can also be observed with the other  $x > 0$  samples. To illustrate the doping effect, we plot the Néel temperature,  $T_N$ , the Curie-Weiss temperature,  $\Theta_{cw}$ , and the calculated effective moment and g-factors in Fig. 2.6 as a function of Zn concentration. The Néel temperature shows a

clear decreasing trend with increasing Zn concentration. This can be explained as follows: in the parent compound the spin-1/2  $\text{Cu}^{2+}$  ions are coupled by the super-exchange interaction through the Cu-O-Cu bonds, while the doped non magnetic  $\text{Zn}^{2+}$  ions break the bonds in the ion network and effectively reduce the average coupling strength. Moreover, from the Curie constant (per mole Cu) slightly larger values of the Landé g-factors  $g = 2.17, 2.22, 2.16, 2.30, 2.28, 2.36$  were found for  $x = 0.13, 0.19, 0.29, 0.43, 0.55, 0.65$ , respectively. The increase in g values may come from the spin-orbit interactions and different local environments of Cu sites in different samples [28, 29]. In the Zn-doped samples, the Zn tends to adopt a tetrahedral coordination, while Cu adopts planar coordination. This difference is suggested as the possible origin of the local (g-value) anisotropy. This explanation is further supported by the fact that the small difference between the ZFC and FC susceptibility appears at  $T < T_N$  for the doped samples (see Fig. 2.5 left inset). We should also note that  $\Theta_{cw}$  undergoes a transition from negative to positive values at approximately  $x = 0.3$ , which indicates the onset of a net ferromagnetic interaction. However, the susceptibility data still show an antiferromagnet feature. The contradiction arises because the Curie-Weiss temperatures are so close to 0 that a small change in the Curie constant may lead to a sign change in  $\Theta_{cw}$ . As a result these positive values are more likely an indication of small systematic deviations from the ideal Curie-Weiss behavior of the materials.

To quantify the frustration in these quasi-triangular systems we employ the factor  $f = |\Theta_{cw}/T_N|$ , which is frequently used as a measure of frustration of a magnetically frustrated system [30]. Using this approach, the  $f$  values obtained for our doped nitrate samples are relatively low (0.4, 0.4, 0.3, 0.1, 0.3, 0.5, 0.3, respectively) in

comparison with other materials with geometric frustration ( $f > 10$  [30]). These small values of  $f$  indicate that the systems are unfrustrated or very weakly frustrated. As discussed in Section 3.1, the  $c$ -axis lattice parameter ( $= 6.92\text{\AA}$ ) in the present case is similar to the in-plane lattice parameters, indicating appreciable interlayer coupling in this quasi-two-dimensional system; this may diminish the degree of frustration.

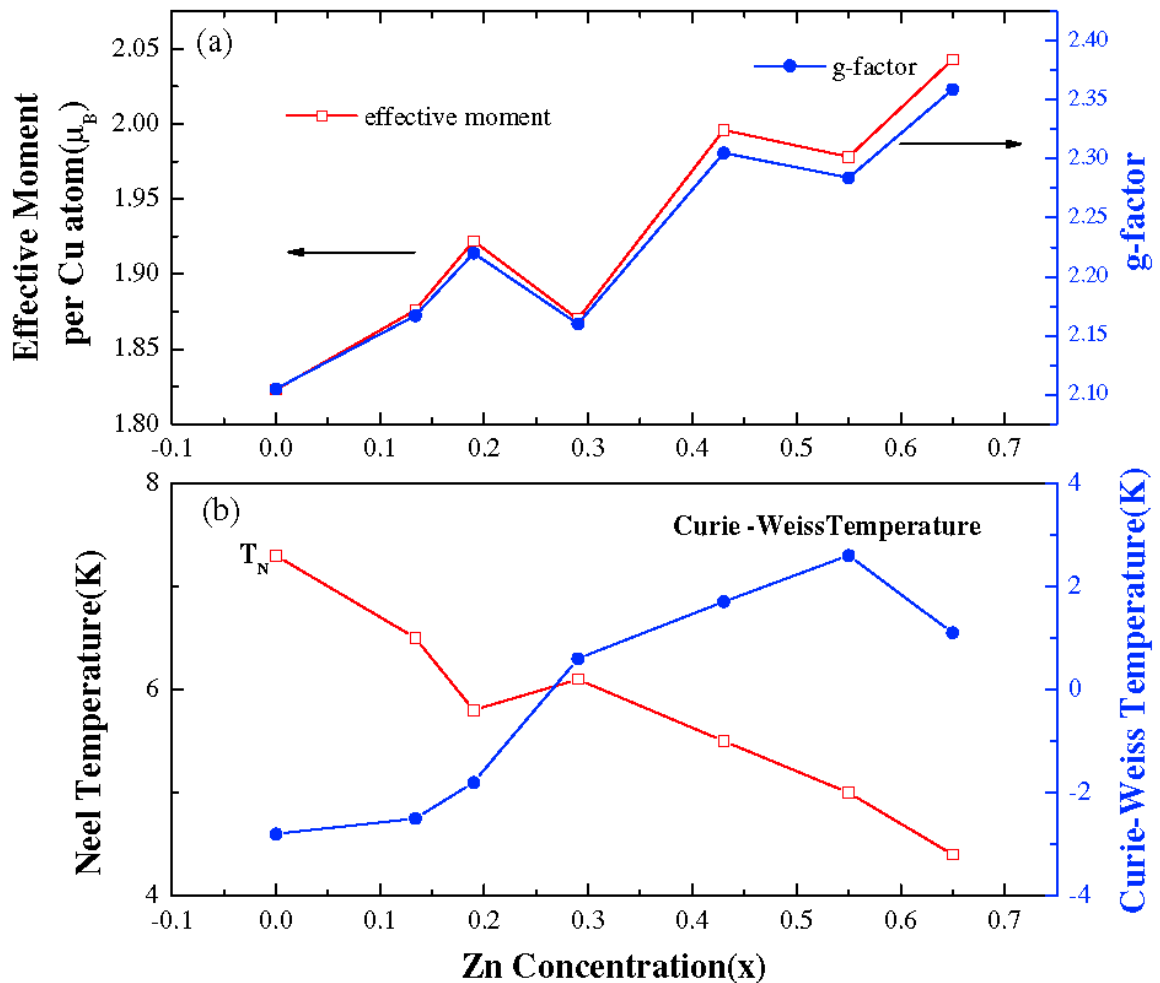
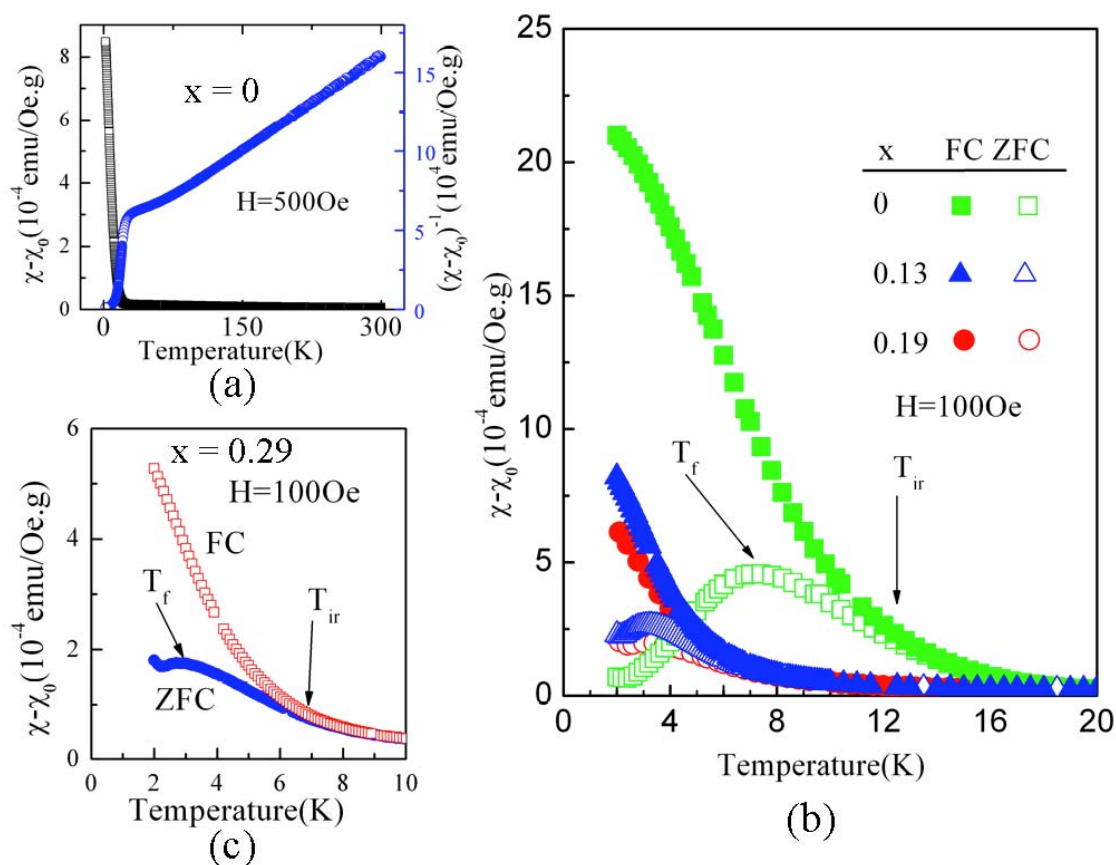


Figure 2.6. (a) The calculated effective moment and g factor for  $0 \leq x \leq 0.65$  nitrate group samples. (b) The calculated Curie-Weiss temperature and Néel temperature for  $0 \leq x \leq 0.65$  nitrate group samples.



**Figure 2.7.** (a) 2-300K temperature dependence of DC susceptibility  $\chi$  and its reciprocal for  $x = 0$   $\text{Cu}_{2(1-x)}\text{Zn}_{2x}(\text{OH})_3(\text{C}_7\text{H}_{15}\text{COO})\cdot m\text{H}_2\text{O}$  (b) 0-20K ZFC and FC susceptibility of  $x = 0, 0.13$  and  $0.19$  (c) A zoom-in view of ZFC and FC susceptibility for  $x = 0.29$ . The temperature independent susceptibilities are  $(x, \chi_0 \times 10^{-7} \text{ emu/Oe.g})$ :  $(0, -8.415)$ ,  $(0.13, -7.826)$ ,  $(0.19, -5.973)$ ,  $(0.29, -8.973)$ .

To improve the 2D character of the material, we replaced the interlayer nitrate group by a much longer carboxylic acid group  $\text{C}_7\text{H}_{15}\text{COO}$ . The temperature dependence of the FC magnetic susceptibility and its inverse are plotted in Fig. 2.7(a) for the pure Cu,  $x = 0$  sample. Unlike the short anion compounds,  $\text{Cu}_{2(1-x)}\text{Zn}_{2x}(\text{OH})_3\text{NO}_3$ , the data for this improved 2D material starts to deviate significantly from the Curie-Weiss behavior below



about 100K. A steep increase in  $\chi$  was observed below about 22 K, which is usually seen in materials exhibiting short- or long-range ferromagnetic correlations. However, the Curie-Weiss temperature calculated from the high temperature (100 K-300 K) susceptibility data is still negative ( $\Theta_{cw} = -94K$ ), but smaller in magnitude than the -140K reported by Gîrțu et al [19]. The much larger magnitudes for the Curie-Weiss temperature for these 2D compounds should be noted in comparison with only -2.9 K for the nitrate compound.

The Curie Weiss temperatures for the  $x = 0.13$ ,  $x = 0.19$ , and  $x = 0.29$  compounds became less negative to -74 K, -67 K, -64 K, respectively, with Zn substitution, similar to the above short chain compounds. The corresponding Néel temperatures 5.5 K, 2.8 K, 2.6 K, and 2.5 K, respectively, also showed a decrease with Zn substitution. The calculation of the Landé g-factors provides a way to make a rough estimate on  $m$ . If  $m = 1, 1, 3, 0$  for the  $x = 0, 0.13, 0.19$  and  $0.29$  samples, the resultant g-factors (2.09, 2.18, 2.18, 2.20) are in good agreement with the values for short chain compounds shown in the above section. The 0 – 20 K ZFC and FC susceptibility data for the  $x = 0, x = 0.13$ , and  $x = 0.19$  samples are shown in Fig. 2.7(b). Similar to the  $x = 0$  compound, the susceptibility data for the Zn substituted compound showed a sharp increase, but at a lower temperature of approximately  $T = 10K$ . Another important feature different from the short anion compounds is the onset of much more prominent irreversibility in the ZFC and FC data below a certain temperature  $T_{ir}$ , which is usually considered as a fingerprint of a spin-glass like ground state [31]. Note that  $T_{ir}$  decreases with increased Zn concentration as does the Neel temperature. Also,  $\chi_{ZFC}$  shows a broad maximum at a freezing temperature  $T_f$ , slightly smaller than  $T_{ir}$ . The spin-freezing temperatures  $T_f$

for  $x = 0, 0.13, 0.19, 0.29$  are 7.2K, 3.2K, 3.1K and 2.7K, respectively. These values are close to the  $T_N$  discussed above, which suggests that the spin-freezing is related to the antiferromagnetic correlation. In addition, as shown for the  $x = 0.29$  data (see Fig. 2.7(c)),  $\chi_{ZFC}$  increases again at temperatures  $T < T_f$ , only for the Zn substituted compounds. The degree of frustration  $f$  can be evaluated in two ways: in the first method the definition described above,  $f = |\Theta_{cw}/T_N|$ , yields the values 17.1, 26.4, 25.8, and 25.6, for  $x = 0, 0.13, 0.19, 0.29$ , respectively. Alternatively, the freezing temperature can be used instead of  $T_N$  so  $f = |\Theta_{cw}/T_f|$  and slightly smaller values are obtained (13.1, 23.1, 21.6 and 23.7). In both cases the degree of frustration is much larger compared to the short chain compounds (0.1 to 0.5).

### 2.4.3 Discussion

As shown above, all the nitrate ion compounds  $\text{Cu}_{2(1-x)}\text{Zn}_{2x}(\text{OH})_3\text{NO}_3$  exhibit antiferromagnetic correlation at low temperature.. The degree of frustration is relatively small compared to the other triangular materials with antiferromagnetic interactions. The substitution of non magnetic Zn ions into the materials has effectively reduced the magnetic order but fails to completely extinguish it. This evidence strongly suggests that the in-plane geometric frustration is relaxed by the 3D interlayer interaction. The dimensionality of the  $\text{Cu}_2(\text{OH})_3\text{NO}_3$  magnetic lattice is still controversial. Linder *et al.* [18] conducted a 2D analysis of a single layer magnetic network and concluded that the dominant interaction is the antiferromagnetic interaction between Cu(II) sites. But the possibility of a 3D ordering was also suggested. This is

further supported by a later density functional study of  $\text{Cu}_2(\text{OH})_3\text{NO}_3$  [32], in which the distribution of spin densities were found to differ from one plane to the other. Our results provide additional evidence to support the existence of interlayer coupling but the strength of the interlayer interaction is still a puzzle.

In the case of long chain compounds, the interlayer distance is expanded to a very large value, 24.2 Å, which should significantly reduce the interlayer interaction relative to the nitrate materials. However, a strong signal of the onset of ferromagnetic correlation in the expanded compounds was observed. This is very likely due to the nature of Cu-O-Cu super-exchange path where the exchange coupling strength and sign strongly depend on the bond angle according to the well known Goodenough-Kanamori analysis [33]. The structural distortion caused by the intercalated long chain alkyl carboxylic acid group may be responsible for a change in bond angle resulting in a change of exchange coupling strength and interaction sign. The water molecules in the gallery also play an important role, which helps deform in-plane bond angles and thus modify the magnetic properties [34]. This kind of structural distortion induced by intercalation groups is also seen in other layered compounds such as  $\text{A}_{1-x}\text{B}_x\text{Vm}$  (where A and B are ions of different ionic radii and Vm is vermiculite) and well described in a layer rigidity model [35]. The insertion of the long chain compound also introduces additional randomness into the materials. The two layers of pillar groups  $\text{C}_7\text{H}_{15}\text{COO}$  may align with slightly different angles leading to variations in super exchange coupling strengths. For this reason, in the long chain compounds, not only the geometric frustration but also the mixed sign interaction or randomness in the bond strengths play

an important role in enabling the spin-glass like behavior at low temperature (even in the  $x = 0$  case).

It is important to note that the long-chain materials studied here are different from the canonical spin glass [31] in several important features: (1)  $\chi_{FC}$  does not saturate but continues to increase below  $T_f$ . (2)  $\chi_{ZFC}$  peaks at  $T_f$  slightly smaller than  $T_{ir}$  while in a canonical spin glass  $T_{ir}$  is below  $T_f$ . These features resemble the so-called cluster-glass behavior, which has been reported in various other materials [36-38]. A tentative understanding can be obtained if a cluster-glass picture is assumed. The sharp increase in susceptibility corresponds to the formation of local ferromagnetic clusters. The increase in  $\chi_{FC}$  below  $T_f$  can be understood as resulting from the strengthening of the inter-cluster ferromagnetic correlation under the external applied field. The spin-freezing observed in  $\chi_{ZFC}$  is likely a consequence of the onset of inter-cluster antiferromagnetic correlation. We also note that the increase in  $\chi_{ZFC}$  again below  $T_f$  is only observed in  $x > 0$  samples under low field. The doping of the magnetic Cu lattice with nonmagnetic Zn thus fragments the 2D magnetic ion lattice and shrinks the size of ferromagnetic clusters formed at low temperature. This fragmentation facilitates the development of inter-cluster correlations.

## 2.5 Conclusions

We have synthesized two classes of mixed ion materials  $\text{Cu}_{2(1-x)}\text{Zn}_{2x}(\text{OH})_3\text{NO}_3$  and their organic derivatives  $\text{Cu}_{2(1-x)}\text{Zn}_{2x}(\text{OH})_3(\text{C}_7\text{H}_{15}\text{COO})\cdot m\text{H}_2\text{O}$  with different interlayer

distances. Based on the study of the magnetic properties of these two closely related classes, we proposed that: (1) The nitrate group compounds are antiferromagnetically correlated at low temperature but with their geometric frustration released by a significant interlayer interaction. The magnetic order attenuates as the Zn concentration increases but still survives in Zn-rich samples ( $x = 0.65$ ). (2) The carboxylic acid group intercalated samples show cluster-glass-like behavior, which is likely the consequence of geometric frustration and the coexistence of antiferromagnetic and ferromagnetic interactions.

## **2.6 Acknowledgements**

We thank the Washington University Center for Materials Innovation (CMI) for seed funding support for this work

## Bibliography

- [1] Schiffer P 2002 *Nature* **420** 35-8
- [2] Ong N P and Cava R J 2004 *Science* **305** 52-3
- [3] Moessner R and Chalker J T 1998 *Phys. Rev. B.* **58** 12049-62
- [4] Collins M F and Petrenko O A 1997 *Can. J. Phys.* **75** 605-55
- [5] Helton J S, Matan K, Shores M P, Nytko E A, Bartlett B M, Yoshida Y, Takano Y, Suslov A, Qiu Y, Chung J-H, Nocera D G and Lee Y S 2007 *Phys. Rev. Lett.* **98** 107204
- [6] Bramwell S T and Gingras M J P 2001 *Science* **294** 1495-501
- [7] Gardner J S, Ehlers G, Bramwell S T and Gaudin B D 2004 *J. Phys.: Condens. Matter.* **16** 5643-51
- [8] Anderson P W 1973 *Matter. Res. Bull.* **8** 153-60
- [9] Fazekas P and Anderson P W 1974 *Phil. Mag.* **30** 423-40
- [10] Kalmeyer V and Lagughlin R B 1987 *Phys. Rev. Lett.* **59** 2095
- [11] Singh R R P and Huse D A 1992 *Phys. Rev. Lett.* **68** 1766
- [12] Powell B J and McKenzie R H 2006 *J. Phys.: Condens. Matter.* **18** R827
- [13] Bramwell S T, Carling S G, Harding C J, Harris K D M, Kariuki B M, Nixon L and Parkin I P 1996 *J. Phys.: Condens. Matter.* **8** L123
- [14] Shimizu Y, Miyagawa K, Kanoda K, Maesato M and Saito G 2003 *Phys. Rev. Lett.* **91** 107001
- [15] Tamura M and Kato R 2002 *J. Phys.: Condens. Matter* **14** L729
- [16] Ito T, Oyamada A, Maegawa S, Tamura M and Kato R 2008 *Phys. Rev. B* **77**

104413

- [17] Pickett W E 1989 *Rev. Mod. Phys.* **61** 433-512
- [18] Linder G G, Atanasov M and Pebler J 1995 *J. Solid State Chem.* **116** 1-7
- [19] Gîrțu M A, Wynn C M, Fujita W, Awaga K and Epstein A J 2000 *Phys. Rev. B* **61** 4117-30
- [20] Meyn M, Beneke K and Lagaly G 1993 *Inorg. Chem.* **32** 1209-15
- [21] Heffenberger H 1983 *Z. Krist.* **165** 127
- [22] Shannon R D 1976 *Acta Cryst. A* **32** 751-67
- [23] Hunter B 1998 "Rietica - A visual Rietveld program", International Union of Crystallography Commission on Powder Diffraction Newsletter No. 20 (Summer) <http://www.rietica.org>
- [24] Morioka H, Tagaya H, Karasu M, Kadokawa J-I and Chiba K 1998 *J. Mater. Res.* **13** 848-51
- [25] Woodward, F M, Albrecht A S, Wynn C M, Landee C P and Turnbull M M 2002 *Phys. Rev. B* **65** 144412
- [26] Yan L-Q, Maciá F, Jiang Z-W, Shen J, He L-H and Wang F-W 2008 *J. Phys.:Condens. Matter* **20**, 255203
- [27] Benmokhtar S, Belmal H, El Jazouli A, Chaminade J P, Gravereau P, Pechev P, Grenier J C, Villeneuve G and De Waal D 2007 *J. Solid State Chem.* **180** 772-9
- [28] Fujita W, Awaga K and Yokoyama T 1997 *Inorg. Chem.* **36**, 196
- [29] Dzyaloshinskii I 1958 *J. Phys. Chem. Solids.* **4** 241  
Moriya T 1960 *Phys. Rev.* **120** 9
- [30] Ramirez A P 1994 *Annu. Rev. Matter. Sci.* **24** 453-80

- [31] Binder K and Young A P 1986 *Rev. Mod. Phys.* **58** 801
- [32] Massobrio C, Rabu P, Drillon M and Rovira C 1999 *J. Phys. Chem. B* **103** 9387-91
- [33] Anderson P W 1975 *Solid State Phys.* **14** 99
- [34] Laget V, Hornick C, Rabu P, Drillon M and Ziessel R, *Coordination Chemistry Reivew* 1998 **178-180** 1533-53
- [35] Kim H, Jin W, Lee S, Zhou P, Pinnavaia T J, Mahanti S D and Solin S A 1988 *Phys. Rev. Lett.* **60**, 2168
- [36] Marcano N, Gómez Sal J C, Espeso J I, Fernández Barquín L and Paulsen C 2007 *Phys. Rev. B* **76** 224419
- [37] Dieny B and Barbara B 1986 *Phys. Rev. Lett.* **57** 1169-72
- [38] Mukherjee S, Ranganathan R, Anilkumar P S and Joy P A 1996 *Phys. Rev. B* **54** 9267



# Chapter 3

## Spin glassiness and power law scaling in anisotropic triangular spin-1/2 antiferromagnets

### 3.1 Abstract

We present data on the magnetic properties of two classes of layered spin  $S = 1/2$  antiferromagnetic quasi-triangular lattice materials:  $\text{Cu}_{2(1-x)}\text{Zn}_{2x}(\text{OH})_3\text{NO}_3$  ( $0 \leq x \leq 0.65$ ) and its long organic chain intercalated derivatives  $\text{Cu}_{2(1-x)}\text{Zn}_{2x}(\text{OH})_3(\text{C}_7\text{H}_{15}\text{COO})_m\text{H}_2\text{O}$  ( $0 \leq x \leq 0.29$ ), where non-magnetic Zn substitutes Cu isostructurally. It is found that the intercalated compounds, even in a clean system in the absence of dilution,  $x = 0$ , show

spin-glass behavior, as evidenced by DC and AC susceptibility, and by time dependent magnetization measurements. A striking feature is the observation of a sharp crossover between two successive power law regimes in the DC susceptibility above the freezing temperature. In contrast to standard theoretical expectations, these power laws are insensitive to doping. Specific heat data are consistent with a conventional phase transition in the unintercalated compounds and glassy behavior in the intercalated compounds.

## **3.2 Introduction**

The study of frustrated quantum magnetism has defined new paradigms of condensed matter for many decades. When low dimensionality, geometrical frustration, and quantum fluctuations interplay, novel and interesting phase diagrams may result. Another driving factor of key importance is disorder. Much excitement has been generated by the recent discovery of a possible realization of the long sought “spin liquid” phase, in compounds such as herbertsmithite [1]. Another intricate state of matter, the spin glass, has been thoroughly studied in systems such as  $\text{LiHo}_x\text{Y}_{1-x}\text{F}_4$  [2]. Despite these efforts, the spin glass state (and, in particular, its realization in electronic systems) is still counted among the most enigmatic states of matter. Many questions remain unresolved. One such key question is whether spin glass type behavior requires explicit structural disorder of the host system, because of the short time scales generally associated with spin dynamics in clean systems, or whether it may be acquired spontaneously in a clean system (as in, e.g., ordinary glasses). This question is

furthermore relevant in the light of the recent interest in spin-ice materials [3]. Here, we present experimental results shedding light on this and other issues in a different class of materials. The systems under investigation are derivatives of the layered compound copper-hydroxy nitrate (CHN),  $\text{Cu}_2(\text{OH})_3\text{NO}_3$  in the presence of zinc doping. The derivatives studied are (i) the diluted CHN system  $\text{Cu}_{2(1-x)}\text{Zn}_{2x}(\text{OH})_3\text{NO}_3$ , and (ii) the long organic chain (LOC) intercalates  $\text{Cu}_{2(1-x)}\text{Zn}_{2x}(\text{OH})_3(\text{C}_7\text{H}_{15}\text{COO})\cdot m\text{H}_2\text{O}$  ( $0 \leq x \leq 0.29$ ), where non-magnetic organic chains enter the galleries between the layers and increase their separation to 24 Å. In the absence of doping, these layered hydroxides are distorted triangular  $S=1/2$  antiferromagnets. Some properties of the  $x = 0$  compounds have been studied earlier [4, 5]. Evidence of glassiness has been reported for the  $x = 0$  LOC compounds, which were argued to be clean systems described by frustrated short range magnetic interactions without much disorder [5].

In recent years, chemical doping has proven to be an invaluable tool in accessing an extended phase diagram of transition metal oxides, in particular for detecting otherwise inaccessible transitions. Examples are the high temperature superconducting cuprates and pnictides, and various heavy fermion compounds [6–9], some of which also exhibit glassiness in some parameter regime. In this work, we apply this tool to study the CHN compound and its LOC derivative. In doing so, we have discovered a remarkably robust behavior of the LOC compounds which manifests itself through two distinct regimes of power law scaling in the temperature dependence of the DC susceptibility, separated by a sharp crossover. Moreover, we also identify this behavior in the undoped parent material. We find that Zn doping enhances this effect and shows it to be a robust feature of the physics of the glassy LOC compounds. Furthermore, we present significant new

evidence for the glassiness of both the doped and undoped LOC compounds. The ability to control the Zn concentration sheds further light on the relation between structural disorder and the glassiness of these compounds.

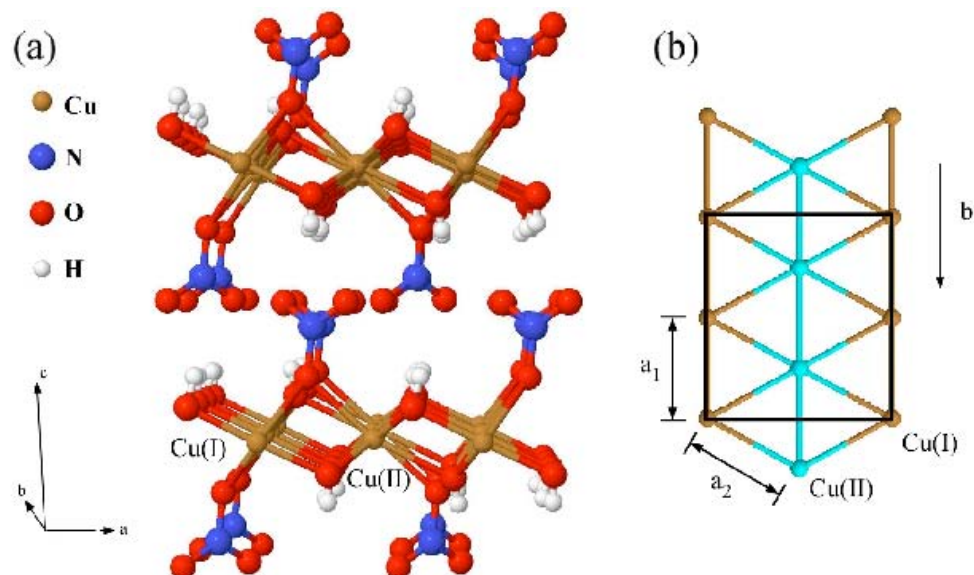


Figure 3.1 Structure of the CHN compound. a) A perspective view of the basal unit. b) c-axis view of the Cu layer and its planar unit cell (dark rectangle).  $a_1=3.03\text{\AA}$ ,  $a_2=3.17\text{\AA}$ .

### 3.3 Structure and preparation

The structure of the CHN compound is shown in Fig. 3.1. The unit cell contains two inequivalent  $\text{Cu}^{2+}$  ions forming distorted triangular layers. The preparation of the undoped samples follows Refs. 4 for CHN and 5 for the LOC compounds. The method for preparing the Zn-doped samples has been reported earlier [10]. Powder X-ray diffraction measurements have been carried out [10]. For both LOC intercalates and diluted CHN samples, Zn was found to replace Cu leading to a series of isostructural doped compounds. The LOC samples are characterized by pronounced (00l) reflections, as is typical for layered structure compounds with large interlayer distances. From this the interlayer distance was obtained to be  $24.2\text{\AA}$ , consistent with Ref. 5. This distance was also found to be independent of Zn doping concentration. A detectable ZnO impurity phase was only observed in the  $x = 0.65$  sample.

### 3.4 DC and AC susceptibility

DC susceptibility data for the diluted CHN system has been reported in Ref. 10. Both the Curie-temperature and the Neel temperature vary with Zn concentration, but are on the order of 10K in agreement with density functional values for the exchange couplings [11]. The value of the exchange interaction parameter is known to be sensitive to the Cu-OH-Cu bond angle, with both ferromagnetic (FM) and anti-ferromagnetic (AFM) values being possible. In CHN the angle is close to the FM-AFM crossover [4] rendering the material weakly anti-ferromagnetic. Interestingly, with increased Zn

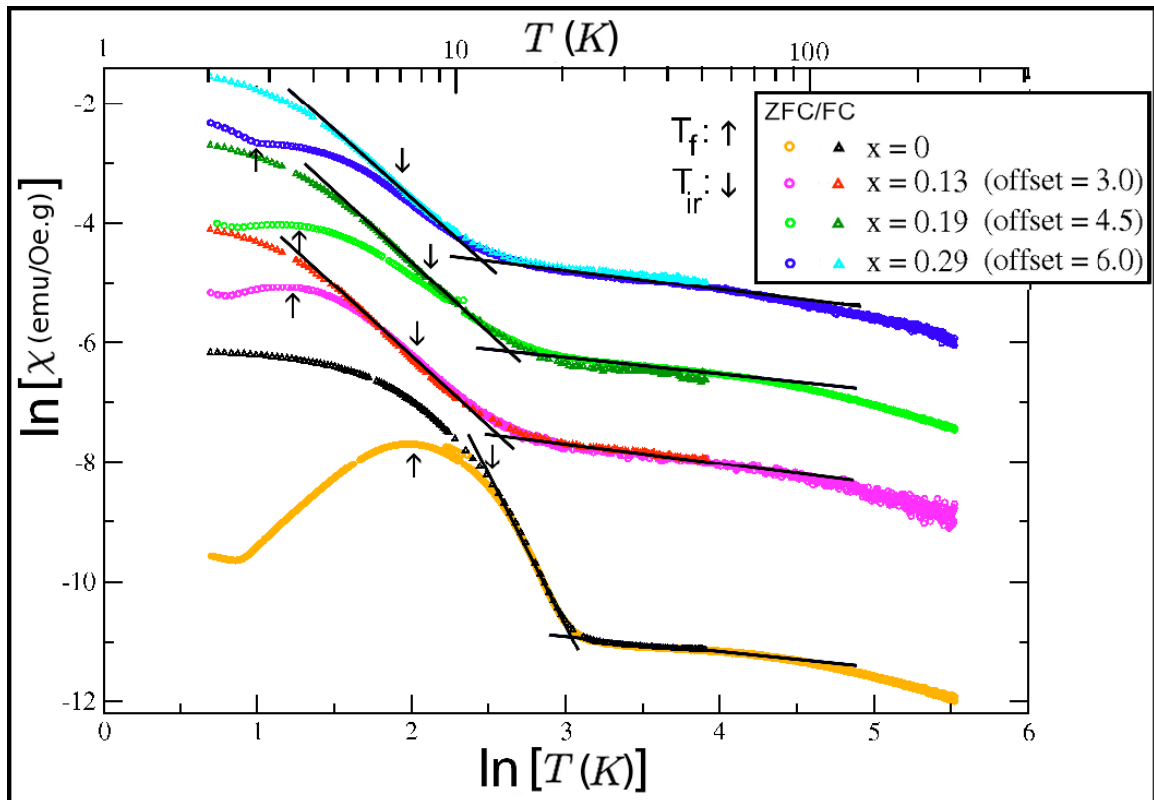


Figure. 3.2  $\ln(\chi)$  vs.  $\ln(T)$  for DC susceptibility (LOC samples). Both field cooled and zero field cooled data are shown, with different offsets for different dopings  $x$  as indicated. The freezing temperature  $T_f$  and irreversibility temperature  $T_{ir}$  are indicated by arrows. Linear fits identify various temperature regimes where  $\chi(T)$  is well described by power laws. In the lower temperature regimes, field cooled data was used for the fit. However, the zero field cooled data is seen to follow similar and in some cases almost identical power laws.

concentration the Curie constant was found to change sign and become ferromagnetic [10]. There was, however, no FM phase seen at low temperature and a complete analysis of this behavior would likely need to take into account Dzyaloshinskii-Moriya (DM) interactions, which result from the relatively low symmetry at the Cu site [5].

We will now focus on the LOC susceptibility data shown in Fig. 3.2. A clear difference between the zero field cooled (ZFC) and field cooled (FC) data below a temperature  $T_{ir} \sim 6-12\text{K}$  is a first indication of the glassiness of the LOC samples. No similarly large effect has been seen in the diluted CHN samples [10]. Note that the FC susceptibility of the  $x = 0$  sample grows by two orders of magnitude between 20K and 2K. Such changes have been seen in other spin glasses and electronic glasses in a variety of response functions [12]. It is worth pointing out that in the LOC case, the ZFC/FC difference actually diminishes at finite Zn concentration compared to the undoped parent compound. This may indicate that the glassiness of the system is indeed driven by frustration rather than disorder. Similarly, the freezing temperature  $T_f$  as determined by the peak in the ZFC susceptibility is  $\sim 8\text{K}$  for the  $x=0$  sample, and is  $\sim 2\text{K}$  lower for the Zn-doped samples.

A remarkable feature seen in the log-log plots of Fig. 3.2 is the presence of a sharp crossover between two distinct power law regimes above  $T_f$ . The first of these regimes corresponds to a temperature window typically between 5K and 12K, where  $\chi \propto T^{-a}$  with different exponents  $a \approx 5$  for  $x=0$   $a \approx 2$  and for  $x > 0$ . In a second regime at higher temperatures roughly between 12K and 90K,  $\chi \propto T^{-b}$  with  $b \approx 0.3$  for all samples, below a Curie tail with  $\chi \propto T^{-1}$  for  $T > 90\text{K}$ . This behavior is slightly more pronounced

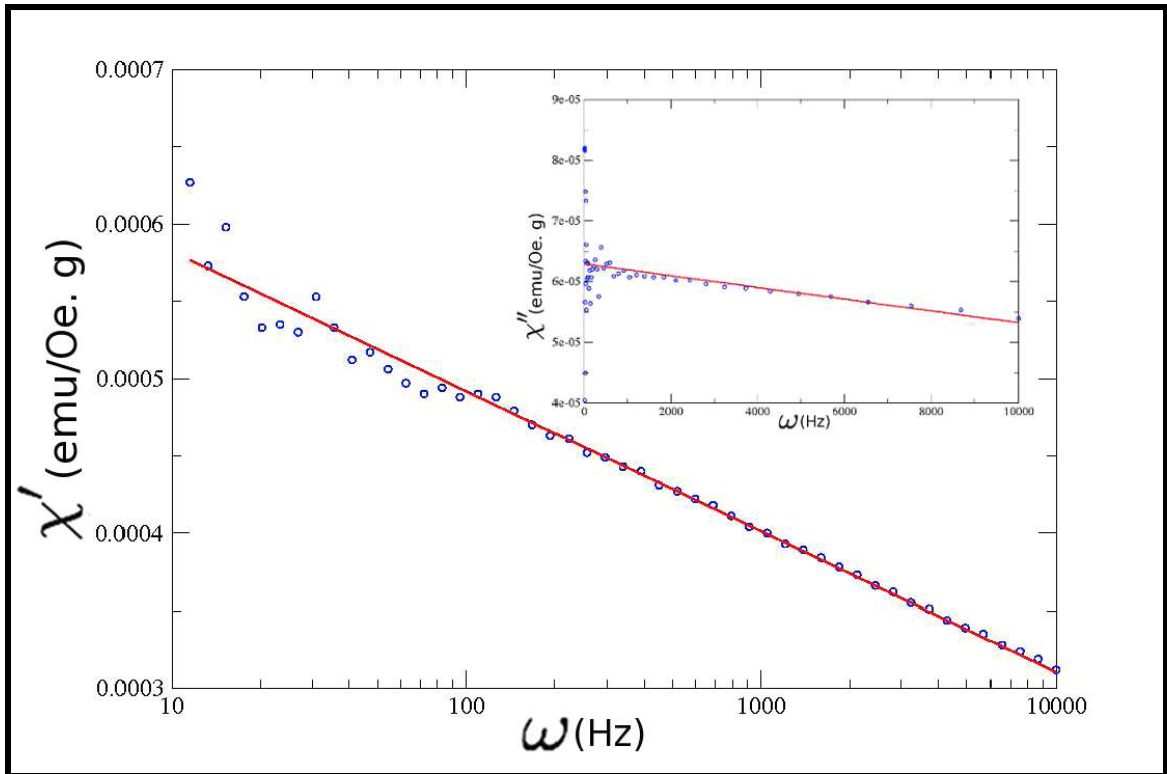


Figure. 3.3 AC susceptibility of  $x = 0$  sample at  $T = 10\text{K}$ . The real part is fitted to the functional form  $\chi' = \chi_0 - c \ln(\omega)$ . The linear fit of the imaginary part (inset) approaches  $\pi c / 2$  at  $\omega = 0$  to within 2% accuracy.



in the  $x > 0$  samples which all have very similar exponents, but is clearly identifiable also in the  $x = 0$  sample. Hence the sharp crossover between two different power law regimes as a precursor to the spin glass phase appears to be a robust feature of the physics of the LOC samples. To our knowledge, the finding of power law behavior that is insensitive to doping has not been reported earlier. We note that FC and ZFC data are indistinguishable in the higher temperature regime. In the lower temperature regime, the FC data have been used for the linear fits in Fig. 3.2. However, the ZFC data display power law behavior with similar exponents even there.

The frequency dependence of the AC susceptibility of the  $x = 0$  LOC sample is shown in Fig. 3.3. The real part  $\chi'$  was found to be extremely well described by the logarithmic functional form  $\chi' = \chi_0 - c \ln(\omega)$  at low frequencies  $< 10^4$  Hz, a standard behavior [13] for spin glasses. This is in good agreement with the imaginary part (inset), whose low frequency limit is a non-zero constant that agrees well with  $\pi c/2$  as determined from the real part via Kramers-Kronig relations. These findings provide strong new evidence for spin-glass physics in the  $x = 0$  LOC sample, even though this system seems to have no apparent structural disorder.

## 3.5 Time dependent magnetization

The time evolution of the isothermal remanent magnetization  $M_{ZFC}(t)$  of the LOC samples has been studied in the following steps. The sample was first cooled in zero field to 2 K (well below the freezing temperature) and then kept in a magnetic field,  $H$ ,

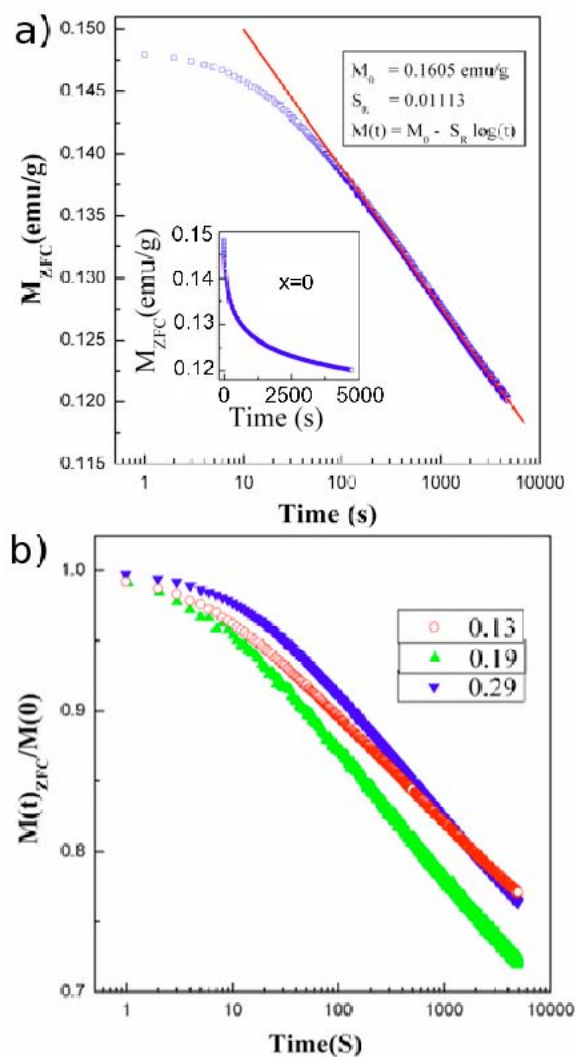


Figure 3.4 Isothermal remanent magnetization  $M_{ZFC}(t)$  vs.  $\log(t)$  at 5000 Oe. a)  $x = 0$ . Inset: The normal plot of  $M_{ZFC}(t)$  for  $x = 0$ . b) The scaled remanent magnetization  $M_{ZFC}(t)/M(0)$  at 5000 Oe for  $x = 0.13, 0.19$  and  $0.29$ .

for 10 minutes. After switching off the applied field, we measured  $M_{ZFC}(t)$  for 5000 seconds. The experiment was repeated in 5 different fields (50 Oe, 500 Oe, 5000 Oe, 10000 Oe and 20000 Oe). The data for 5000 Oe are shown in Fig. 3.4. The time dependence of  $M_{ZFC}(t)$  of the  $x = 0$  sample is plotted in Fig. 3.4 a), in which we observed a long time slow nonexponential relaxation. For  $t < 100s$ ,  $M_{ZFC}(t)$  can be described by  $M_{ZFC}(t) = M_0 - S_R \log(t)$ , in which  $M_0$  is a constant and the coefficient  $S_R$  is the magnetic viscosity. This logarithmic decay law is a characteristic feature of spin glass like systems. In order to better compare the relaxation behaviors of other doped samples, a scaled  $M_{ZFC}(t)/M(0)$  quantity is plotted in Fig. 3.4b) instead of the absolute values. At 5000 seconds, their  $M_{ZFC}(t)$  values slowly decay to 70-80% of the initial values  $M(0)$ . Their long time decay behaviors all follow the logarithmic form with different coefficients  $S_R$ . The time relaxation of  $M_{ZFC}(t)$  under the other 4 fields shows similar behavior and follows a logarithmic decay law after  $t > 100s$ . The initial values  $M_{ZFC}(0)$  increase rapidly with field for  $H < 5kOe$  and slowly approach their saturation value when  $H > 5kOe$ .

## 3.6 Specific heat

Specific heat (C) measurements were performed on a Quantum Design PPMS with the relaxation method [14]. The powder samples were compressed into 10-20mg thin cylindrical disks and attached to a platform by Apiezon N grease. A reference

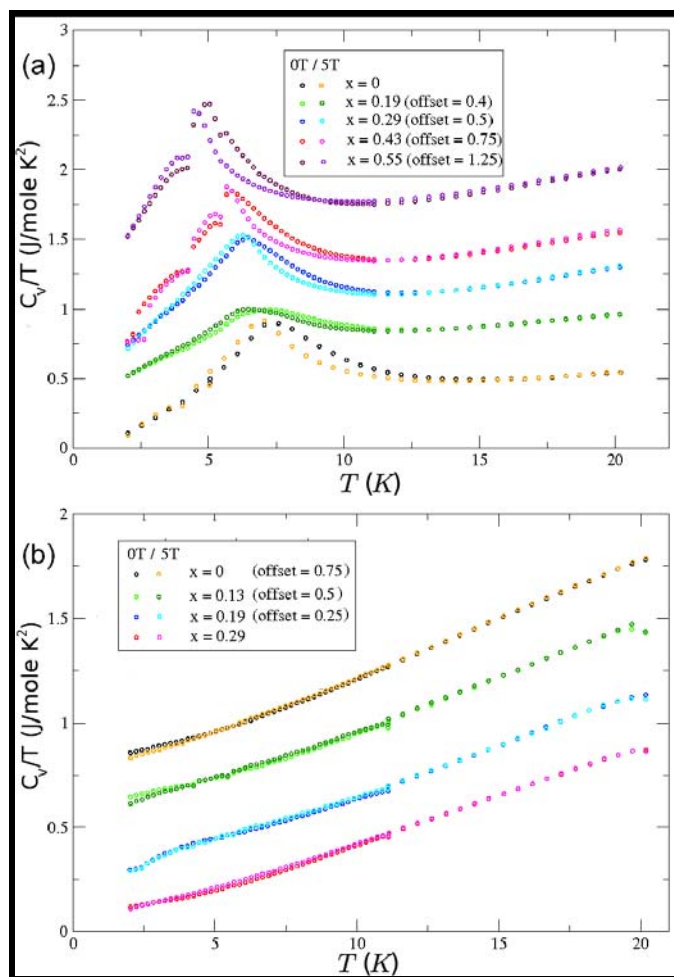


Figure 3.5 Specific heat divided by temperature, for diluted CHN (a) and LOC (b) samples, with and without an applied magnetic field of  $B = 5T$ . Data for different Zn concentration  $x$  are mutually offset for clarity.

measurement was taken first to obtain the heat capacity of the platform and grease. In the following sample measurement, the reference data was subtracted from the total heat capacity yielding the pure sample  $C$ . Fig. 3.5 shows the  $C$  data. Sharp peaks in the diluted CHN data indicate a large amount of entropy loss during the antiferromagnetic phase transitions. This supports a picture based on the existence of conventional long-range magnetic order in the diluted CHN samples. The peak position of  $C/T$  decreases as the Zn doping increases, which is similar to the doping dependence of the DC susceptibility peaks [10]. We should also note that in the temperature range  $2\text{K} < T < 4\text{K}$ , the specific heat has a roughly  $T^2$  behavior. This is also seen up to  $T \approx 20\text{K}$  or more in the LOC data, Fig. 3.5b), as noted for  $x = 0$  in Ref. 5. We caution that since there are no proper nonmagnetic materials with an analogous lattice structure available, the pure magnetic contribution cannot be easily separated. To shed more light on this issue, we compared  $C$  in zero field to that in a field of  $B = 5\text{T}$ , where the Zeeman energy is comparable to the magnetic exchange interaction (see above). This has a pronounced effect on the peak structure in the diluted CHN samples, giving further evidence of the magnetic origin of this peak. On the other hand, the effect of the magnetic field on the overall  $C$  is very small in the LOC samples. The small difference between  $B = 0$  and  $B = 5\text{T}$  is barely visible in Fig. 3.5b), and is found to be of order  $0.1\text{J/mol-K}$ . This small magnetic field dependence indicates that lattice degrees of freedom dominate the  $C$ .

One may attribute this dominance to the large unit cell of the system, especially for the LOC samples, and to the enhanced phonon density of states at low energies due to the approximately two-dimensional character of the system. Furthermore, the magnetic

peak (and the associated field dependence) is seen to be absent in the LOC samples. This is also a common feature seen in many spin glass like systems [13], due to the gradual freezing of spins or spin clusters over a large temperature range. In particular, if spins are locked into large clusters even above  $T_f$ , this may provide an additional explanation why magnetic degrees of freedom do not release much entropy at low temperatures, and contribute relatively little to  $C$  at low- $T$ . From the weak magnetic field dependence, we conclude that the approximate  $T^2$ -behavior of  $C$  is chiefly due to phonons. This is a direct consequence of the quasi-two-dimensional geometry of the system. However, a close inspection of the graphs in Fig. 3.5 b) shows that the low- $T$  limit of  $C/T$  is non-zero, hence implying a weak linear contribution to  $C$ . This is the expected low- $T$  contribution of a spin glass (or structural glass) phase [13, 15].

## 3.7 Discussion

The CHN family of compounds allows a controlled study of the role of non-magnetic impurities in a layered frustrated spin-1/2 compound with glassy behavior. We have given further evidence for the presence of a spin glass phase in the “clean” ( $x = 0$ ) LOC parent compound, and tracked the observed phenomenology as a function of Zn concentration  $x$ . The  $x = 0$  limit in the absence of Zn substitution was seen to be the case where the glassy features were most pronounced. This may strengthen earlier claims according to which the spin glass phase is driven by frustration rather than disorder. It is likely that anisotropy introduced by DM interactions also plays a role in the observed behavior [5, 16], especially in view of the weakness of the energy scale

associated with exchange interactions. We caution that DM terms are particularly sensitive to the symmetry of the local environment, and thus could be more affected by disorder introduced by the organic chains in the LOC samples. Detailed calculations on the strength of these terms and the disorder necessary to reproduce the observed behavior are left for future studies.

A remarkable effect was found to emerge at temperatures above  $T_f$  in the form of two successive power law regimes in the DC susceptibility with sharp crossover. This effect was furthermore seen to be robust against Zn doping, becoming rather more pronounced in the  $x > 0$  samples. The occurrence of power laws above a transition into a glassy state is somewhat reminiscent of the picture developed in Ref.17. There it was argued that a quantum Griffiths phase [18] may be unstable to the formation of a cluster glass phase at low temperatures. Above the transition temperature, the quantum Griffiths behavior is still expected to be seen, which leads to the observation of power laws in thermodynamic quantities as determined in Ref. 19. Specifically, the susceptibility is predicted to be of the form  $\chi \propto T^{\alpha-1}$  with  $\alpha > 0$ . It is feasible that the role of long range RKKY interactions considered in Ref. 17 is played by dipole-dipole interactions in the present case. We note, however, that the value of  $\alpha$  in this scenario is not universal, but is expected to depend on doping [20]. In contrast, the power laws observed here are fairly insensitive to doping which is more suggestive of universal exponents. Furthermore, the quantum Griffiths scenario can at present only explain the occurrence of a single power law with exponent less than 1, and offers no direct explanation for the power law behavior seen at low temperature. To our knowledge, a

crossover between different power laws as seen in the LOC CHN compounds has not been previously observed or predicted, and may well be the hallmark of new physics. The stability of the scaling forms and their insensitivity to doping may indicate self-generated glassiness [21], which may overwhelm doping dependence. A detailed understanding of this behavior and the search for possible incarnations in other systems remain an interesting challenge for future work.

## **3.8 Acknowledgements**

We would like to thank the Center for Materials Innovation for support of this work. AS would like to acknowledge support by the National Science Foundation under NSF Grant No. DMR-0907793, as well as discussions with V. Dobrosavljević.



## **Bibliography**

- [1] J. S. Helton, K. Matan, M. P. Shores, E. A. Nytko, B. M. Bartlett, Y. Yoshida, Y. Takano, A. Suslov, Y. Qiu, J.-H. Chung, et al., *Phys. Rev. Lett.* 98, 107204 (2007).
- [2] D. H. Reich, T. F. Rosenbaum, and G. Aeppli, *Phys. Rev. Lett.* 59, 1969 (1987).
- [3] C. Castelnovo, R. Moessner, and S. L. Sondhi, *Nature* 451, 42 (2008).
- [4] G. G. Linder, M. Atanasov, and J. Pebler, *J. Solid State Chem.* 116, 1 (1995).
- [5] M. A. Girtu, C. M. Wynn, W. Fujita, K. Awaga, and A. J. Epstein, *Phys. Rev. B* 61, 4117 (2000).
- [6] J. G. Bednorz and K. A. Müller, *Rev. Mod. Phys.* 60, 585 (1988).
- [7] M. Rotter, M. Tegel, and D. Johrendt, *Phys. Rev. Lett.* 101, 107006 (2008).
- [8] Z. Fisk, D. W. Hess, C. J. Pethick, D. Pines, J. L. Smith, J. D. Thompson, and J. O. Willis, *Science* 239, 33 (1988).
- [9] C. Varma, Z. Nussinov, and W. v. Saarloos, *Phys. Rep.* 361, 267 (2002).
- [10] J. Wu, A. K. Gangopadhyay, P. Kanjanaboos, and S. A. Solin, *J. Phys. Condens. Matter* 22, 334211 (2010).
- [11] E. Ruiz, M. Llunell, J. Cano, P. Rabu, M. Drillon, and C. Massobrio, *J. Phys. Chem. B* 110, 115 (2006).
- [12] T. Park et al., *Phys. Rev. Lett.* 94, 017002 (2005).
- [13] K. H. Fischer and J. A. Hertz, *Spin Glasses* (Cambridge University Press, 1993).
- [14] R. Bachmann et al., *Rev. Sci. Instrum.* 43, 205 (1972).
- [15] K. Binder and A. P. Young, *Rev. Mod. Phys.* 58, 801 (1986).
- [16] M. F. Collins and O. A. Petrenko, *Can. J. Phys.* 75, 605 (1997).

- [17] V. Dobrosavljević and E. Miranda, Phys. Rev. Lett. 94, 187203 (2005).
- [18] R. B. Griffiths, Phys. Rev. Lett. 23, 17 (1969).
- [19] T. Vojta and J. Schmalian, Phys. Rev. B 72, 045438 (2005).
- [20] M. Brando, T. Westerkamp, M. Deppe, P. Gegenwart, C. Geiberl, and F. Steglich, J. Phys.: Conf. Ser. 200, 012016 (2010).
- [21] H. Westfahl, J. Schmalian, and P. G. Wolynes, Phys. Rev. B 68, 134203 (2003).

## **Chapter 4**

**Magnetism and specific heat of 2D**

**distorted triangular lattice**

**materials:**

**$\text{Cu}_{2(1-x)}\text{Zn}_{2x}(\text{OH})_3\text{NO}_3/(\text{C}_7\text{H}_{15}\text{COO})$**

**$\cdot m\text{H}_2\text{O}$**

## 4.1 Abstract

Magnetic susceptibility and specific heat measurements have been performed on a series of spin  $S = 1/2$  distorted triangular lattice materials  $\text{Cu}_{2(1-x)}\text{Zn}_{2x}(\text{OH})_3\text{NO}_3$  ( $0 \leq x \leq 0.65$ ) and their long chain alkyl carboxylic group intercalated derivatives,  $\text{Cu}_{2(1-x)}\text{Zn}_{2x}(\text{OH})_3(\text{C}_7\text{H}_{15}\text{COO}) \cdot m\text{H}_2\text{O}$  ( $0 \leq x \leq 0.29$ ). We found that antiferromagnetic-type long-range order develops in all the nitrate group compounds below the Neel temperatures  $T_N$ , which decreases with increasing Zn content. For the organic long chain intercalated samples, the temperature dependence of the magnetic susceptibility suggests that the low temperature state is spin-glass-like phase, or more specifically, a cluster glass. Typical glassy behavior is also observed in the time evolution of remanent magnetization data. The specific heat data displaying no visible peaks agrees with many spin-glass-like materials. Moreover, we found the susceptibility follows a power law  $\chi \propto T^{-a}$  with two different exponents  $a$  in two successive regimes above the freezing temperature  $T_f$ , from which we propose that a quantum Griffiths phase could exist in the intermediate temperature regime.

## 4.2 Introduction

The physical properties of low-dimensional frustrated magnets have attracted intensive experimental and theoretical interest for decades, since their highly

degenerate ground states provide fertile ground for new physics [1,2,3]. Many of these studies were carried on triangle-based lattices, in which an interesting phenomenon, geometric frustration, arises due to the contradiction between the periodicity of long-range magnetic order and the lattice geometry. The typical examples of geometric frustration have been found in 2D triangular [4] and Kagomé lattices [5], 3D pyrochlore lattices [6] with nearest-neighbor (NN) antiferromagnetic interactions, or in spin-ice [7] materials with both ferromagnetic NN interactions and strong axial anisotropy.

The study of frustrated materials is significantly driven by the search for unconventional ground states. One well-known example is the NN triangular Heisenberg antiferromagnet (THAF), described by the Hamiltonian

$$H = -J \sum_{\langle i,j \rangle} \mathbf{S}_i \cdot \mathbf{S}_j \quad (1)$$

where  $J < 0$  and  $\langle i,j \rangle$  refers to NN spins. In the classical limit, the ground states exhibit a three sub-lattice long-range order in which the spins are arranged  $120^\circ$  relative to their nearest neighbors. However, at low temperature, quantum fluctuations in small spin systems could be strong enough to destabilize this classical chiral ordered state leading to a liquid like resonating-valence-bond state as firstly proposed by Anderson [8,9]. Numerous works suggests that NN THAF is ordered at zero temperature albeit with a much reduced moment [10,11,12]. However, no final consensus has been reached. Longer range interactions may lead to a spin-liquid ground state. The absence of spin order down to the mK range has been reported on a few materials, such as organic salts  $\kappa$ -(BEDT-TTF)<sub>2</sub>Cu<sub>2</sub>(CN)<sub>3</sub> [13] and Cs<sub>2</sub>CuCl<sub>4</sub> [14] under high magnetic field. However, the nature of the ground state of the THAF is still a controversial question.

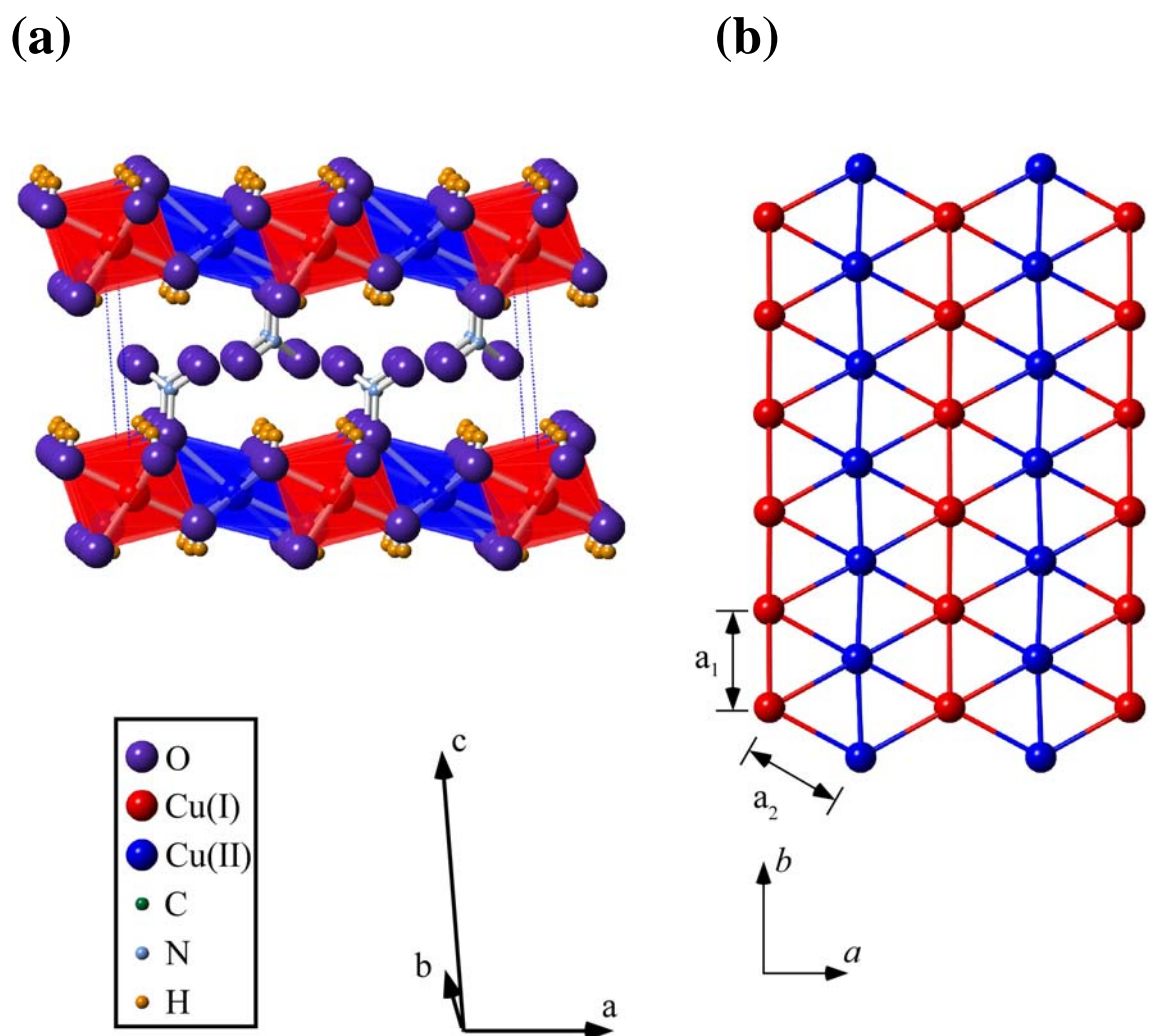


Figure. 4.1 (a) The  $P2_1(4)$  crystal structure of  $\text{Cu}_2(\text{OH})_3\text{NO}_3$ . Each Cu is located in a  $\text{CuO}_6$  octahedron. The Cu(I) sites are connected to 5 OH and 1  $\text{NO}_3$  group while the Cu(II) sites are connected via 4 OH and 2  $\text{NO}_3$  groups. (b) A c-axis view of the distorted triangular Cu layers.

A large category of frustrated materials has been found to display a series of spin-glass-like behaviors at low temperature [15]. Unlike the spin liquid states, the phase space of the spin glass materials is separated by relatively high energy barriers which can't be overcome at low temperature leading to ergodicity breaking. Usually, two physical factors, randomness and frustration, are required simultaneously to make a spin glass [16]. The question of whether a purely frustrated material without structural disorder can afford a spin glass is still open. Data collected on different materials differs due to the various factors, such as inequivalent exchange constants, single ion anisotropies, and Dzyloshinskii-Moriya and long range interactions, which further complicate the question. A well-controlled study of a substitutional system could shed some light on this problem.

In this paper we report an extensive study of the magnetic properties and specific heat of two series of distorted triangular lattice materials  $\text{Cu}_{2(1-x)}\text{Zn}_{2x}(\text{OH})_3\text{NO}_3$  ( $0 \leq x \leq 0.65$ ) and  $\text{Cu}_{2(1-x)}\text{Zn}_{2x}(\text{OH})_3(\text{C}_7\text{H}_{15}\text{COO}) \cdot m\text{H}_2\text{O}$  ( $0 \leq x \leq 0.29$ ). In these samples, the magnetic ions  $\text{Cu}^{2+}$  are gradually substituted by non-magnetic ions  $\text{Zn}^{2+}$ , which affords us the flexibility to tune the average coupling constant. In the following part of this paper, we will name them as nitrate group compounds and long chain intercalated compounds, respectively.

As shown in the schematic view in Fig. 4.1, the botallackite-type compound  $\text{Cu}_2(\text{OH})_3\text{NO}_3$  has a layered structure, in which the adjacent layers are separated by two layers of  $\text{NO}_3$ . In each layer, the  $\text{Cu}^{2+}$  magnetic ions which carry a 1/2 spin are arranged on a distorted triangular lattice with about 3% difference between unit cell parameters  $a$

and *b*. Each  $\text{Cu}^{2+}$  ion is located in a  $\text{CuO}_6^-$  octahedron. Two nearest neighbor  $\text{Cu}^{2+}$ s are coupled by super-exchange interactions through a Cu-O-Cu path. However, two different copper sites Cu(I) and Cu(II) can be differentiated by their slightly different local environments. The non-magnetic  $\text{Zn}^{2+}$  ions can be introduced to replace the  $\text{Cu}^{2+}$  ions [17]. The interlayer  $\text{NO}_3^-$  anions could also be replaced by other monovalent anion groups [17]. In our study, both substitutions were applied in a controlled manner. A long chain alkyl carboxylic group  $\text{C}_7\text{H}_{15}\text{COO}$  was selected in our study to increase the interlayer distance and thus enhance the 2D character. The parent compounds  $\text{Cu}_2(\text{OH})_3\text{NO}_3$  and  $\text{Cu}_2(\text{OH})_3(\text{C}_7\text{H}_{15}\text{COO})\cdot\text{mH}_2\text{O}$  have been previously studied by Linder *et al.*[18] and Gîrțu *et al.*[19]. And the magnetic properties of  $\text{Cu}_{2(1-x)}\text{Zn}_{2x}(\text{OH})_3\text{NO}_3$  and some preliminary results on  $\text{Cu}_{2(1-x)}\text{Zn}_{2x}(\text{OH})_3(\text{C}_7\text{H}_{15}\text{COO})\cdot\text{mH}_2\text{O}$  are reported in our previous paper[20]. In this paper, our focus will be on the long chain intercalated samples.

This paper is organized as follows. In Sec. 4.3 we provide a description of the sample preparation method and experimental procedures. The detailed experimental results and discussion on the magnetic properties and specific heat of above two series materials will be presented in the Sec. 4.4. We end the paper with conclusions in Sec. 4.5.

## 4.3 Experiment

### 4.3.1 Sample preparation



$\text{Cu}_{2(1-x)}\text{Zn}_{2x}(\text{OH})_3\text{NO}_3$  is one of the hydroxy double salts  $(\text{Me},\text{M})_2(\text{OH})_3\text{X}$ , in which Me and M represents two divalent metal ions ( $\text{Cu}^{2+}$ ,  $\text{Zn}^{2+}$ ,  $\text{Mg}^{2+}$ , etc.) and X is a monovalent anion ( $\text{NO}_3^-$ ,  $\text{Cl}^-$ ,  $\text{C}_7\text{H}_{15}\text{COO}^-$ , etc.). The synthesis of Hydroxy double salts is usually accomplished by reacting a solid oxide MeO or  $\text{Me}(\text{OH})_2$  with another metal salt  $\text{MX}_2$  solution[17]. The long chain intercalated samples are made by anion exchange reaction between  $\text{Cu}_{2(1-x)}\text{Zn}_{2x}(\text{OH})_3\text{NO}_3$  and  $\text{C}_7\text{H}_{15}\text{COONa}$  water solution. The details of sample preparation are reported in our previous paper [20].

### 4.3.2 Experiment procedures

The Zn concentrations of the mixed ion samples were analyzed on an Agilent 7500ce Inductively Coupled Plasma Mass Spectrometer (ICP-MS) after the powder samples were dissolved in nitric acid.

The DC magnetic susceptibility was measured by a vibrating sample magnetometer (VSM, PPMS, Quantum Design) equipped with a 9-T superconducting magnet. Before measurement, the powder samples were compressed into cylindrical pellets with ~20mg mass under 50 psi pressures by a hydraulic press. A 2-300 K wide temperature range was employed to study the temperature dependence of magnetic susceptibility of long chain samples was taken under a 500Oe or 5000Oe DC field. In the low temperature range (2K- 50K), two different protocols were applied to investigate the thermal irreversibility of the magnetic susceptibility. In the first situation, the samples were cooled under zero field from 50K to 2K and then the so-call zero-field-cooled (ZFC)

susceptibility was collected in the following warming process under a typical field between 10Oe to 5000Oe. The field-cooled (FC) susceptibility could be measured in the cooling process when a field was applied simultaneously. Since a residual field was always present in the superconducting magnet, the zero field means  $\sim 2$ Oe. The Hysteresis measurements were taken at  $T = 2$ K and 10K under a saw wave field from -5T to 5T. The sample was firstly cooled in zero field to a specific temperature and then the magnetization was collected versus magnetic field.

In the measurement of the time dependence of the magnetization, the sample was cooled in zero field to 2K. Then an external magnetic field  $H$  ( $50 \text{ Oe} < H < 20000 \text{ Oe}$ ) was switched on for 10 minutes. The remanent magnetization  $M_{ZFC}(t)$  was recorded for 5000 seconds after the field  $H$  was changed to 0.

The 2K to 300K specific heat measurements of our samples were performed on a Quantum Design PPMS using the relaxation method [21]. The magnetic specific heat under 5T was taken between 2K and 20K. As in the magnetic susceptibility measurements, the powder samples are compressed into cylindrical disks. The sample mass for specific heat measurement is  $\sim 20$ mg for the nitrate group compounds and  $\sim 10$ mg for the long chain intercalated compounds. The sample disk was attached to the measurement platform with Apiezon N grease to facilitate good thermal contact. The heat capacity data of the addenda with grease was taken before the sample measurement to eliminate the background contribution.

## **4.4 Results and Discussion**

### 4.4.1 Crystal structure

The crystal structure of the basic compound  $\text{Cu}_2(\text{OH})_3\text{NO}_3$  is monoclinic (space group  $\text{P2}_1(4)$ ) with lattice parameters:  $a = 5.605 \text{ \AA}$ ,  $b = 6.087 \text{ \AA}$ ,  $c = 6.929 \text{ \AA}$  and  $\beta = 94.29^\circ$ . The X-ray powder diffraction data of the doped nitrate group compounds indicates that the Zn doped samples still keep the basic framework of the parent compound but with slightly distorted unit cells [22]. The starting ZnO material is only detectable in the  $x = 0.65$  samples. The X-ray powder diffraction patterns of the long chain samples  $\text{Cu}_{2(1-x)}\text{Zn}_{2x}(\text{OH})_3(\text{C}_7\text{H}_{15}\text{COO})\cdot m\text{H}_2\text{O}$  display a series of intense (001)

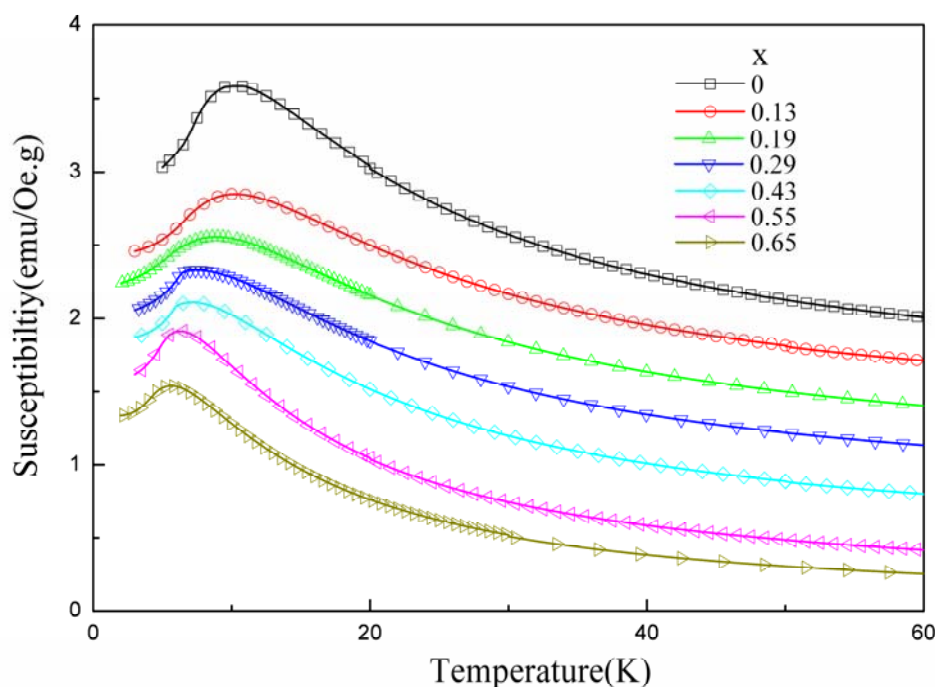


Figure. 4.2 The temperature dependence of the magnetic susceptibility of 7 different  $\text{Cu}_{2(1-x)}\text{Zn}_{2x}(\text{OH})_3\text{NO}_3$  samples. The data are shifted upward by emu/Oe.g amounts of 1.4, 1.2, 0.9, 0.7, 0.4, 0.1, 0 for  $x = 0, 0.13, 0.19, 0.29, 0.43, 0.55$  and  $0.65$ , respectively.

peaks, which is commonly seen in layered compounds. The interlayer distance is expanded to 24.2 Å and almost doping independent [20].

## 4.4.2 Magnetic properties

### 4.4.2.1 Nitrate group compounds $\text{Cu}_{2(1-x)}\text{Zn}_{2x}(\text{OH})_3\text{NO}_3$

Fig. 4.2 shows the temperature dependence of the DC susceptibility of the Zn-doped samples ( $0 \leq x \leq 0.65$ ). When  $T > 50\text{K}$ , the susceptibility of this family of samples follows the Curie-Weiss law  $\chi = C/(T - \Theta_{cw}) + \chi_0$ , in which  $C$ ,  $\Theta_{cw}$  and  $\chi_0$  are the Curie constant, Curie-Weiss temperature and temperature independent contributions. For all the samples, there are peaks occurring at  $T < 15\text{K}$ , indicating the onset of antiferromagnetic correlation. One can clearly see a decreasing trend of the peak positions with the increasing  $\text{Zn}^{2+}$  concentration from 11K for  $x = 0$  to 5.5K for  $x = 0.65$ . This phenomenon can be explained if we note that the  $\text{Zn}^{2+}$  ions don't carry magnetic moments and thus they only dilute the magnetic ion lattice. This dilution of the magnetic lattice decreases the average coupling strength and gradually reduces the magnetic order.

The degree of frustration  $f = |\Theta_{cw}/T_N|$  is  $< 1$  for all these samples if the Neel temperature  $T_N$  is defined as the maximum value of  $|d\chi/dT|$  [23]. This suggests an unfrustrated nature of the nitrate group samples, which differs from the highly frustrated values ( $f > 10$ ) reported in the other triangular lattice antiferromagnetic materials [15]. The imperfection of the triangular lattice and the interlayer interaction may account for the release of frustration. Another thing worth noting is that we observed an increasing

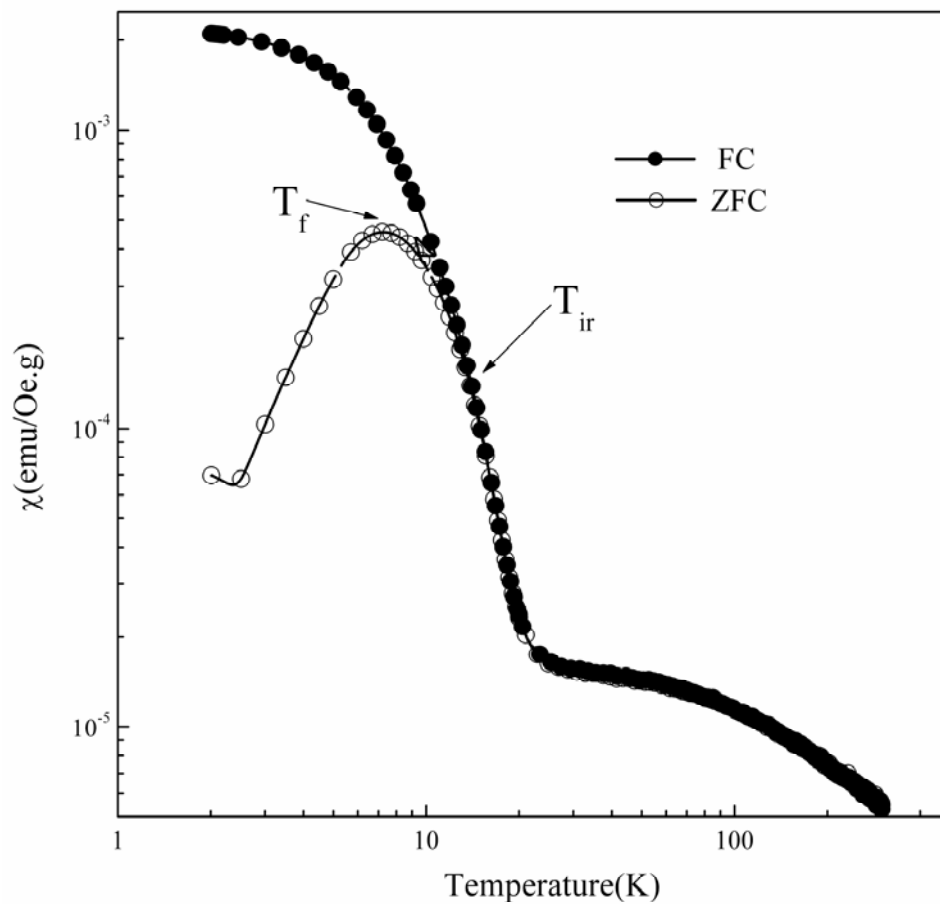


Figure. 4.3. A log-log plot of the temperature dependence of the magnetic susceptibility for the  $x = 0$  long chain intercalated sample.

trend of Landé  $g$  factors with increased Zn content [20]. The anisotropy is enhanced in doped samples, which reflects the change of the spin-orbit interactions induced by structural distortion and Zn doping.

#### 4.4.2.2 $\text{Cu}_{2(1-x)}\text{Zn}_{2x}(\text{OH})_3(\text{C}_7\text{H}_{15}\text{COO})\cdot\text{mH}_2\text{O}$

After the long chain alkyl carboxylic acid group  $\text{C}_7\text{H}_{15}\text{COO}$  was introduced into the interlayer galley valley, the interlayer distance  $24.2 \text{ \AA}$  is  $\sim 3.5$  times the value of the nitrate group compounds. In this case, the dipole-dipole interaction between 2  $\text{Cu}^{2+}$  ions in two layers is negligible [19]. A log-log plot of temperature-dependence of the  $x = 0$  DC magnetic susceptibility is shown in Fig. 4.3. The Curie-Weiss temperature  $\Theta_{cw}$  is  $-94\text{K}$ , which is about 30 times larger than for the  $x = 0$  nitrate compound. However, no peak-like anomaly such as those in the nitrate group compounds is found in  $\chi_{FC}$  at lower temperature as in the Nitrate compounds. A sharp increase in susceptibility was found at  $T = 20\text{K}$  suggesting the occurrence of a strong local ferromagnetic correlation. The absence of long-range ferromagnetic or antiferromagnetic order is obvious in this case, which is evidenced by the huge difference between  $\chi_{FC}$  and  $\chi_{ZFC}$  below  $T_{ir} = 15\text{K}$ . The  $\chi_{ZFC}$  has a rather broad maximum at a freezing temperature  $T_f = 7.2 \text{ K}$ . The onset of irreversibility below  $T_{ir}$  has long been considered a finger print for spin-glass-like materials [16].

Fig. 4.4 (a) shows the temperature dependence of  $\chi_{FC} - \chi_{ZFC}$  for all the 4 samples ( $x = 0, 0.13, 0.19, 0.29$ ) in the  $2 \text{ K} < T < 20 \text{ K}$  range under a magnetic field of  $H = 100\text{Oe}$ . The other 3 Zn doped long chain intercalated samples also demonstrate clear glassy

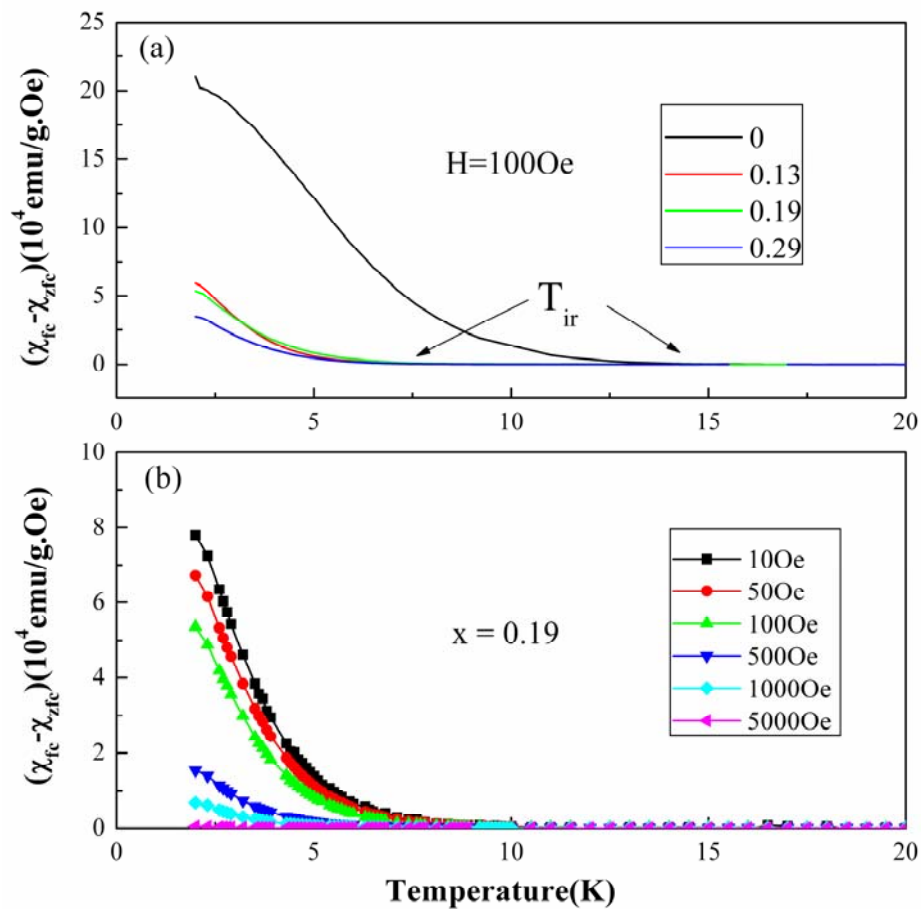


Figure. 4.4. (a) The difference between  $\chi_{FC}$  and  $\chi_{ZFC}$  in the  $2\text{K} < T < 20\text{K}$  range for 4 different organic long chain intercalated samples. (b) The difference between  $\chi_{FC}$  and  $\chi_{ZFC}$  for the  $x = 0.19$  organic long chain intercalated sample under 6 different magnetic fields.

behavior. At  $T = 2\text{K}$ , the magnitude of  $\chi_{\text{FC}} - \chi_{\text{ZFC}}$  attenuates with increasing Zn concentration.

The temperature  $T_{\text{ir}}$  of the other 3 doped samples is in 7~9 K range, which is significantly smaller than that of the  $x = 0$  sample. The divergence of  $\chi_{\text{FC}}$  and  $\chi_{\text{ZFC}}$  has a magnetic field dependence. The  $x = 0.19$  sample is selected as a typical example as shown in Fig. 4.4 (b). The thermomagnetic irreversibility is suppressed by the high magnetic field and  $T_{\text{ir}}$  is shifted to lower temperature with increasing field  $H$ . When the applied magnetic field is above 5000Oe, the thermomagnetic irreversibility is completely removed. We should mention that this is also true for the  $x = 0.13$  and 0.29 samples. However, we could still observe a nonzero value of  $\chi_{\text{FC}} - \chi_{\text{ZFC}}$  for the  $x = 0$  sample even at 5000Oe. This suggests that the  $x = 0$  sample has the stiffest glassiness. A further observation of the details of the susceptibility data suggests that the long chain intercalated samples are more similar to a cluster-glass [24, 25] rather than to the canonical spin-glass. For all 4 samples, the freezing temperature  $T_{\text{f}}$  is well below  $T_{\text{ir}}$  while in the canonical spin-glass  $T_{\text{ir}}$  is very close to, but still below,  $T_{\text{f}}$  [16]. Furthermore,  $\chi_{\text{FC}}$  continues to increase even below  $T_{\text{f}}$  instead of saturating as in the canonical spin-glass.

Another important feature we found is that the DC susceptibility data follows a distinct power laws  $\chi \propto T^{-a}$  in 3 temperature regimes above the freezing temperature  $T_{\text{f}}$ . The log-log plot of  $\chi_{\text{ZFC}}$  vs. temperature is shown in Fig. 4.5 for 4 long chain intercalated samples. The regime I starts from a little above  $T_{\text{f}}$  and ends at about 20 K for the  $x = 0$  sample, and at 14K for the doped samples. The exponent,  $a$ , obtained for



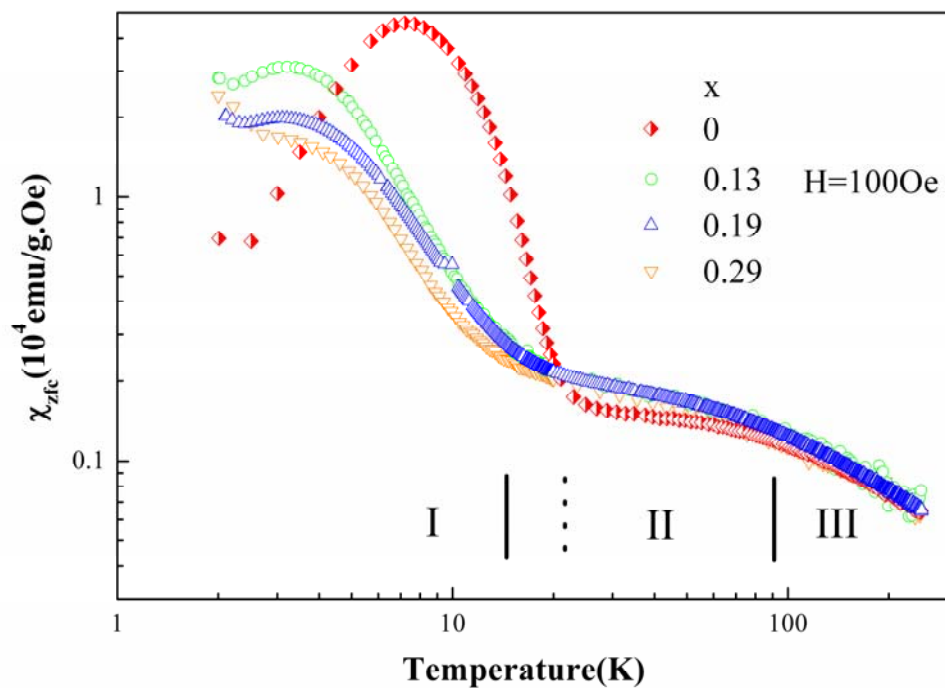


Figure. 4.5. A log-log plot of  $\chi_{ZFC}$  vs. temperature for 4 organic long chain intercalated samples ( $x = 0, 0.13, 0.19$  and  $0.29$ ). The approximate boundaries of 3 regimes are labeled in the figure. The dashed and solid lines are the boundaries between I and II for the  $x = 0$  and  $x > 0$  samples, respectively.

$x=0$  is  $\sim 5$  and in the range  $1.7 < a < 2.2$  for other doped samples. The upper boundary of regime II is  $\sim 90\text{K}$ , in which the exponent  $a$  dramatically drops to  $0.2 < a < 0.3$ . In regime III, the curves exhibit Curie-Weiss tails with the exponents close to 1. Since the lower boundary of regime I is below  $T_{\text{ir}}$ , the exponents in regime I calculated with  $\chi_{\text{FC}}$  data are slightly larger than the above values. However, this will not alter the observation that there is a distinct crossover in power law exponents,  $a$ , from regime I to II. We believe this is a reflection of the distinct spin dynamics in these two regimes. The experimental results we observed here are similar to the theoretical picture proposed by Dobrosavljević *et. al.* [26], in which a quantum Griffiths phase evolves into a cluster-glass phase at low temperature. In particular, the magnetic susceptibility of the quantum Griffiths phase is predicted to follow the form  $\chi \propto T^{\alpha-1}$  with  $\alpha > 0$  [27], which agrees with our results in regime II. We also note that the upper boundary of regime II is close to  $\Theta_{\text{cw}}$ . This suggests that the occurrence of a quantum Griffiths phase is somehow related to a frustration effect, which disables the conventional long-range order at  $\Theta_{\text{cw}}$ . Instead of the formation of a long-range order, the small spin clusters start to nucleate at  $\Theta_{\text{cw}}$  and finally these clusters grow into a cluster-glass below  $T_{\text{ir}}$ .

To further investigate the magnetic irreversibility at low temperatures, we performed a detailed study of the hysteresis of the magnetization  $M(H)$ . The  $M(H)$  curves at  $T = 2\text{K}$  and  $10\text{K}$  for 4 long chain intercalated samples are plotted in Fig. 4.6(a) and 6(b), respectively. At  $T = 2\text{K}$ , a large hysteresis loop with coercive field  $H_C = 3200\text{Oe}$  was observed for the  $x = 0$  sample. The coercive field  $H_C$  decreases with increasing Zn doping to  $630\text{Oe}$ ,  $580\text{Oe}$  and  $390\text{Oe}$ , for  $x = 0.13$ ,  $0.19$  and  $0.29$ , respectively. When

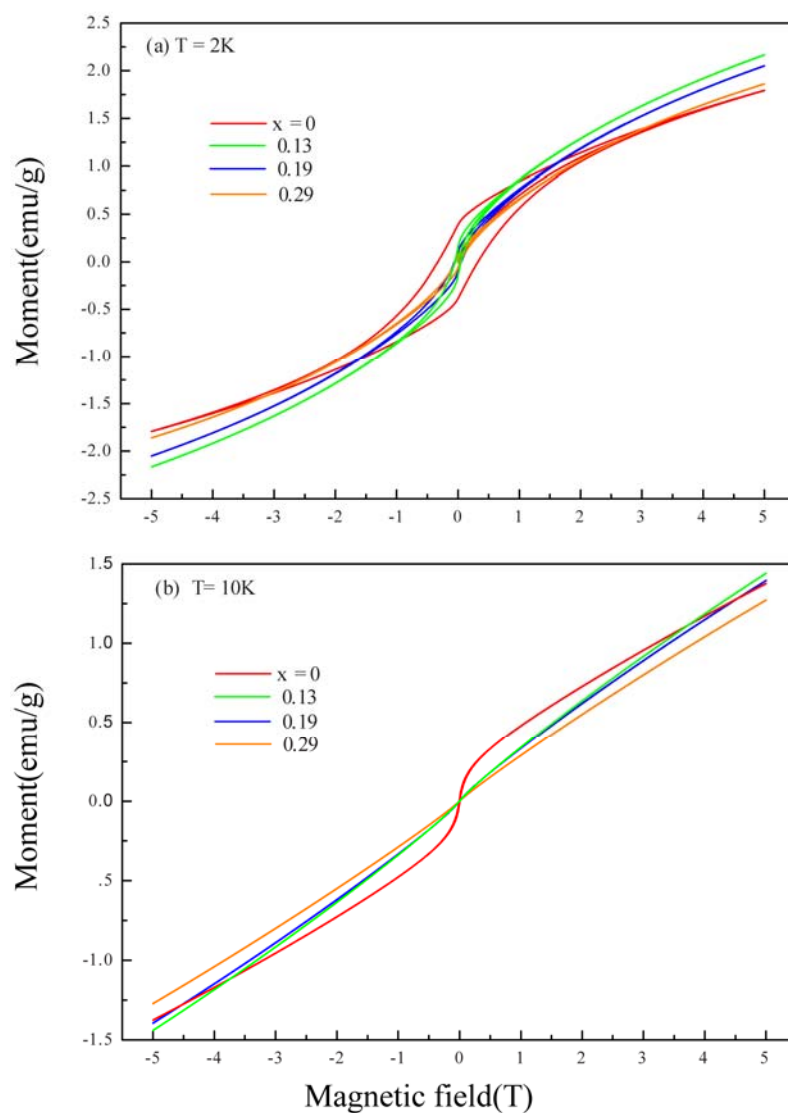


Figure 4.6. (a) The  $M(H)$  curves for 4 organic long chain intercalated samples ( $x = 0$ , 0.13, 0.19 and 0.29) at  $T = 2K$ . (b) The  $M(H)$  curves for 4 organic long chain intercalated samples ( $x = 0$ , 0.13, 0.19 and 0.29) at  $T = 10K$ .

the temperature is raised to 10K, the  $M(H)$  curves for all  $x > 0$  samples only exhibit a nearly linear  $H$  dependence. However, a clear S-shaped curvature is still seen in the  $x = 0$  sample with a coercive field  $H_C = 70\text{Oe}$ . The selected temperature 10K is below  $T_{ir}$  for  $x = 0$  but above  $T_{ir}$  for  $x > 0$ , which suggests that spin clusters are not growing to a size big enough to induce hysteresis until  $T < T_{ir}$ . None of the samples reaches magnetic saturation up to  $B = 5\text{T}$  at  $T = 2\text{K}$ . Instead, the  $M(H)$  curves at  $T = 2\text{K}$  can be separated into two parts: the hysteresis loop and the high field linear tail. Hence, the saturation values of the ferromagnetic part, which could be obtained by extrapolation from the high field region, are 1560 emu G/mol-Cu, 1820 emu G/mol-Cu, 1890 emu G/mol-Cu, and 1650 emu-G/mol Cu for  $x = 0$ ,  $x = 0.13$ ,  $x = 0.19$  and  $x = 0.29$ , respectively [28]. All the above experimental values are smaller than the expected saturation value 5585 emu G/mol for a spin  $S = 1/2$  ferromagnet [19]. A possible explanation for the difference in coercive fields could be generated with the cluster-glass picture. Due to the presence of nonmagnetic  $\text{Zn}^{2+}$  ions, the  $x > 0$  samples have relatively small cluster size. So it is easier to flip the spin direction in these smaller clusters resulting in smaller coercive fields in the  $x > 0$  samples. However, the doping dependence of the saturation value is more complicate and requires further effort to understand.

Finally, we have investigated the time evolution of the isothermal remanent magnetization  $M_{ZFC}(t)$ . In order to compare the time relaxation effect of 4 long chain intercalated samples, we plot a scaled quantity  $M_{ZFC}(t)/M_{ZFC}(0)$  measured under  $H = 5000\text{Oe}$  in Fig. 4.7(a). When  $t > 100\text{s}$ , all the  $M_{ZFC}(t)$  curves could be fit to following form,

$$M_{ZFC}(t) = M_0 - S_R \log(t)$$

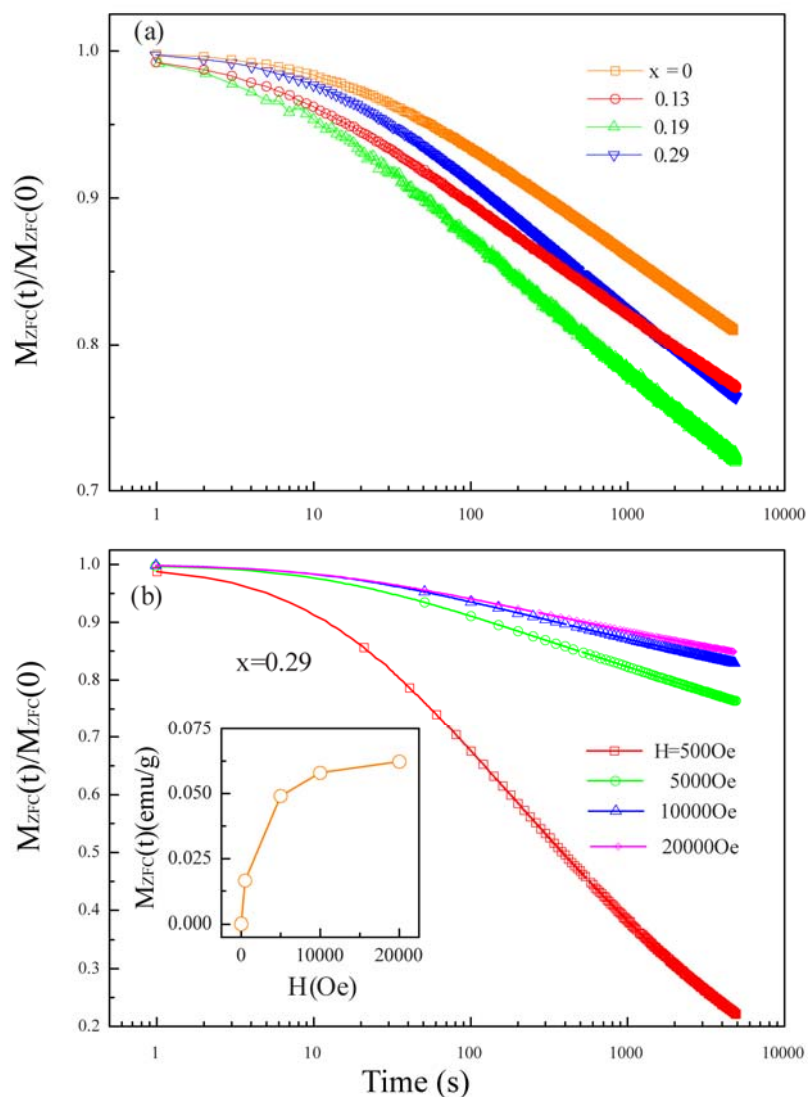


Figure. 4.7 (a) The scaled quantity  $M_{ZFC}(t)/M_{ZFC}(0)$  measured under  $H = 5000$  Oe for 4 organic long chain intercalated samples ( $x = 0, 0.13, 0.19$  and  $0.29$ ) (b) Main panel: The field-dependence of the scaled quantity  $M_{ZFC}(t)/M_{ZFC}(0)$  of the  $x = 0.29$ . Inset: The field-dependence of the initial value  $M_{ZFC}(0)$  of  $x = 0.29$ .

where  $M_0$  is a constant and the coefficient  $S_R$  is the magnetic viscosity. This logarithmic decay formula was previously used to characterize a category of spin-glass like systems [16]. The slope in our plot in the  $100s < t < 5000s$  range is the scaled magnetic viscosity  $S_R / M_{ZFC}(0)$ . The slopes are calculated to be -0.073, -0.075, -0.087 and -0.087 for  $x = 0, 0.13, 0.19$  and  $0.29$ , respectively, which can be divided into 2 groups. The Zn-rich samples seem to relax faster than the low doping samples. The logarithmic decay could extend to a longer time and we found no sign that  $M_{ZFC}(t)$  approaches a stable value. Fig. 4.7(b) compares the relaxation behaviors of the  $x = 0.29$  sample under 4 different applied magnetic fields. The final value  $M_{ZFC}(5000) / M_{ZFC}(0)$  decreases with increasing magnetic field  $H$ . In the case of  $H = 500\text{Oe}$ ,  $M_{ZFC}(5000)$  reaches 20% of its initial values  $M_{ZFC}(0)$  while in the  $H > 10\text{kOe}$   $M_{ZFC}(t)$  only relaxes by 80-90%. The magnetic field dependence of the initial value of  $M_{ZFC}(0)$  for  $x = 0.29$  is shown in Fig. 4.7(b) inset. The  $M_{ZFC}(0)$  increases rapidly when  $H < 5\text{kOe}$  and gradually approaches a saturation value when  $H > 10\text{kOe}$ . A similar field dependence of  $M_{ZFC}(t)$  is also found for the other 3 long chain intercalated samples.

### 4.4.3 Specific heat

#### 4.4.3.1 Nitrate group compounds $\text{Cu}_{2(1-x)}\text{Zn}_{2x}(\text{OH})_3\text{NO}_3$

A log-log plot of the specific heat  $C$  vs. temperature for the nitrate group compounds is shown in Fig. 4.8(a). The separation of the magnetic contribution from the lattice contribution is impractical in the present case since no proper reference material such as a pure Zn compound is available. Sharp peak anomalies appear in the range  $5\sim 8\text{K}$ , which

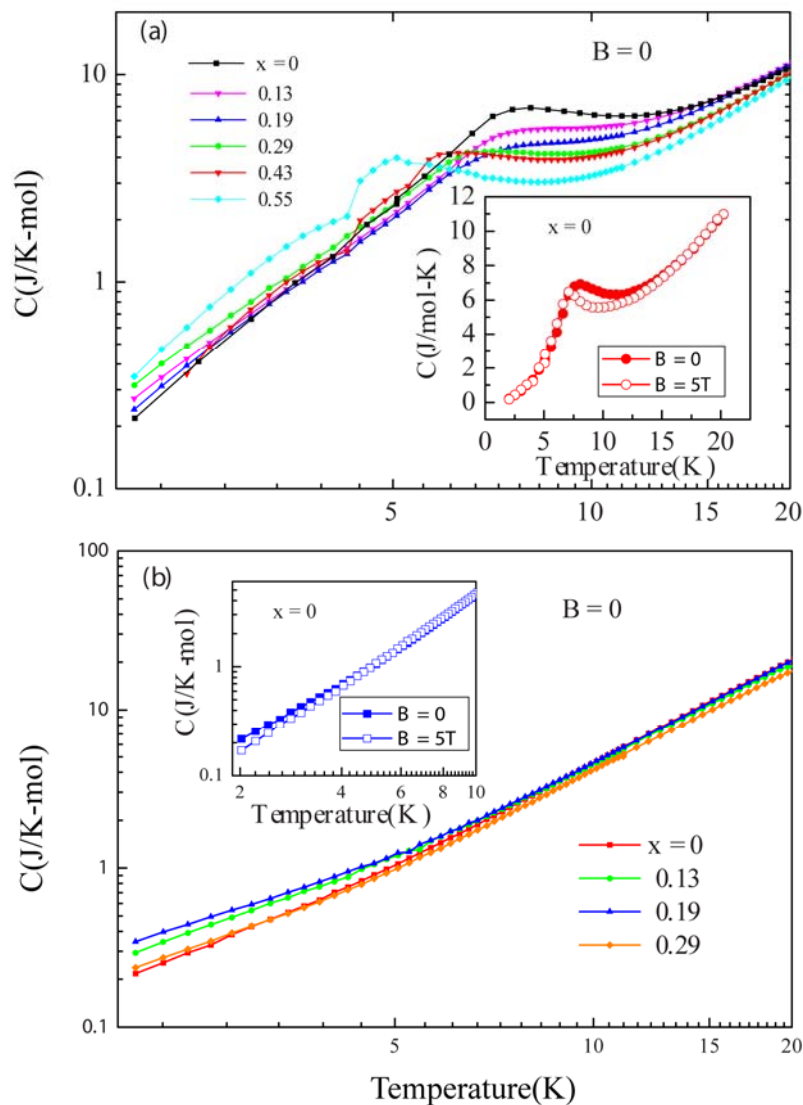


Figure. 4.8 (a) Main panel: A log-log plot of the specific heat data for 6 nitrate group samples. Inset: A comparison between the  $B = 0$  and 5T specific heat data of the  $x = 0$  nitrate group sample. (b) Main panel: A log-log plot of the specific data for 4 organic long chain intercalated samples. Inset: A comparison between the  $B = 0$  and 5T specific heat data of the  $x = 0$  organic long chain intercalated sample.

are close to their corresponding  $T_N$  determined in the magnetic susceptibility measurement. The occurrence of these sharp peaks confirms that long-range antiferromagnetic order is well established in the nitrate group materials. The peak position of the specific heat curves decreases with increasing Zn content, which is also a consequence of dilution of the magnetic lattice. The inset of Fig. 4.8(a) shows a comparison between the specific heat  $C$  in the  $B = 0$  and 5T cases for the  $x = 0$  sample. The difference between the two curves is mainly in  $4\text{K} < T < 15\text{K}$  temperature window, in which the phase transitions occurs. The peak is slightly shifted down by  $\sim 0.5\text{K}$ . This confirms the magnetic origin of these peaks although the separation of lattice contribution is not performed. It is worth noting that the specific heat follows a power law  $C \propto T^\beta$  above and below the transition where  $\beta$  can be obtained by a linear fit in the log-log plot. The exponents  $\beta$  are 1.3, 1.4, 1.6, 1.7, 1.7 and 1.9 before transition and 2.6, 2.3, 2.3, 2.2, 2.4 and 2.5 after transition for the  $x = 0, 0.13, 0.19, 0.29, 0.43$  and  $0.55$  samples, respectively. This is probably an indication that there is 3D ordering present after the phase transition as discussed in Linder's paper [18].

#### 4.4.4.2 $\text{Cu}_{2(1-x)}\text{Zn}_{2x}(\text{OH})_3(\text{C}_7\text{H}_{15}\text{COO})\cdot m\text{H}_2\text{O}$

A log-log plot of  $C$  vs.  $T$  for 4 long chain intercalated samples ( $x = 0, 0.13, 0.19$  and  $0.29$ ) is shown in Fig. 4.8(b). No distinct peak features were observed down to the lowest temperature 2K. The absence of strong features in the specific heat is common in other spin-glass-like materials [16,29]. An entropy loss may happen in the gradual freezing of spins or spin clusters over a large temperature range as seen in many



spin-glass-like systems. However, there is a noticeable change in slope around  $T = 6$  K for all 4 samples. In the  $6\text{K} < T < 20\text{K}$  region, the calculated exponent  $\beta$  values are 2.1~2.2, which are nearly doping independent. In the  $2\text{K} < T < 6\text{K}$  region, the exponents  $\beta$  values decrease to 1.5~1.8. The high-T specific heat has an approximate  $T^2$  dependence, whose origin could be 2D phonon or antiferromagnetic spin waves on a 2D lattice [19]. In order to exam the above 2 possibilities, we measured the specific heat under  $B = 5\text{T}$ . The comparison between the  $B = 0$  and  $5\text{T}$  specific heat data for  $x = 0$  is shown in Fig. 4.8(b) inset. The two curves are nearly identical above 6K. Similar results are also observed in other doped samples. These results would strongly support the 2D phonon explanation of the  $T^2$  behavior. The divergence between the  $B = 0$  and  $5\text{T}$  curve becomes noticeable when  $T < 4\text{K}$ , which would encourage us to consider the magnetic contribution to the total specific heat in this regime. Apparently the exponent  $\beta$  has a decreasing trend with decreasing temperature. The low-T specific heat of spin glass was previously predicted to have linear dependence on temperature [29]. So it is very possible that the specific will approaches the  $T^1$  limit at lower temperature.

## 4.5 Conclusions

The focus of this paper is the long chain intercalated samples  $\text{Cu}_{2(1-x)}\text{Zn}_{2x}(\text{OH})_3(\text{C}_7\text{H}_{15}\text{COO})\cdot m\text{H}_2\text{O}$  ( $0 \leq x \leq 0.29$ ), which have been intentionally synthesized to improve the 2D character of the triangular  $\text{Cu}^{2+}$  layers. The series of nitrate group materials are shown to exhibit conventional long-range order. Although the Curie-Weiss temperatures of the long chain intercalated samples are found to be one

order of magnitude above that of their nitrate group analogues, the long-range order is not stabilized at low temperature. Instead, a set of spin-glass like behaviors are observed: (1) The prominent bifurcation between  $\chi_{FC}$  and  $\chi_{ZFC}$  below  $T_{ir}$ ; (2) A hysteresis effect found in the  $M(H)$  curves; (3) The logarithmic decay law of the time dependence of the isothermal remanent magnetization  $M_{ZFC}(t)$  (4) The lack of visible peaks in the specific heat data all support this notion. A detailed inspection of the DC susceptibility would suggest the long chain intercalated samples are cluster-glasses when  $T < T_{ir}$ . We also found that the susceptibility in the intermediate regime (regime II) follows a power law  $\chi \propto T^{\alpha-1}$  with  $\alpha > 0$ , which we could directly link to an earlier prediction of a Quantum Griffiths phase. We should note that both frustration effects and long-range interactions between spin-clusters may play an important role in this regime. It will be very interesting to construct a detailed model in future to study the rich physics of the long chain intercalated samples.

## 4.6 Acknowledgements

We thank Washington University Center for Materials Innovation (CMI) for seed funding support for this work.

## Bibliography

- [1] P. Schiffer, *Nature* **420**, 35 (2002).
- [2] R. Moessner, and J. T. Chalker, *Phys. Rev. B.* **58**, 12049 (1998).
- [3] L. Balents, *Nature* **464**, 199 (2010).
- [4] M. F. Collins, and O. A. Petrenko, *Can. J. Phys.* **75**, 605 (1997).
- [5] J. S. Helton, K. Matan, M. P. Shores, E. A. Nytko, B. M. Bartlett, Y. Yoshida, Y. Takano, A. Suslov, Y. Qiu, J. H. Chung, D. G. Nocera, and Y. S. Lee, *Phys. Rev. Lett.* **98**, 107204 (2007).
- [6] J. S. Gardner, M. J. P. Gingras, and John E. Greedan, *Rev. Mod. Phys.* **82**, 53 (2010).
- [7] S. T. Bramwell, and M. J. P. Gingras, *Science* **294**, 5546 (2001).
- [8] P. W. Anderson, *Matter. Res. Bull* **8**, 153(1973).
- [9] P. Fazekas, and P. W. Anderson, *Phil. Mag.* **30**, 423(1974).
- [10] D. A. Huse, and V. Elser, *Phys. Rev. Lett.* **60**, 2532534 (1988).
- [11] P. Azaria, B. Delamotte, and D. Mouhanna, *Phys. Rev. Lett.* **70**, 2483 (1993).
- [12] N. Elstner, R. R. P. Singh, and A. P. Young, *Phys. Rev. Lett.* **71**, 1629 (1993).
- [13] Y. Shimizu, K. Miyagawa, K. Kanoda, M. Maesato, and G. Saito, *Phys. Rev. Lett.* **91**, 107001 (2003).
- [14] R. Coldea, D.A. Tennant, A.M. Tsvelik, and Z. Tylczynski, *Phys. Rev. Lett.*, **86**, 1335 (2001).
- [15] A. P. Ramirez, *Annu. Rev. Matter. Sci.* **24**, 453 (1994).
- [16] K. Binder and A. P. Young, *Rev. Mod. Phys.* **58**, 801 (1986).
- [17] M. Meyn, K. Beneke, and G. Lagaly, *Inorg. Chem.* **32**, 1209 (1993).

- [18] G. G. Linder, M. Atanasov, and J. Pebler, *J. Solid State Chem.* **116**, 1 (1995).
- [19] M. A. Gîrțu, C. M. Wynn, W. Fujita, K. Awaga, and A. J. Epstein, *Phys. Rev. B* **61**, 4117 (2000).
- [20] J. Wu, A. K. Gangopadhyay, P. Kanjanaboos, and S. A. Solin, *J. Phys. Condens. Matter* **22**, 334211 (2010).
- [21] R. Bachmann et al., *Rev. Sci. Instrum.* **43**, 205 (1972).
- [22] H. Heffenberger, *Z. Krist.* **165** 127 (1983).
- [23] L-Q. Yan, F. Maciá, Z-W. Jiang, J. Shen, L-H. He, and F-W. Wang, *J. Phys.:Condens. Matter.* **20**, 255203 (2008)
- [24] N. Marcano, Sal. J. C. Gómez, J. I. Espeso, Barquín. L. Fernández, and C. Paulsen, *Phys. Rev. B* **76**, 224419 (2007).
- [25] S. Mukherjee, R. Ranganathan, P. S. Anilkumar, and P. A. Joy, *Phys. Rev. B* **54**, 9267 (1996).
- [26] V. Dobrosavljević and E. Miranda, *Phys. Rev. Lett.* **94**, 187203 (2005).
- [27] T. Vojta and J. Schmalian, *Phys. Rev. B* **72**, 045438 (2005).
- [28] K. Vijayanandhini, Ch. Simon, V. Pralong, V. Caignaert, and B. Raveau, *Phys. Rev. B* **79**, 224407 (2009)
- [29] K. H. Fischer and J. A. Hertz, *Spin Glasses* (Cambridge University Press, 1993).

# Chapter 5

## Summary

We have successfully synthesized the powder and single crystal sample of a distorted triangular lattice material  $\text{Cu}_2(\text{OH})_3\text{NO}_3$ , using the hydrothermal synthesis at ambient and high pressure, respectively. Based on this start material, we introduce the nonmagnetic  $\text{Zn}^{2+}$  to dilute its magnetic lattice and modify the average coupling strength. Furthermore, an organic long chain group  $\text{C}_7\text{H}_{15}\text{COO}$  is intercalated into the above materials to enhance the 2D Characters, which has been proven to have big influence on the low temperature phase in our study.

The above materials were first characterized by X-ray diffraction analysis to confirm its structural similarities to the start material, and ICP-MS to find out the real Zn concentration in the materials. After that, the magnetic properties, including temperature dependence of DC and AC susceptibility, magnetic hysteresis and time evolution of remanent magnetization, and specific heat of the above samples have been carefully studied.

The nitrate group samples,  $\text{Cu}_{2(1-x)}\text{Zn}_{2x}(\text{OH})_3\text{NO}_3$ , all exhibit clear phase transitions to antiferromagnet at various Neel temperatures  $T_N$ , which decrease with increase Zn doping. The calculation of the degree of frustration strongly suggests its unfrustrated nature. This is also supported by the specific heat data, which displays a series of prominent peaks at temperature close to their Neel temperatures. Close examinations of specific heat suggests that there might be a 3D ordering at lower temperatures due to the interlayer couplings.

The organic long chain intercalated samples,  $\text{Cu}_{2(1-x)}\text{Zn}_{2x}(\text{OH})_3(\text{C}_7\text{H}_{15}\text{COO})_m\text{H}_2\text{O}$ , with negligible interlayer interactions, are found to show spin-glass-like behaviors. The big bifurcation between ZFC and FC susceptibility appears below  $T < 15\text{K}$ . The relaxation of remnant magnetization confirms glassiness. That is the linear dependence of  $\ln(t)$  of remnant magnetization when  $t > 100\text{s}$ . Further evidence comes from the AC susceptibility data, in which the real component follows  $\chi' = \chi_0 - c \ln(\omega)$ . Unlike the nitrate group samples, the specific heat only displays some weak features due to the slow freezing of spins. The analysis on the details of DC susceptibility suggests the low temperature state is cluster glass, in which short range order is present. A sharp increase in DC susceptibility is an indication of this short-range ferromagnetic correlation. In addition, we also notice that in the temperature range  $T_f < T < |\Theta_{CW}|$ ,  $\chi \propto T^{\alpha-1}$  with  $\alpha > 0$ , which agrees with the previous predication of Quantum Griffiths phases. This suggests that a Quantum Griffiths phase exist at higher temperature and evolve into cluster glass state below  $T_{ir}$ . All the above results are not independent of doping. However, those major observations are pretty robust.

The above two class of materials belong to the Zoology of triangular lattice materials, which have attracted intense attentions. In future, it is very interesting to fully investigate their AC susceptibility in the cluster glass temperature regime and the possible Quantum Griffiths phase regime, to gain a full picture of the evolution of spin dynamics. Other experimental techniques, such as NMR and neutron scattering, may also bring new findings. Especially, collaborating with theoretical efforts, these future experimental studies may shred some lights to the underlying nature of the transition from a Quantum Griffiths phase to a cluster glass state.

## **Part II**

# **Extraordinary Electroconductance in metal-semiconductor hybrid structures**



# Chapter 6

## Introduction to Extraordinary

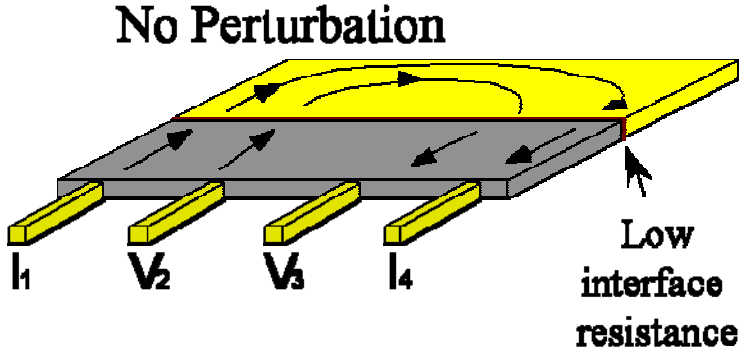
## Effects

### 6.1 General principle

The Extraordinary effect (EXX) is a name given to a class of geometry-driven effects in metal-semiconductor hybrid structures. To date the XX are MR (magnetoconductance), PC (piezoconductance), OC (optoconductance) and EC (electroconductance), which are named by the external perturbations applied to the devices. In the series of devices with EXX effects, we could observe a large change in device conductance with and without the above external perturbations.

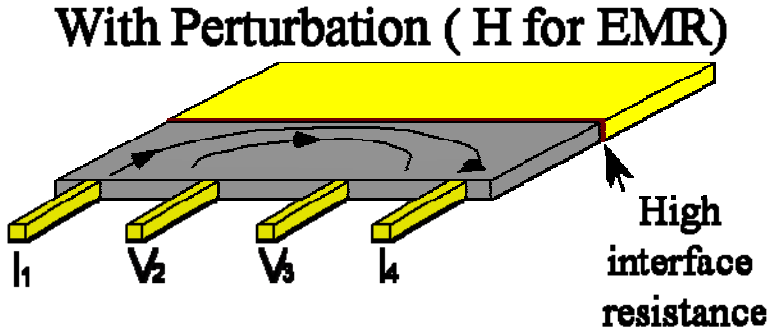
The basic principle of EXX effects is described by Fig 6.1, in which a metal-

(a)



$$R'_{eff} = \frac{V'_{23}}{I'_{14}} \approx R_M$$

(b)



$$R_{eff} = \frac{V_{23}}{I_{14}} \approx R_S$$

Figure 6.1 General Principle of EXX effects. (a) A metal-semiconductor structure without perturbations (b) with perturbation. The current is excluded from the metal part due to the high interface resistance.

semiconductor hybrid structure is displayed. If no external perturbation is applied, the current is flowing into the metal side through the interface. If an external perturbation is applied, which results in a high interface resistance, the current path will be significantly changed. In an extreme case as shown in Fig. 6.1(b), the current is completely excluded from the metal. The effective resistance of this metal hybrid structure can be measured by the four-lead arrangements as shown in Fig. 6.1 as,

$$R_{eff} = \frac{V_{23}}{I_{14}} \quad (6.1)$$

Since the resistivity  $\rho_S \sim 1000\rho_M$ , the effective resistance measured in the Fig. 6.1(b) case,  $R_{eff}$ , can be much larger than that of Fig. 6.1(a),  $R'_{eff}$ .

The central idea of an EXX device is to try to maximize the change in effective resistance caused by the external perturbation, by modifying the geometric factors such as the shape of the metal and semiconductor (rectangular or circular), size, interface curvature, lead arrangements etc. Since the large change in resistance is observed due to the external perturbation, the EXX device can be used as a micro- or nano- size sensor of magnetic fields, strain, photon, or electric fields. In the following subsections, we will briefly discuss 3 of them, EMR, EPC and EOC. The fourth member, EEC, will be discussed in detail in Chapter 7 and 8.

## 6.2 Extraordinary Magnetoresistance

The first example of an EXX effect is Extraordinary Magnetoresistance (EMR), which was discovered by Solin and coworkers in 2000 [1]. As shown in Fig. 6.2(a), the central

part of the EMR device is a 1.3  $\mu\text{m}$  disk of nonmagnetic narrow-gap semiconductor material InSb with an embedded concentric Au disk. This hybrid structure was deposited on a 4-inch semi-insulating GaAs substrate with a 200nm buffer layer of undoped InSb in between. A van der PauW (vdP) four-lead configuration was adopted

to measure the resistance  $R = \frac{V_{23}}{I_{14}}$ . A filling factor  $\alpha$  is defined as

$$\alpha = r_a / r_b \quad (6.2)$$

where the  $r_a$  and  $r_b$  are the inside and outside disk radii as labeled in Fig 6.2(a). The EMR effect is then defined as the percentage of the change with and without magnetic field H at certain  $\alpha$ ,

$$\frac{R(H, \alpha) - R(0, \alpha)}{R(0, \alpha)} \times 100\% \quad (6.3)$$

The largest room temperature EMR effect observed is  $\sim 10^6\%$  for the  $\alpha = 13/16$  device at a magnetic field H= 4-5T. Even at a lower field H = 0.25T, the EMR of the  $\alpha = 13/16$  sample is still as high as 9100%. The numbers are significantly higher than the MR effects observed in layered magnetic metals [1].

The origin of so large EMR effect is the current redistribution induced by the magnetic field, which has been enhanced by this particular geometry. Without the magnetic field H, the conductivity tensor of the semiconductor is diagonal. The electric field is always perpendicular to the metal surface. Hence, for H = 0, the current will follow the direction the electric field line and flow into the metal Au. This corresponds to relatively low resistance. At a high magnetic field, the electric current vector  $\vec{J}$  is

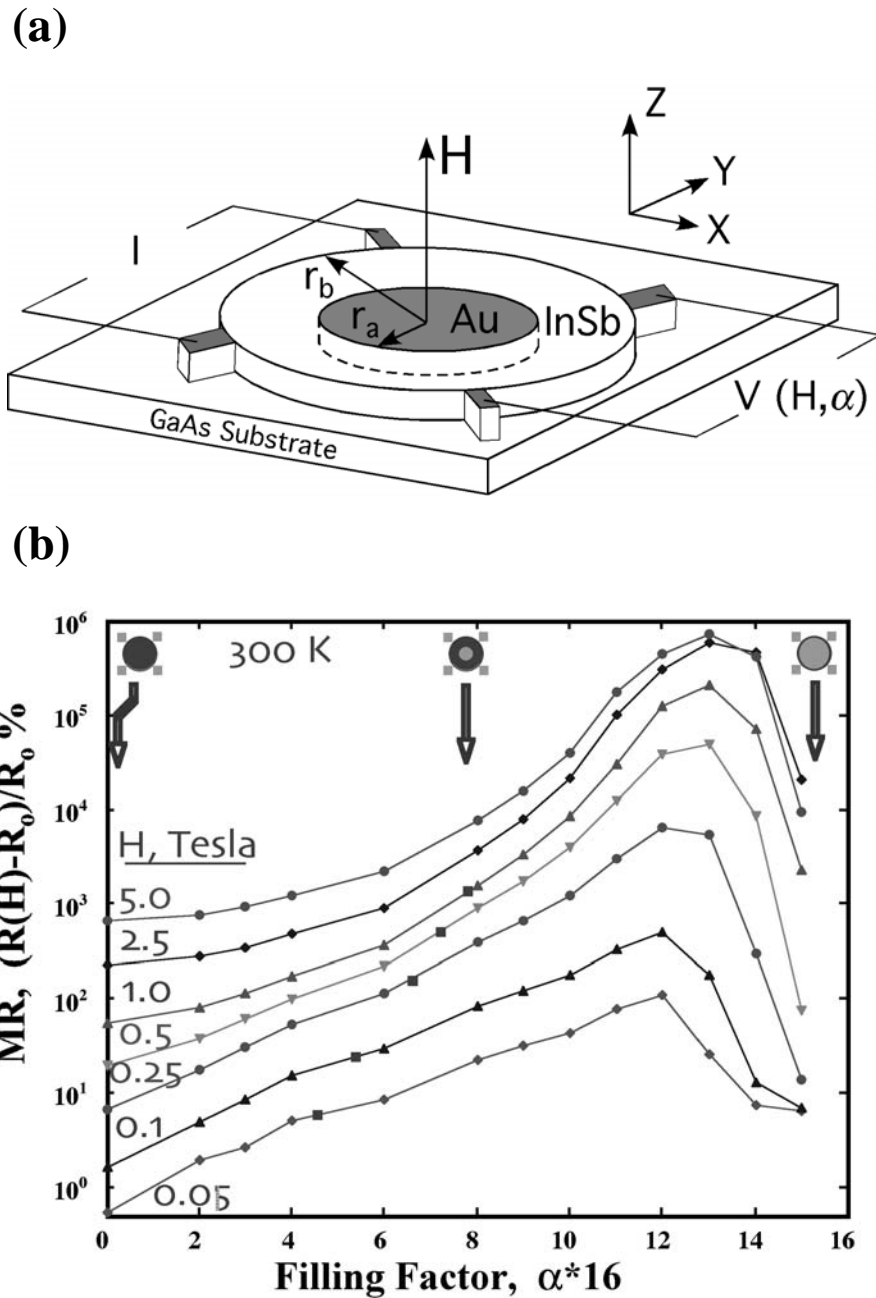


Figure. 6.2 (a) A schematic diagram of a homogeneous InSb vdP disk (radius  $r_b$ ) with an embedded cylindrical Au inhomogeneity (radius  $r_a$ ). (b) The observed room temperature EMR versus filling factor,  $\alpha$ , of the above hybrid structure under different magnetic fields. (After ref. 1)

no longer parallel to the local electric field  $\vec{E}$ . Instead the current will be deflected away from the metal-semiconductor interface. In the extreme case, the angle between  $\vec{J}$  and  $\vec{E}$  is close to  $90^\circ$ , which means the current is almost completely removed from the metal. The current can only flow through the narrow annular semiconductor ring. We should remember that the resistivity of InSb in this situation is  $1.893 \times 10^4 \Omega^{-1}m^{-1}$  while the resistivity of Au is  $4.517 \times 10^7 \Omega^{-1}m^{-1}$ . This 3 order of magnitude difference in resistivity and current redistribution essentially account for the large EMR effect observed in this hybrid structure.

Although the proof-of-principle experiment was done on a circular geometry, the EMR effect could be realized in other configurations as discussed in ref. 2. One of the many applications of the EMR effect is nano-size read head sensors for ultra-high-density magnetic recording.

## 6.3 Extraordinary Piezoconductance

The second member of the EXX family is Extraordinary Piezoconductance (EPC), which was firstly demonstrated on a rectangular geometry at room temperature as shown in Fig. 6.3 [3]. A maximum of  $\sim 10\%$  change in metal-semiconductor conductance was achieved when a tensile strain up to  $5 \times 10^{-4}$  is applied parallel to the metal-semiconductor interface. The origin of EPC is similar to EMR, which is the effect of the current redistribution caused by the strain.

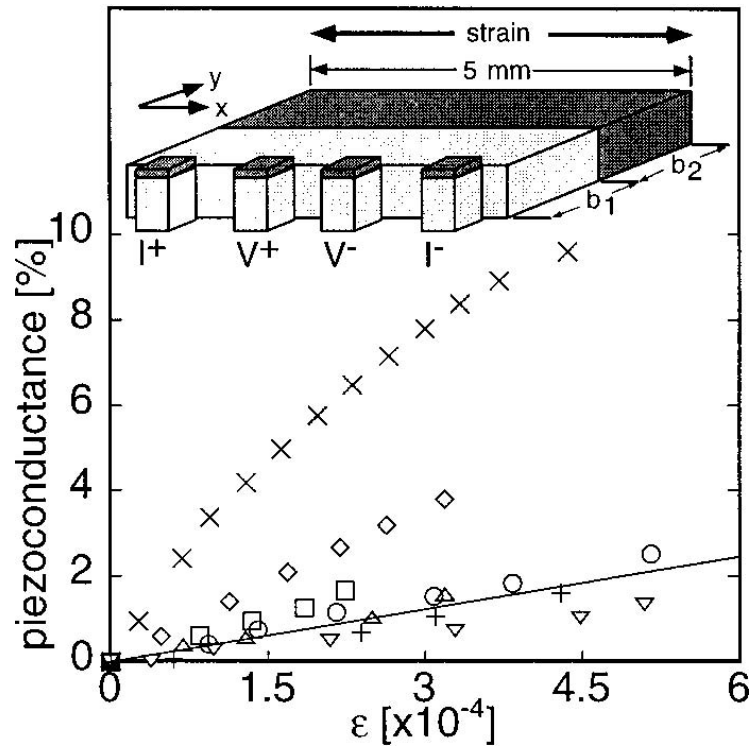


Fig. 6.3 The strain dependence of the piezoconductance measured in a metal-semiconductor hybrid structure with several different values of  $\alpha$  at room temperature. The symbols correspond to  $16\alpha = 0$ ,  $\circ$ ; 6,  $\square$ ; 8,  $\diamond$ ; 9,  $\times$ ; 12,  $\triangle$ ; 13,  $\nabla$ ; 15,  $+$ ; and homogeneous semiconductor alone (solid line). The inset is a schematic view of the device. (After ref. 3)

## 6.4 Extraordinary Optoconductance

Followed by the EMR and EPC, a third member of the EXX family, EOC was discovered in 2004 for a rectangular device as shown in Fig. 6.4 [4]. The device was realized at macroscopic size ( $10\text{ mm} \times 2\text{ mm} \times 400\text{ }\mu\text{m}$ ) with a metal-semiconductor interface between GaAs and In. The external optic perturbation is applied by a focused laser beam with wavelength  $\lambda = 476.5\text{ nm}$ . The EOC effect increases with a decreasing temperature and the maximum EOC effect observed is  $\sim 500\%$  at  $T = 30\text{ K}$ .

Interestingly, the resistance of the EOC devices has a dependence on the position of the focused laser spot. So it is possible to utilize the principle of EOC in a position sensor.

## 6.5 The Schottky Interface

The fourth member of EXX effect, Extraordinary Electroconductance (EEC), is significantly different from the previous three. The metal-semiconductor interface in an EEC device is no longer Ohmic but of the Schottky-type. Therefore, we will briefly discuss the physics of a Schottky interface in this section.

The Schottky Interface is formed at a heterojunction, such as metal-semiconductor or semiconductor-semiconductor interface, which has rectifying characteristics. A schematic view of the band diagram of a metal-semiconductor interface is shown in Fig. 6.5.



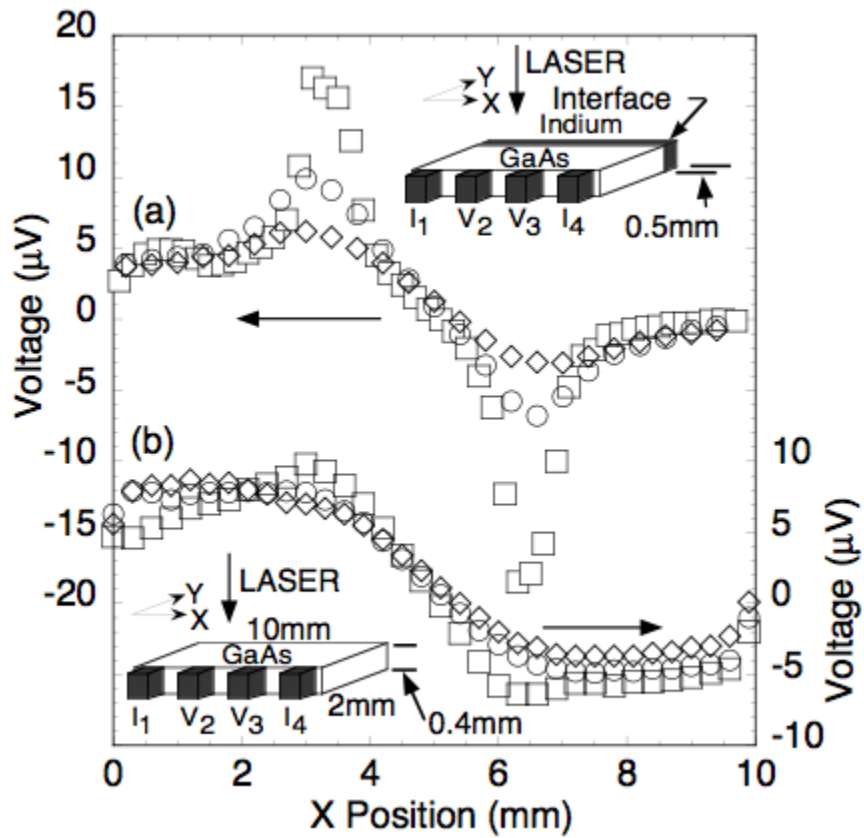


Figure 6.4 Main panels: The position ( $x$ ) dependent voltage measurements,  $V_{23}$ , of (a) an In-GaAs device and (b) a bare GaAs sample acquired under identical conditions at  $T = 15$  K and with 20 mW of 476.5 nm laser radiation focused onto the sample surface.

(After ref. 4)

Before contacting, a n-type semiconductor and a metal have different Fermi levels and work functions  $\phi_m$  and  $\phi_s$ , which are the energy required for an electron to escape to vacuum. When a contact is formed between them, electrons flow to the entity with larger work function (lower Fermi level) until a unifying Fermi level is formed throughout the whole hybrid structure. In the situation shown in Fig. 6.5, the current is flowing from the semiconductor to metal side, which leaves a thin positively charged regime in semiconductor side. This is called the depletion regime. The separation of positive and negative charge induces a strong internal electric field  $\vec{E}$  pointing from semiconductor to the metal side. And this internal electric field causes a built-in potential drop  $V_i$  across the depletion regime and bends the band of the semiconductor near the junction as shown in Fig. 6.5(b). Hence, a Schottky barrier is formed with a barrier height  $\phi_B = \phi_m - \chi_s$ , where  $\chi_s$  is the electron affinity of semiconductor and  $\phi_B$  is the potential barrier an electron must overcome to move to semiconductor side. The width of depletion regime is given by

$$W = \sqrt{2\varepsilon V_i / \rho} \quad (6.4)$$

where  $\varepsilon$  is the semiconductor dielectric constant and  $\rho$  is the electric charge density. In the presence of an external voltage bias, the depletion regime width can be increased or decreased depending on the direction of bias. In the depletion regime, the current carrier is depleted and thus an electric current is forbidden. Hence the electroconductance is then sensitive to the external electric field. This is the working principle of the EEC devices, which will be discussed in detail in the following two chapters.

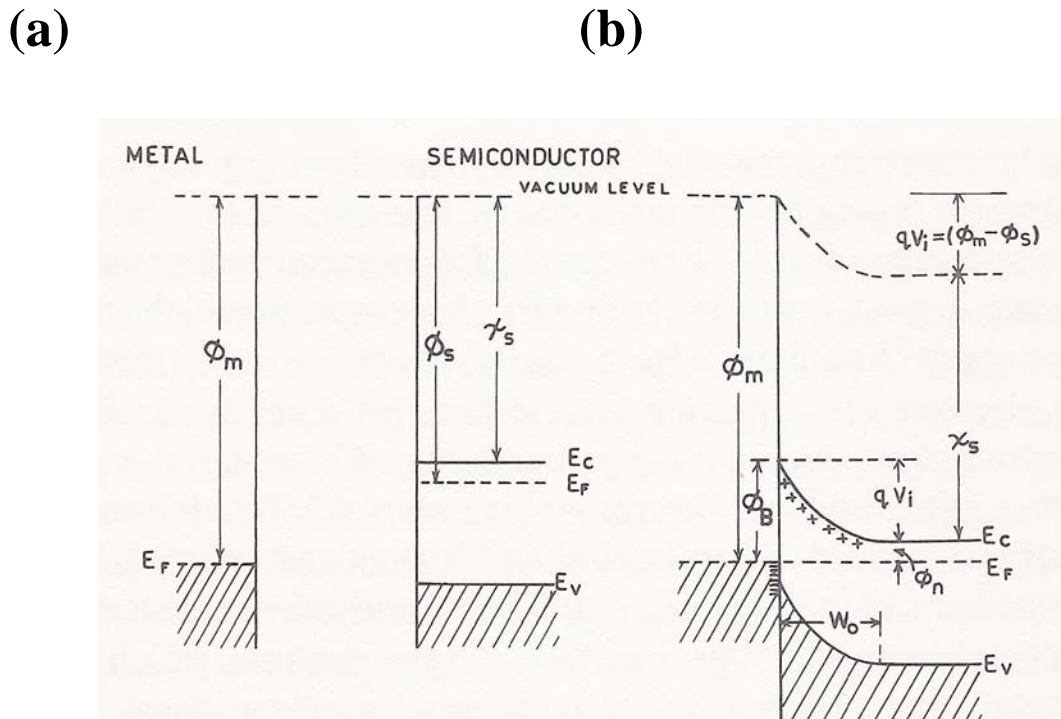


Figure 6.5 (a) The band diagram of an isolated metal and semiconductor. (b) The band diagram of the metal and n-type semiconductor junction.  $E_F$ ,  $E_C$  and  $E_V$  are the Fermi level, conduction band and valence band, respectively.  $\phi_m$  and  $\phi_s$  are the work functions for the metal and semiconductor.  $V_i$  is the built-in potentials.  $\chi_s$  is the electron affinity of the semiconductor, which is the difference between the vacuum and the conduction band. (After Ref. 5)

## **Bibliography**

- [1] S. A. Solin, D.R.Hines, T. Thio and J. Heremans, *Science* **289**, 1530 (2000).
- [2] S. A. Solin, D. R. Hines, J. S. Tsai, Yu. A. Pashkin, S. J. Chung, N. Goel and M. B. Santos, *Appl. Phys. Lett.* **80**, 4012 (2002).
- [3] A. C. H. Rowe, D. R. Hines, and S. A. Solin, *Appl. Phys. Lett.* **83**, 1160 (2003).
- [4] K. A. Wieland, Yun Wang, L. R. Ram-Mohan, S. A. Solin, and A. M. Girgis, *Appl. Phys. Lett.* **88**, 052105 (2006).
- [5] B. L. Sharma, *Metal-Semiconductor Schottky Barrier Junctions and Their Applications*, page 3(Plenum, New York, 1984).

# **Chapter 7**

## **Extraordinary Electroconductance in Metal-Semiconductor Hybrid Structures**

### **7.1 Abstract**

We report the phenomenon of extraordinary electroconductance in microscopic metal-semiconductor hybrid structures fabricated from GaAs epitaxial layer and a Ti thin film shunt. Four-lead Van der Pauw structures show a gain of 5.2 % in electroconductance under +2.5 kV/cm with zero shunt bias. The increase in the sample conductance results from the thermionic field emission of electrons and the geometrical amplification. A model provides good agreement with the experimental data and clearly demonstrates the geometry dependence of the field effect in EEC. The differences

between EEC devices and field effect transistors, such as JFET and MESFET, are discussed.

## 7.2 Introduction

Electrical transport in any device depends on both the physical or intrinsic properties such as the carrier concentration, etc. and the extrinsic geometric properties such as the shape of the device, etc [1]. Normally, transport studies focus on the physical properties and samples are designed to minimize the geometric contributions. However, Solin and coworkers have shown that by careful design, the geometric contributions can be made dominant and have demonstrated a class of EXX phenomena, where E = extraordinary and, to date, XX = magnetoresistance (MR) [2;3], piezoconductance (PC) [4;5] and optoconductance (OC) [6;7]. Here we report another type of EXX phenomenon, extraordinary electroconductance (EEC), which is based on the geometric amplification of the physical properties of a Schottky interface using a metal-semiconductor hybrid structure (MSH).\_

## 7.3 Device Preparation

The MSH structures were fabricated from a 2-inch (100) GaAs substrate (resistivity  $\rho > 1 \times 10^{15}$  ohm·m, thickness  $t = 350$   $\mu\text{m}$ ) with an epitaxially-grown Si-doped n-GaAs layer ( $N_D = 4 \times 10^{17}$   $\text{cm}^{-3}$ ,  $t = 200$  nm). Four equally spaced Au/Ge ohmic leads are surface deposited on the periphery of the mesa disk. A circular opening 100 nm in

depth was patterned concentrically on the GaAs mesa and a disk-shaped Ti thin film ( $t = 50$  nm) was deposited. An additional 50nm Au/Ge was deposited as a current shunt. With deliberate control of the metal deposition rate and surface passivation, a Schottky barrier was formed at the interface. To apply the electric field directly, a pair of thin metal plates is built into the device. One, made of Au/Ge, was deposited on top of the shunt metal with a layer of  $\text{Si}_3\text{N}_4$  ( $t = 1$   $\mu\text{m}$ ) in between, while the other was obtained by metalizing the bottom surface of the substrate. Two sets of devices with different mesa radius, 100 $\mu\text{m}$  and 60 $\mu\text{m}$ , are studied. Fig. 7.1(a) and (b) show the sample structure. In this study, a four-point AC lock-in measurement was used with current passing through leads 1 and 4 (common ground) and the voltage sensing between leads 2 and 3. The external field is in the range  $-2.5$  kV/cm  $\leq E \leq +2.5$  kV/cm.

## 7.4 Experiment

For a MS system with  $5 \times 10^{16} \text{ cm}^{-3} \leq N_D \leq 5 \times 10^{17} \text{ cm}^{-3}$ , thermionic field emission dominates current transport across the interface at room temperature [8]. The total current density can be expressed as,  $I = I_s [\exp(qV / nkT) - 1]$  where  $I_s$  is the saturation current which is a complicated function of barrier height, semiconductor properties, and temperature. The ideal factor for the Schottky interface is defined as  $n \equiv (q / kT) [\partial V / \partial (\ln I)]$ .

The deviation of real Schottky interface from the ideal can be attributed to many effects, such as electron trapping and recombination [9], barrier inhomogeneities [10],

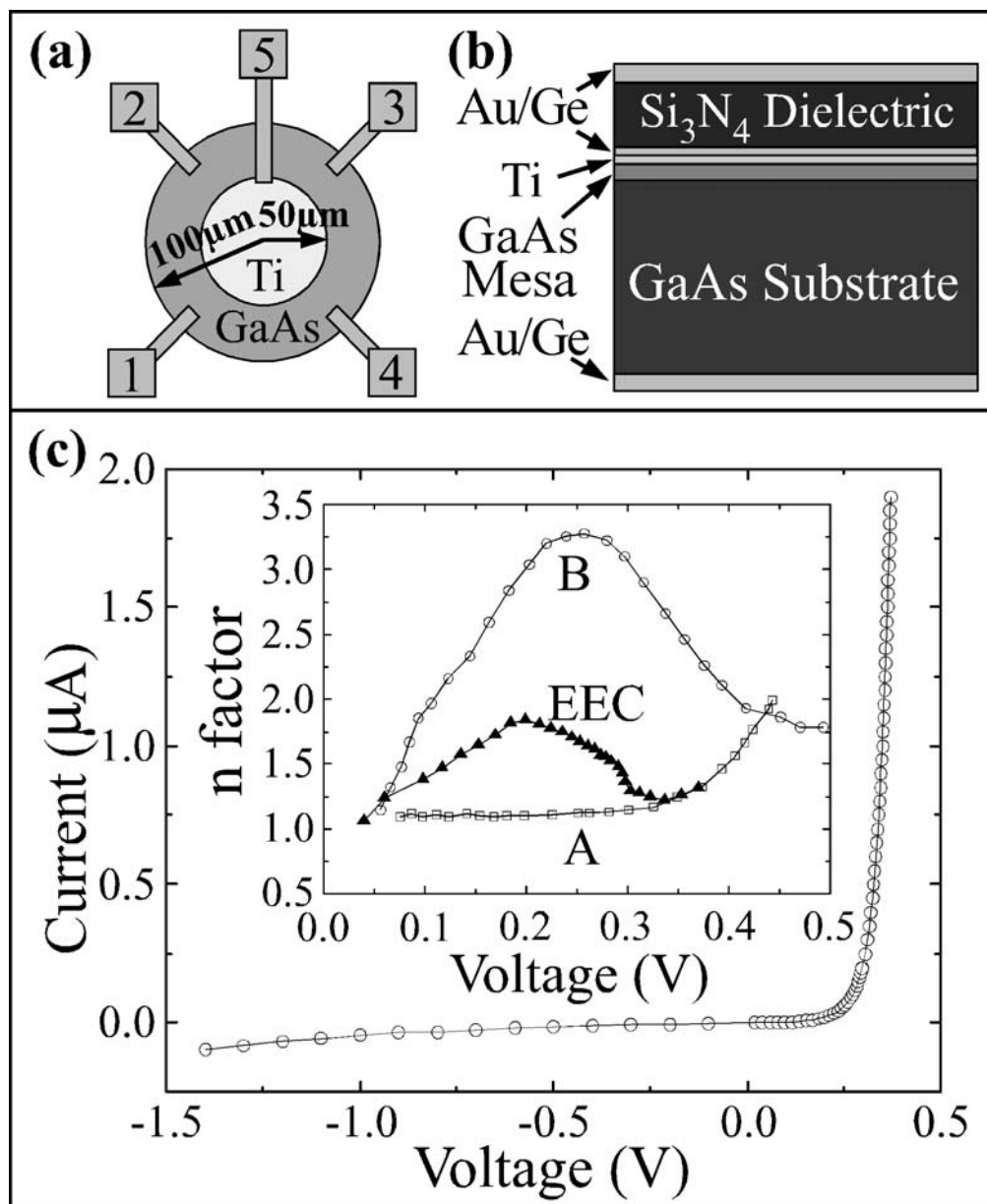


Figure. 7.1. Panels (a) and (b) – Schematics, respectively, of the top view and side view of an EEC device with  $R = 100 \mu\text{m}$  and  $r = 50 \mu\text{m}$ . Panel (c) – The room temperature I-V characteristic of the Schottky interface. Inset – ideal factor  $n$  from a typical EEC device, an ideal Schottky diode, A and a Schottky diode with a thick oxide interfacial layer, B. (A and B are adapted from Ref. 30). The lines are guides to the eye.



interfacial oxide layer [11], image force lowering [12], and series resistance [13]. In a two-terminal Schottky I-V measurement, comparing to an ideal Schottky diode, the EEC device has a larger series resistance arising from the uncovered annulus shaped GaAs region between leads 5 and 4. This excess series resistance and the possible presence of a thin oxide layer at the GaAs-Ti interface contribute to the non-ideal behavior of the MS interface. The main panel of Fig. 7.1(c) shows the I-V characteristic of the Schottky interface while the inset compares the factor  $n$  of a typical EEC device with an ideal Schottky diode A and non-ideal diode B with a thick oxide interfacial layer. According to Ellis *et. al.* [13], the equivalent circuits of a real Schottky diode, like EEC devices, can be represented by two ideal diodes in parallel, each with associated series resistance. In fact, from the inset of Fig. 7.1(c), the ideal factor of the EEC is approximately a linear combination of those of samples A and B. Detailed discussion of this point will be provided elsewhere [14].

The main panel of Fig. 7.2 shows the field dependence of the device resistance under a series of shunt biases from -0.4 V to +0.5 V between leads 5 and 4. The sample resistance is a function of both the external electric field  $E$  and shunt bias  $V_B$ , i.e.  $R(E, V_B)$ . Under a constant  $V_B$ , the resistance monotonically decreases as  $E$  increases and there is a one-to-one correspondence between  $R$  and  $E$ . On the other hand, for a fixed  $E$ , the resistance is substantially decreased when  $V_B > +0.2$  V, as the forward shunt bias diminishes the depletion region [15] at the MS interface. The inset of Fig. 7.2 shows the device sensitivity, defined as  $-(1/R)(dR/dE)$ , with respect to  $E$  as a function of  $V_B$ . The maximum sensitivity,  $\sim 4$  %cm/kV, is obtained at -0.3 kV/cm. Note that, for  $E > -1$  kV/cm,

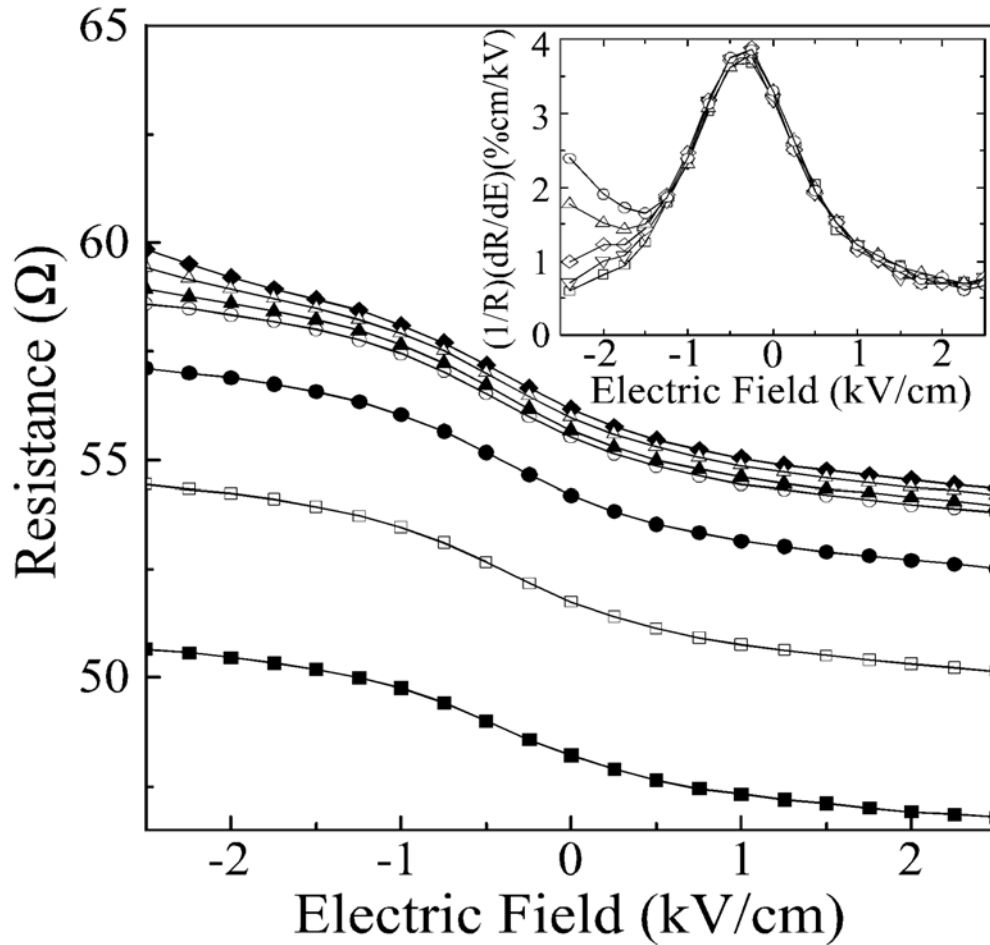


Figure. 7.2. Main panel – The room temperature 4-lead resistance of a sample with  $R = 100 \mu\text{m}$  and  $\alpha = 1/16$  under for  $-2.5 \text{ kV/cm} \leq E \leq +2.5 \text{ kV/cm}$ . The symbols have the following designations:  $V_B = -0.4 \text{ V}$ , ◆;  $-0.2 \text{ V}$ , △;  $0 \text{ V}$ , ▲;  $+0.2 \text{ V}$ , ○;  $+0.4 \text{ V}$ , ●;  $+0.45 \text{ V}$ , □; and  $+0.5 \text{ V}$ , ■. Inset – The sensitivity of the device for  $V_B = -0.4 \text{ V}$ , ○;  $-0.2 \text{ V}$ , △;  $0 \text{ V}$ , ◇;  $+0.2 \text{ V}$ , ▽;  $+0.4 \text{ V}$ , □.

the sensitivity of this device is independent of  $V_B$ . With our current measurement set up, for  $E = 2$  kV/cm, a 0.7 % change in field intensity can be detected. Similar to other EXX entities, geometry plays an important role in the transport properties of the EEC device. For a Van der Pauw disk structure, we define a parameter  $\alpha$  as the ratio of the shunt radius to the mesa radius, i.e.  $\alpha = R_{shunt}/R_{mesa}$ . The room temperature EEC is defined to be the percentage change in sample conductance  $G = I_{14}/V_{23}$  with and without an external electric field.

$$EEC(E, \alpha) = |G(E, \alpha) - G(0, \alpha)| / [G(0, \alpha)] * 100\% \quad (7.1)$$

Fig. 7.3 shows the calculated EEC for 4 different devices with a fixed 100  $\mu\text{m}$  mesa radius and  $\alpha$  of 1/16, 5/16, 10/16 and 14/16. The device with  $\alpha = 1/16$  exhibits the largest EEC effect in both forward and reverse field bias and the largest EEC effect,  $\sim 5.2\%$ , is obtained at a field of 2.5 kV/cm. As  $\alpha$  decreases, the EEC increases. Since mesoscopic effects will prevent divergence of the EEC it must have a maximum at reduced  $\alpha$ . We have not yet determined that maximum due to the feature size limitation ( $\sim 5$   $\mu\text{m}$ ) of our optical lithography. This determination will be made with future devices fabricated with e-beam lithography.

## 7.5 A 2-Layer Analytical Model

Traditionally, the p-n junction field effect transistor (JFET) [16] and the Schottky barrier gate FET (MESFET) [17] were studied under reverse bias. The reverse gate voltage controls the depletion thickness at the junction and thus modulates the

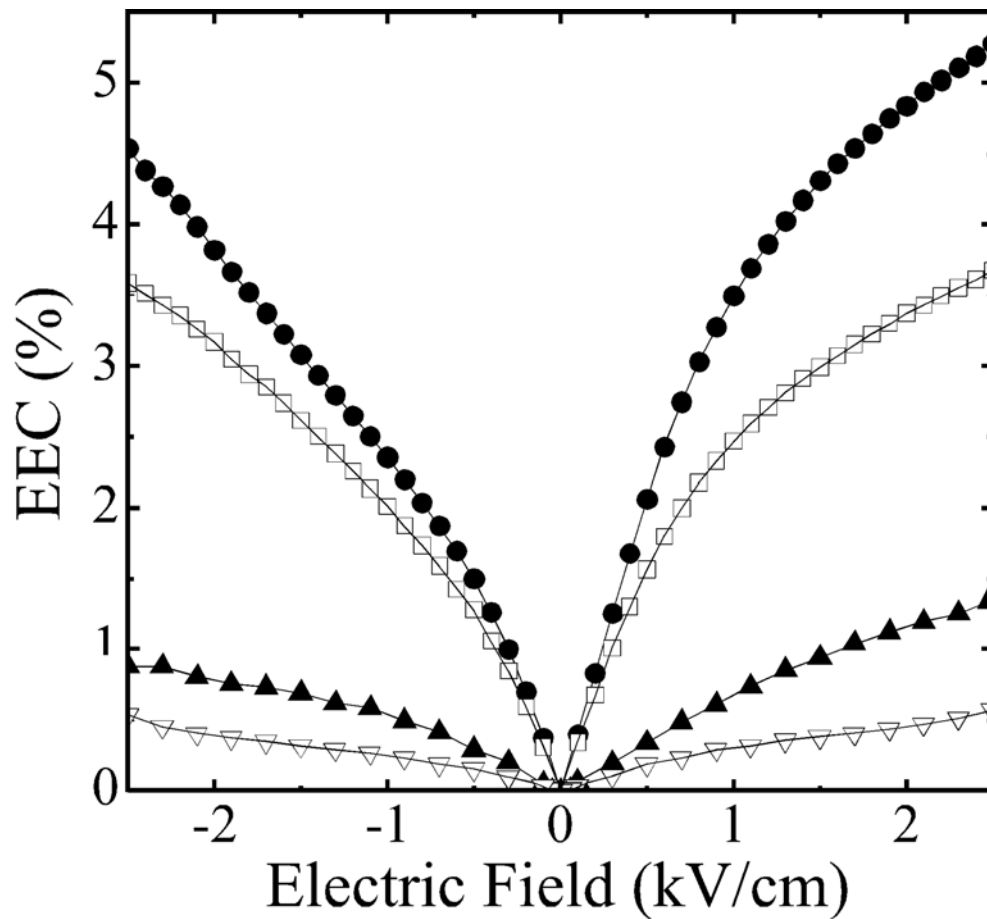


Figure. 7.3. The geometry dependence of the EEC effect. The symbols correspond to  $16\alpha = 1, \bullet; 5, \square; 10, \blacktriangle; 14, \nabla$ . The mesa radius for each device is  $100\mu\text{m}$ .

conductivity of the electron channel. EEC distinguishes itself from the FET like devices by the forward field effect. Without a proper modification of the FET structure, the forward bias cannot be studied due to the additional current injection from metal to semiconductor, which is inseparable from the pure field effect. In the EEC structure, a 1 $\mu\text{m}$  thick  $\text{Si}_3\text{N}_4$  dielectric thin film is included between the top electrode and the metal shunt for this purpose. At equilibrium, the estimated depletion width is given by [18],

$$W = \sqrt{\frac{2\varepsilon_s}{qn} \left( V_{in} - V_B - \frac{kT}{q} \right)} \quad (2)$$

where  $\varepsilon_s$  is the permittivity,  $V_{in}$  is the built-in voltage, and the other parameters have their usual meanings. This yields  $W = 31.5$  nm for our devices with  $V_{in} = 0.3$  V. Under a forward field, the depletion is thinned and more thermally excited electrons can tunnel through the barrier near the top from semiconductor to metal. The Ti and Au/Ge thin films act as both a Schottky gate and a current shunt. By providing an alternative route for electrons traveling from semiconductor to metal, current paths are not restricted to the conducting channels shaped by the depletion as in FET devices. This contributes significantly to the geometry dependence of the EEC effect.

On the other hand, under zero applied electric field and direct reverse bias across leads 5 and 4, a configuration we label as the FET testing mode, the EEC sensor behaves as a JFET. In an analytical model we developed, a GaAs annulus, with the central hole corresponding to the depletion region, and a homogenous GaAs cylinder are connected in parallel. The inset of the Fig. 7.4 shows the 3D schematics of the 2-layer model. The total resistance can be expressed as,

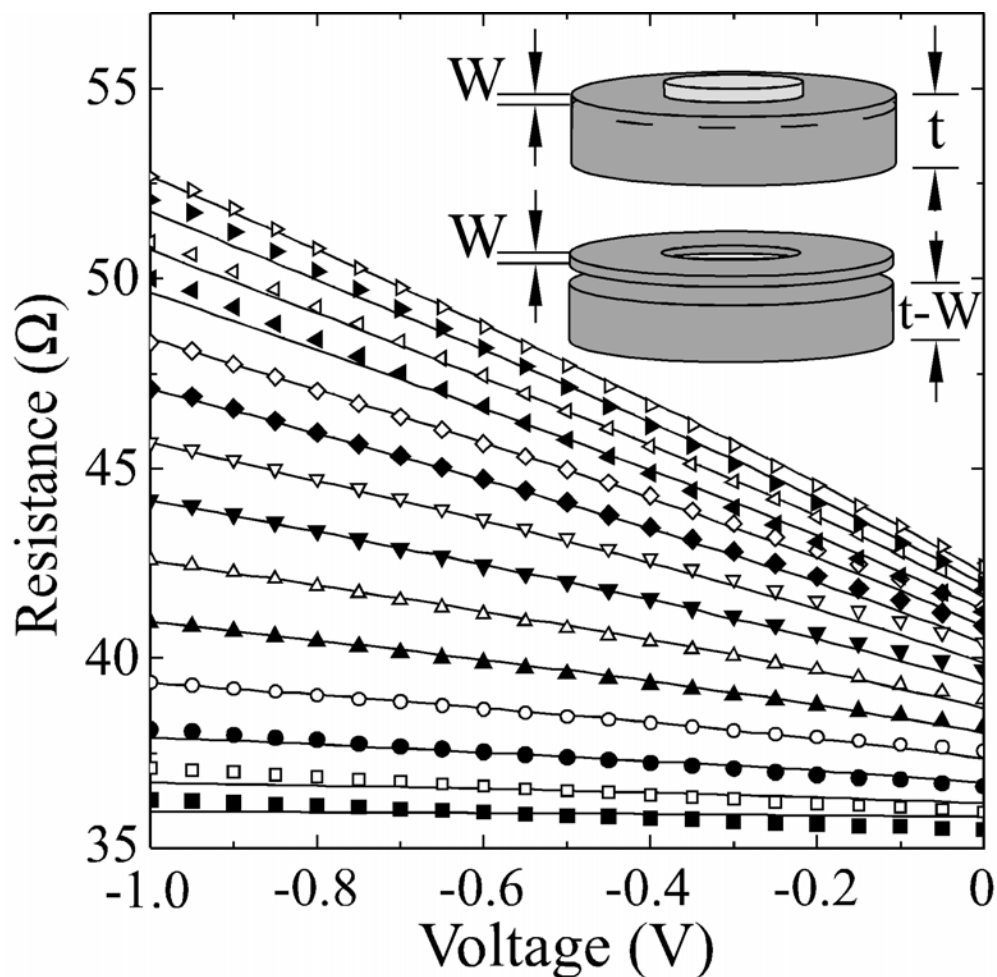


Figure. 7.4. Inset – Schematics of the 2-layer EEC structure under reverse bias. Main panel – The solid lines are fits of Eq. (7.3) to experiment for samples with  $R = 60 \mu\text{m}$  under reverse bias. The symbols correspond to the observed resistances adjusted by  $R_c(\alpha)$  with  $[16\alpha, R_c(\alpha)] = (1, 10.92 \Omega), \blacksquare; (2, 20.45 \Omega), \square; (3, 12.69 \Omega), \bullet; (4, 6.09 \Omega), \circ; (5, 11.23 \Omega), \blacktriangle; (6, 13.63 \Omega), \triangle; (7, 12.02 \Omega), \blacktriangledown; (8, 9.39 \Omega), \triangledown; (9, 7.81 \Omega), \bullet; (10, 6.91 \Omega), \blacklozenge; (11, 13.22 \Omega), \blacktriangleleft; (12, 9.16 \Omega), \triangleleft; (13, 10.97 \Omega), \blacktriangleright; (14, 13.39 \Omega), \triangleright$ .

$$\frac{1}{R(\alpha, V_B)} = \frac{1}{R_{Top}(\alpha, V_B)} + \frac{1}{R_{Bottom}(\alpha, V_B)} \quad (7.3)$$

where  $R_{Top} = \frac{1}{\pi\sigma W} \sum_{n=1}^{\infty} \left[ \frac{2(1+\alpha^{2n})}{(1-\alpha^{2n})} - \frac{(1+\alpha^{4n})}{(1-\alpha^{4n})} \right] \frac{1}{n} (-1)^{n+1}$  [19; 20], and, with  $\alpha = 0$ ,

$$R_{Bottom} = \frac{\ln 2}{\pi\sigma(t-W)}. \quad \text{The model assumes sidewall contacting of the voltage and current}$$

probes whereas the devices use surface contacts. This necessitates the introduction of one adjustable offset parameter  $R_C(\alpha)$ , so that the calculated effective resistance is

$$R_{eff}(\alpha, V_B) = R(\alpha, V_B) + R_C(\alpha) \quad (7.4)$$

For clarity of presentation, the main panel of Fig. 7.4 compares  $R(\alpha, V_B)$  (solid lines) and  $[R_{obs} - R_C(\alpha)]$  (symbols), where  $R_{obs}(\alpha, V_B) = V_{23}/I_{14}$ . The model provides a very good fit to the data for various values of  $V_B$  and  $\alpha$ . The values of  $R_C(\alpha)$  are given in the figure caption. Further details of the model will be discussed elsewhere [14].

Under the FET testing mode, the key difference between EEC and JFET/MESFET comes from the device geometry. In both JFET and MESFET, the gate has a fixed dimension and covers the major area of the conducting channel. However, in the case of EEC, the Ti shunt, equivalent to the gate in the FETs, has a variable area and the ratio  $\alpha$  ranges from 1/16 to 14/16. With 20  $\mu\text{A}$  alternating current from leads 1 to 4, the device operates in the linear regime. Due to the special structure of EEC devices, there is no pinch off effect [16]. Under reverse bias, the radius of the depletion region in the semiconductor coincides with that of the shunt. Suppose enough bias is applied and the semiconductor thin film under the shunt is totally depleted, electrons can still travel in

the annulus shaped semiconductor surrounding the depletion. Under the above conditions, the geometry dependence of the resistance in a FET like device can now be demonstrated in terms of the “gate” sizes.

## **7.6 Conclusion**

In summary, we have demonstrated the proof of principle of EEC in GaAs-Ti thin film MSH. The geometry dependence of the device resistance and the dual role of the Schottky metal, i.e. gate in the FET testing mode and current shunt in direct field sensing, distinguish EEC from the JFET and MESFET structures. The inclusion of the dielectric layer of  $\text{Si}_3\text{N}_4$  makes the forward bias study of a Schottky interface possible. An individual EEC device could function as an electric field sensor. Arrays of such sensors could be used for biological applications. For example, by scaling to the nano regime, an EEC sensor array could, in principle, produce a real time image of the charge distribution on a single cell surface.

## **7.7 Acknowledgements**

We thank L. R. Ram-Mohan for useful discussions. This work is supported by the US NIH under grant 1U54CA11934201 and by the US NSF under grant ECCS-0725538. SAS is a co-founder of and has a financial interest in PixelEXX, Inc. a start-up company whose mission is to market EXX imaging arrays.



## **Bibliography**

- [1] R. S. Popovic, “Hall effect devices”, Adam Hilger, Bristol (1991).
- [2] S. A. Solin, D. R. Hines, T. Thio and J. Heremans, *Science* **289**, 1530 (2000).  
S.A. Solin, D. R. Hines, J.S. Tsai, Yu. A. Pashkin, S. J. Chung, N. Goel and M. B. Santos, *Appl. Phys. Lett.* **80**, 4012 (2002).
- [3] C. H. Rowe, D. R. Hines and S. A. Solin, *Appl. Phys. Lett.* **83**, 1160 (2003).
- [4] C. H. Rowe and S. A. Solin, *Phys. Rev. B* **71**, 235323 (2005).  
K. A. Wieland, Yun Wang, L. R. Ram-Mohan, S. A. Solin and A. M. Girgis, *Appl. Phys. Lett.* **88**, 052105 (2006).
- [5] K.A. Wieland, Yun Wang, S. A. Solin, A. M. Girgis, and L. R. Ram-Mohan, *Phys. Rev. B* **73**, 155305 (2006).
- [6] S. Dushman, *Rev. Mod. Phys.* **2**, 381 (1930).
- [7] W. Shockley and W. T. Read, *Phys. Rev.* **87**, 835 (1952).
- [8] S. Chand and J. Kumar, *Semicond. Sci. Technol.* **12**, 899 (1997).
- [9] K. Maeda, H. Ikoma, K. Sato, and T. Ishida, *Appl. Phys. Lett.* **62**, 2560 (1993).
- [10] S. M. Sze, C. R. Crowell, and d. Kahng, *J. Appl. Phys.* **35**, 2534 (1964).
- [11] J. A. Ellis and P. A. Barnes, *Appl. Phys. Lett.* **76**, 124 (2000).
- [12] K. M. Newaz, Yun Wang, Jian Wu, S.A. Solin, V.R. Kavasseri, I.S. Ahmed, and I. Adesida, to be published.
- [13] R. B. Pierret, “Semiconductor Device Fundamentals”, 200 (1996).
- [14] W. Shockley, *Proc. IRE.* **40** 1365 (1952).
- [15] A. Mead, *Proc. IEEE.* **54** 307 (1966).

- [16] S. M. Sze, “Physics of Semiconductor Devices”, 2<sup>nd</sup> edition, 248 (1981).
- [17] T. Zhou, S. A. Solin, and D. R. Hines, J. Magn. Magn. Mater. **226**, 1976 (2001).
- [18] Wolfe, G. Stillman, and J. A. Rossi, Sol. St. Sci. and Tech. **199**, 2 (1972).

# **Chapter 8**

## **Transport measurements and analytical modeling of extraordinary electroconductance in Ti-GaAs metal-semiconductor hybrid structures**

### **8.1 Abstract**

We present a comprehensive study of a new phenomenon, extraordinary electroconductance (EEC), in microscopic metal-semiconductor hybrid structures

(MSH) at room temperature. Our artificially designed MSH structure shows highly efficient external electric field sensing properties not exhibited by bare semiconductor structures. The microscopic device is fabricated from a GaAs epitaxial layer with a Ti/Au shunt subject to an external electric field and gives a maximum 5.2% EEC effect corresponding to a change of electric field of the order of 3 V/cm. Moreover, the study reveals a strong dependence of the transport properties on the geometry of the MSH. An analytical 2-layer model is developed which provides good agreement with the experimentally observed data. We propose that scaled down nanoscopic EEC sensor arrays can be used as a novel imaging technique for the charge distribution on a single cell surface in real time.

## 8.2 Introduction

The electrical transport properties of any device depend on two factors, one physical and one geometric. The contribution to the physical components arises from the material properties such as doping level, impurities, bulk mobility, etc. On the other hand, the contribution to the geometric components comes from the configuration of the device such as the device dimensions, shape, lead contact area, lead arrangement, etc.[1] Traditionally, semiconductor device studies focused on the physical contributions and limited the geometrical effects on purpose to fully examine the underlying physics. But by careful design, the geometric contribution can be made dominant in the transport properties. The recently discovered extraordinary magnetoresistance (EMR) in a metal-semiconductor hybrid (MSH) structure by Solin *et. al.* [2] is the first example of

geometry driven effects. What Solin and his coworker pointed out in the study is that the physical effects can be enhanced by geometric factors such as device shape, dimensions and arrangements of the conducting leads. In fact, a symmetric Van der Pauw (VdP) disk of homogeneous nonmagnetic InSb with an embedded concentric Au inhomogeneity exhibits a 100% magnetoresistance (MR) effect at the field of 0.05T at room temperature, exceeding the spin dependent GMR effects [7,8] and colossal MR [9]. Geometry dependent properties, other than electronic transport, in different nanoscopic and mesoscopic devices have also been reported [3-6].

The EMR devices have a donut shaped InSb VdP structure with a Au filling at the center. The ohmic metal-semiconductor (MS) interface and the Corbino-like structure play central roles in the magnetoresistance. At zero magnetic field, the electron takes the easiest route through the metal, i.e., small effective resistance. On the other hand, at nonzero magnetic field, the Lorentz force due to the magnetic field deflects the current through the semiconductor, i.e., high effective resistance. This difference in resistance with and without the magnetic field is the origin of the geometry dependent EMR. By extending this general idea of geometrically driven interfacial effects on transport properties, a new class of EXX phenomena has been demonstrated, where E= extraordinary and, to date, XX = magnetoresistance (MR) [10], piezoconductance (PC) [11,12], and optoconductance (OC) [13,14].

Following the discovery of EMR, EPC and EOC, it was realized that an electric field equivalent of the EXX phenomenon, i.e., extraordinary electroconductance (EEC), should exist, with the external electric field providing the perturbation. In principle, the EEC device should have a geometry where the external electric field redistributes the current

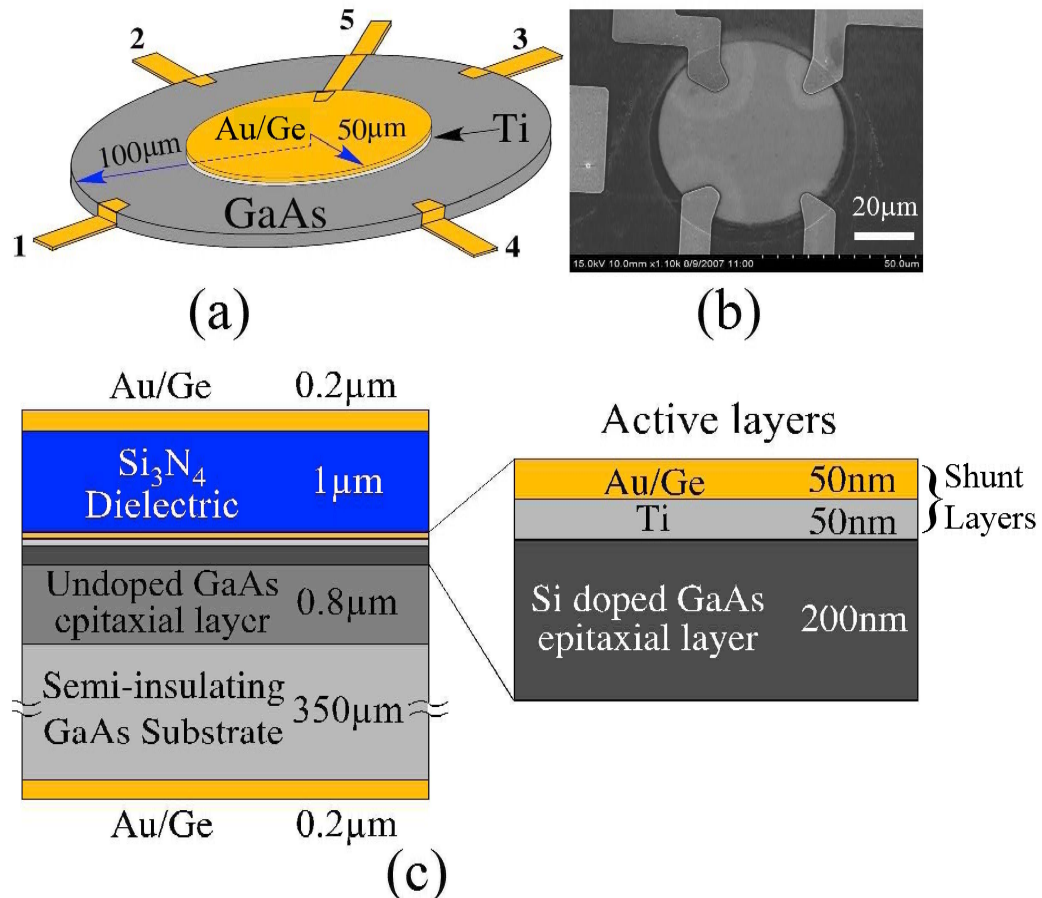


Figure. 8.1 Panel (a) A 3D schematic of the EEC Van der Pauw structure. A concentric metal shunt of radius  $50 \mu\text{m}$  is in a direct contact with the GaAs mesa of radius  $100 \mu\text{m}$ . Four leads are deposited on the periphery of the mesa surface and lead 5 is directly connected to the shunt. Panel (b) An SEM image of an EEC device without the shunt metal on top. Panel (c) A cross sectional view of the EEC multilayer structure. The shunt is composed of two  $50 \text{ nm}$  thick metal thin films, Ti and Au/Ge. A pair of parallel plates, as shown in Fig. 8.1(c), is incorporated to apply an external field with a  $1 \mu\text{m}$   $\text{Si}_3\text{N}_4$  dielectric between the top plate and the shunt.

propagation. In EMR and EOC devices, the interface between metal and semiconductor is ohmic. Since the external electric field has very minimal or no impact on an ohmic interface and strong effects on a Schottky MS interface, we have chosen a metal (in this case, Ti) to form a Schottky barrier at the interface. The MSH structure designed for an EEC device is shown schematically in Fig. 8.1(a). The Ti metal disk on top of the cylindrical GaAs mesa forms a Schottky barrier. The external electric field perpendicular to the MS interface modifies the Schottky barrier height and width, which in turn changes the current distribution through the semiconductor, i.e., changing the total resistance. This unique characteristic of the MSH design can be used in sensing efficiently the local electric field intensity. We have recently provided a proof of principle demonstration of the EEC effect in Ti-GaAs MSH structures in a brief preliminary report.<sup>15</sup> Here we provide the detailed experimental study of this effect and show a two-layer analytical model that quantitatively accounts for the observed transport properties under an extended range of reverse biases. We have also included a full characterization of the Schottky properties at the Ti/Au-GaAs interface.

This paper is organized as follows. In Sec. 8.2, we provide a detailed description of the experiment setup such as the sample preparation and the instrumentation. Then we discuss the experimental observation of different transport properties, such as the Schottky  $I$ - $V$ , 4-lead conductance change under electric field, device sensitivity and resistance change under reverse shunt bias, in Sec. 8.3. A refined 2 layer analytical model developed to explain the observed transport properties is presented in Sec 8.4. We compare existing field effect devices such as JFETs and MESFETs with our EEC devices in Sec. 8.5. We end the paper with conclusions in Sec. 8.6.

## 8.3 Experimental Procedure

### 8.3.1 Sample design and fabrication

Our EEC devices were prepared using lattice-matched GaAs epitaxial layers, as shown in Fig.8.1(c), grown by molecular beam epitaxy (MBE). The active layer of the device is a 200 nm thick Si-doped GaAs epitaxial layer (mobility  $\mu = 4400 \text{ cm}^2\text{V}^{-1}\text{S}^{-1}$ , carrier concentration  $N_D = 4 \times 10^{17} \text{ cm}^{-3}$ ), followed by an undoped 800 nm thick epitaxially grown GaAs layer as a buffer with a semi-insulating GaAs substrate (thickness  $t = 350\text{mm}$ ) at the bottom. The mesa was first fabricated using standard optical lithography and wet etching. Second, AuGe/Ni/Au metal layers for the ohmic leads were deposited followed by a thermal annealing at  $450^\circ\text{C}$  for 1 minute. The four contacting pads of the leads are symmetrically distributed around the periphery of the mesa disk and ohmic contacting to the surface is achieved. Next, we have deposited concentric double metal layers composed of a 50 nm thick Ti thin film, which has an intimate contact to the GaAs epi layer to form a Schottky interface, and a 50 nm thick Au/Ge thin film, which acts as an effective shunt for electron transport. Ti and Au metals were deposited sequentially in a metal evaporation system. Before depositing metal for the ohmic leads and the shunt, we have etched the surface oxidation by dipping the sample in an HCl:DI (1:2) solution for 5 minutes and quickly transferring the sample to the evaporation system. An additional bonding lead is attached to this shunt metal for biasing purposes.

Fig. 8.1(a) shows schematically the 3D structure of a typical EEC device. An SEM image of a defined mesa connected with four ohmic leads is shown in Fig. 8.1(b). To test



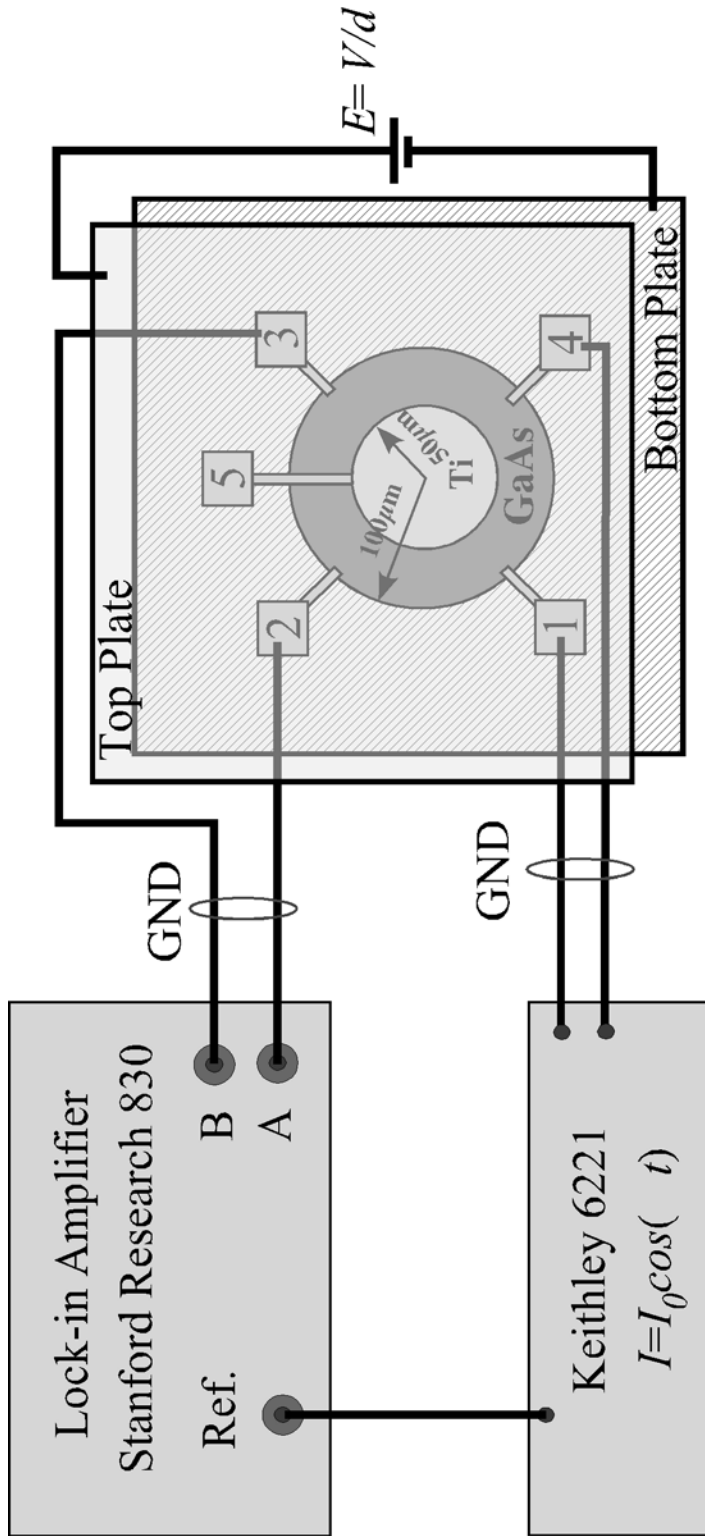


Figure 8.2 A schematic diagram of the experimental setup for measuring the four-point resistance using the lock-in method. The EEC device is inside a parallel plate capacitor configuration and the electric field ( $E = V/d$ , where  $d$  is the separation between the top and the bottom plates) is directly proportional to the voltage applied across.

our device under an external electric field, a pair of capacitor plates is incorporated into the EEC structure. In order to prevent leakage current from the top metal plate to the Au/Ge shunt, a  $1\mu\text{m}$  thick layer of  $\text{Si}_3\text{N}_4$  is sandwiched in between. The  $\text{Si}_3\text{N}_4$  insulating dielectric was deposited by plasma enhanced chemical vapor deposition (PECVD) and etched with a plasma etcher. A schematic cross-sectional view of the heterostructure is shown in Fig. 8.1(c). Finally we have deposited the two metal layers of Au/Ge for the top and bottom capacitor plates, as shown in Fig. 8.2, using optical lithography.

We define a geometrical parameter  $\alpha$  to be ratio of the shunt radius  $r_s$  to the mesa radius  $r_m$ . As in Fig. 8.1(a),  $r_s = 100\ \mu\text{m}$  and  $r_m = 100\ \mu\text{m}$ , i.e.,

$$\alpha = r_s / r_m . \quad (8.1)$$

Two sets of devices with  $r_m = 100\ \mu\text{m}$  and  $60\ \mu\text{m}$  have been studied and each set contains 15 devices with  $\alpha$  from 0/16 (controlled sample) to 14/16.

### 8.3.2 Experimental setup

Before testing the EEC effect, the property of the Schottky interface needs to be characterized. The four ohmic leads are numbered from 1 to 4 clockwise and the lead to the shunt is numbered as 5 as shown in the Fig. 8.1(a). By attaching the shunt lead 5 and ground lead 4 to a current source (Keithley 6221) and a nano voltmeter (Keithley 2182) in parallel, the I-V characteristics can be obtained.

With the  $\text{Si}_3\text{N}_4$  dielectric between the top capacitor plate and the shunt metal, the resistance is found to be  $\sim 10^{12}\ \Omega$ , which assures negligible current leakage through the MS interface in the device.

The EEC device contains a Van der Pauw [16] mesa structure. The resistance of the device was measured in a four-probe setup to eliminate any influence of the contact resistance between the metal leads and semiconductor. In addition, we adopted both the delta method [17] and lock-in method [18] to measure the resistance to exclude low frequency ( $f < 100\text{Hz}$ ) thermal noise. In the delta method, a Keithley 6221 provides a square wave current with amplitude of  $20\ \mu\text{A}$  at a frequency of  $0.2\text{kHz}$ . A Keithley 2182 performs A/D conversion at source high and source low points. A three-point moving-average algorithm is used to calculate the 4-lead resistance. In the lock-in method, as shown schematically in Fig. 8.2, the square current is replaced by a sinusoidal wave at the frequency of  $7\ \text{kHz}$  and the data were sampled uniformly along the oscillation. As both methods produce equivalent results, we chose the Lock-in method due to its faster data acquisition. The external electric field is realized by applying a DC voltage across the top and bottom capacitor plates built into the device. All the measurements were carried out at room temperature. The EEC device and electrical feedthroughs were enclosed in a grounded metal box to isolate the measurement from the external noise or disturbance.

## 8.4 Experimental Observations

### 8.4.1 Schottky I-V

The main panel of Fig. 8.3 shows the Schottky rectification property originating from the Ti-GaAs MS interface. Here the Schottky  $I$ - $V$  characteristic is measured between the

terminals 5 and 4 as shown in Fig. 8.1(a). Ti adheres well to GaAs and the Ti-GaAs interface forms an excellent Schottky barrier [19]. We have measured the Schottky I-V curve for 60 devices and all showed similar characteristics to those presented in Fig. 8.3. In the reverse bias region ( $V < 0$ ), the current is essentially zero before breaking down, while in the forward bias region ( $V > 0$ ), the current increases sharply after a threshold voltage  $V_T$ , where  $V_T \sim 0.3\text{V}$ .

For a metal-semiconductor system with a moderately doped semiconductor ( $5 \times 10^{16} \text{ cm}^{-3} \leq n \leq 5 \times 10^{17} \text{ cm}^{-3}$ ), as in the EEC devices, the tunneling of thermally excited electrons or thermionic field emission (TFE) dominates the electron transport. The total current can be expressed as [20],

$$I = I_s \exp(qV/nkT - 1), \quad (8.2)$$

where  $q$  is the electron charge and  $I_s$  is the saturation current, a complicated function of the MS interfacial area, barrier height, properties of the semiconductor and the operation temperature. It can be obtained by extrapolating the current from the linear extension of  $\ln I - V$  at  $V = 0$ . Here  $n$  is the so-called ideal factor and is defined as,

$$n \equiv \frac{q}{kT} \frac{\partial V}{\partial(\ln I)}. \quad (8.3)$$

where  $J$  is the current density. The deviation of a real Schottky interface from the ideal ( $n = 1$ ) can be attributed to many effects, such as electron trapping and recombination [21], barrier inhomogeneities [22], an interfacial oxide layer [23], image force lowering [24], shunt resistance [25] and series resistance [26]. In the two-terminal Schottky I-V measurement, comparing to an ideal Schottky diode, the EEC device has a built-in series resistance. When a current is sent from the leads 5 to 4, it passes through the Schottky

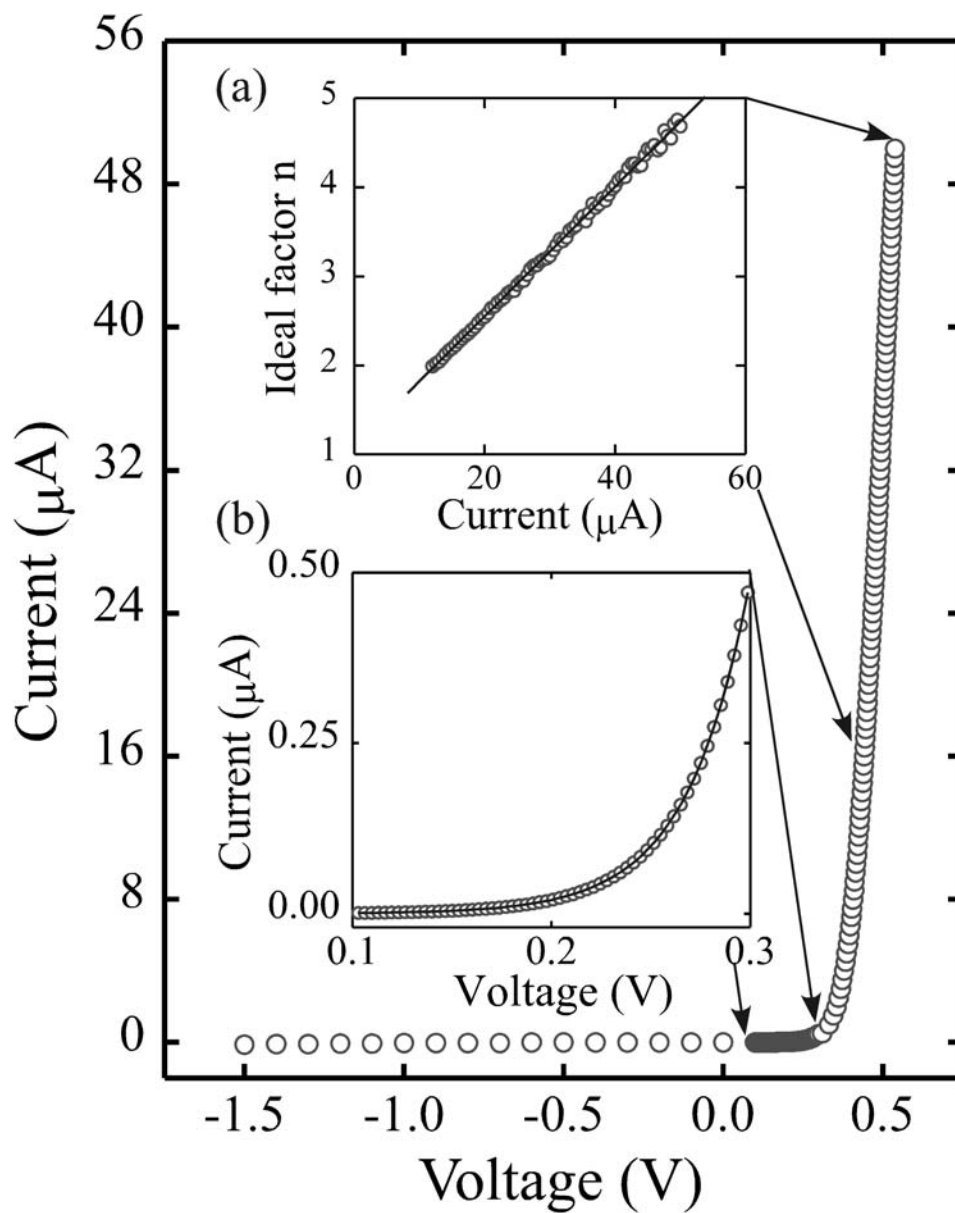


Figure. 8.3 Main panel - The room temperature I-V characteristic of the Schottky interface. The inset (a) shows the linear dependence between the ideal factor  $n$  and the current for  $I > 16 \mu\text{A}$ . The inset (b) shows the quasi-exponential dependence between the current and

interface as well as the annular shaped GaAs uncovered by metal, which leads to a series resistance. When the current is in the high forward bias regime, i.e.,  $I > 16 \mu\text{A}$ , the term “-1” in Eq. (8.2) is negligible. To incorporate the effect of the series resistance, Eq. (8.2) can be modified as

$$I = I_s \left\{ \exp \left[ \frac{(qV - IR_{se})}{n_0 kT} \right] \right\} \quad (8.4)$$

where  $R_{se}$  is the series resistance and  $n_0$  is the modified ideal factor of the diode excluding the effect from  $R_{se}$ . By taking the natural log of Eq. 8.4, differentiating both sides by  $d/d \ln I$  and plugging in Eq. 8.3, we have

$$n = n_0 + (qR_{se}/kT) \cdot I. \quad (8.5)$$

Thus the series resistance leads to a linear dependence between the ideal factor  $n$  and the current  $I$  in the high forward bias regime, which is shown in inset (a) of Fig. 8.3. From the intercept and the slope,  $n_0 = 1.142$  and  $R_{se} = 1818 \Omega$  can be obtained, respectively. In fact,  $R_{se}$  can be estimated from a simple approximation, where the current from leads 5 to 4 is assumed to be highly concentrated in a rectangular shaped channel within the uncovered region of the GaAs mesa. The channel length is  $(r_m - r_s)$  and the width is the same as the contact pads, i.e.,  $4 \mu\text{m}$ , while the channel height equals to the mesa thickness, i.e.,  $200 \text{ nm}$ . The resistivity of the GaAs can be calculated from the carrier mobility and concentration. The result is  $\sim 1400 \Omega$ . As both numbers are in the same order of magnitude, the above two calculations are self-consistent. In addition, if we directly fit  $\ln I - V$  from Eq. 8.2 with a straight line,  $n \sim 1.31$ . As  $n_0$  is much closer to 1 than  $n$ , this confirms the notion that  $R_{se}$  induces non-ideal properties to the EEC Schottky interface.

At a low forward bias  $0 < I < 0.5 \mu\text{A}$ , the effect from  $R_{se}$  is minimal as  $I \cdot R_{se} \ll V$  and the shunt effect becomes important. The current starts to bypass the Schottky barrier through a shunt resistance,  $R_{sh}$ , and Eq. 8.2 is further modified as

$$I = I_s \left[ \exp(qV/n'_0 kT) - 1 \right] + V/R_{sh}. \quad (8.6)$$

Here to distinguish from  $n_0$ ,  $n'_0$  is used as the modified ideal factor excluding the shunt effect. In the low current bias regime  $0 < I < 0.5 \mu\text{A}$ , an exponential-linear combination function  $y = p_1 \exp(-x/p_2) + p_3 + p_4 x$  fits the data perfectly. The two parameters in Eq. 8.6,  $R_{sh} = 3.45 \times 10^8 \Omega$  and  $n'_0 = 1.197$ , can be extracted from the fitting parameters  $p_4$  and  $p_2$  respectively. Inset (b) of Fig. 8.3 shows the quasi-exponential  $I$ - $V$  dependence in this region. The characterization of the shunt resistance in an EEC device is crucial to the understanding of the electron transport property under an electric field. In addition to the Schottky barrier, the shunt resistance provides another path for electrons from the GaAs mesa to get access to the Ti/Au shunt and results in a redistribution of the current between the metal and the semiconductor. This current redistribution gives rise to a measurable device conductance change.

### 8.4.2 EEC 4-lead Resistance under Direct Bias

We measure the device resistance by sending a current through leads 1 to 4,  $I_{14}$ , and measuring the voltage drop across leads 2 and 3,  $V_{23}$ . The observed resistance  $R_{obs}$  is given by,

$$R_{obs}(\alpha, E) = \frac{1}{G(\alpha, E)} = \frac{V_{23}}{I_{14}}, \quad (8.7)$$

where  $G(\alpha, E)$  is the sample conductance. Using an electric field, we can externally perturb the EEC device in two different ways. First, applying a bias voltage across the shunt lead 5 and the ground lead 4, which we label as direct biasing. The non-linear current voltage dependence and the non-uniform field distribution at the MS interface make it very complicated to calculate the local field intensity. Second, applying a bias voltage across the capacitor's top and bottom plates, which we label as indirect biasing. The field intensity in this case is simply given by  $E = V/d$ , where  $d$  ( $\sim 400 \mu\text{m}$  for the EEC devices studied here) is the separation between the top and bottom plates. Under a direct bias, the EEC device operates as a Field Effect Transistor (FET). The direct bias voltage ranges from -2V to +1V, as shown in Fig. 8.4. In the reverse bias region, sample resistance declines linearly as the bias increases (i.e., the magnitude of bias voltage decreases), and this linear dependence continues into the forward region until  $V \sim V_T$ , followed by a dramatic drop in the device resistance.

The rapid decrease in resistance in the forward bias region arises from current injection. When a metal and an  $n$ -type semiconductor have an intimate contact, electrons from semiconductor conduction band will keep flowing into the metal until the Fermi levels on the two sides line up. Positive ionized donors are left behind in the semiconductor while electrons that surmount or tunnel through the barrier form a thin sheet of negative charges on the metal surface. An internal electric field from semiconductor to metal is built up. As electrons move out of the semiconductor into the metal, the free electron concentration near the boundary decreases and a high-resistivity



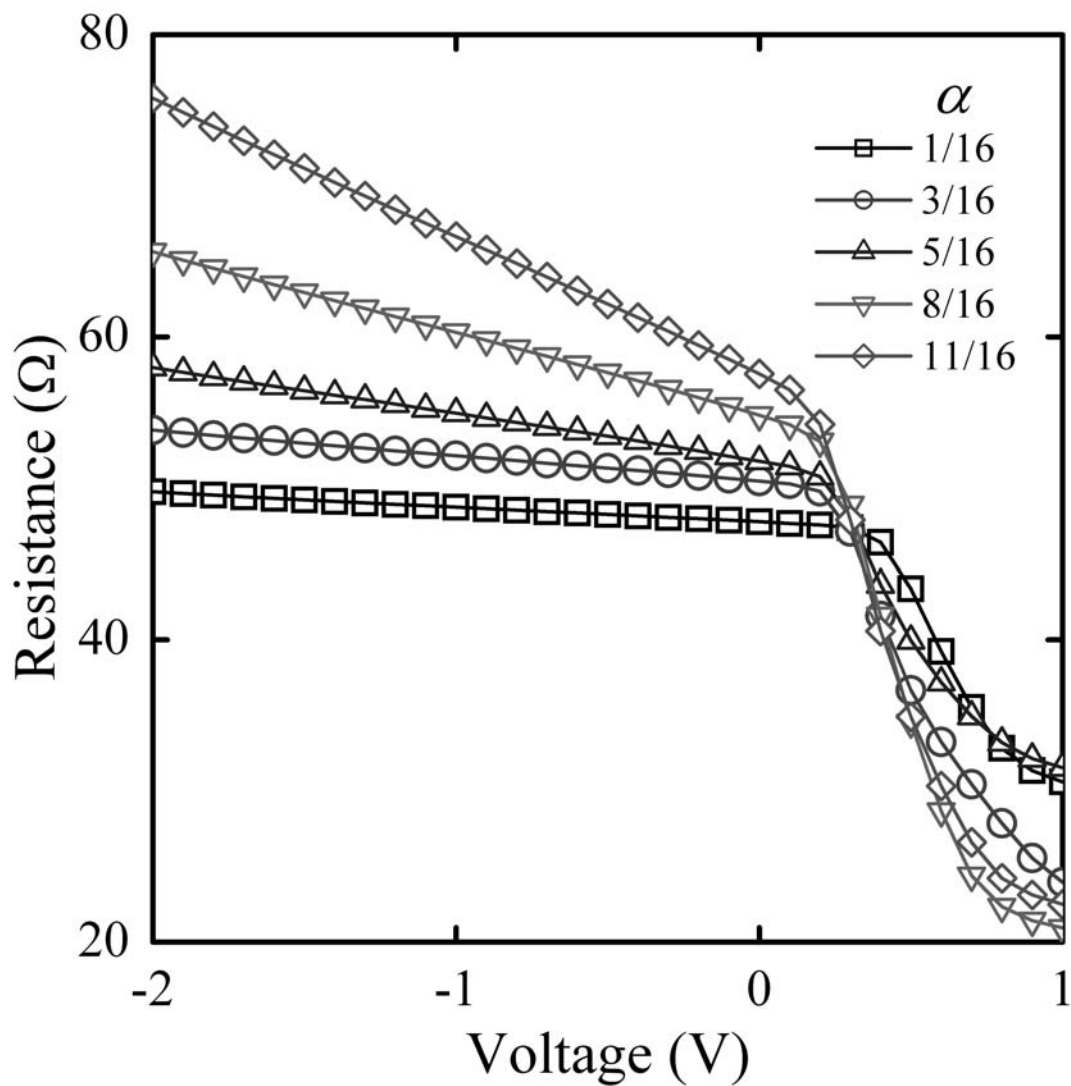


Figure. 8.4 The four lead resistance of devices with 60  $\mu\text{m}$  mesa radius and different  $\alpha$  values under a direct shunt bias voltage from -2 V to +1 V.

depletion region is formed. The depletion width  $W$  depends on the square root of the applied bias voltage [27]. When a forward bias is applied, the resultant electric field at the interface decreases and so does the depletion width. For the devices shown in Fig. 8.4, when  $V$  increases to  $+0.3V$ , the depletion is thin enough for a large number of electrons to tunnel through the barrier leading to a substantial decrease in the measured 4-lead resistance. Therefore, the depletion width at equilibrium,  $W_0$ , can be estimated from this threshold voltage, which will be discussed in Sec. 8.5.1.

### 8.4.3 EEC 4-lead Resistance under External Electric Field and its Field Sensitivity

The EEC devices are essentially field-controlled resistors, which can be used as electric field sensors. To study the response of our devices to an external electric field, a quantity  $EEC$  is defined to be the percentage change in sample conductance with an external electric field and without field and is given by,

$$EEC = \frac{|G(\alpha, E) - G(\alpha, 0)|}{G(\alpha, 0)} \times 100\%, \quad (8.8)$$

where  $\alpha$  is the geometric factor defined in Eq. 8.1 and  $G(\alpha, E)$  is the sample conductance defined in Eq. 8.7.

To test the EEC effect, we connect the top and bottom metal plates to a voltage source (Keithley 230) to supply a static field using a DC voltage. Compared to the internal field at the MS interface, usually between  $10^5$  V/cm and  $10^6$  V/cm, the applied field ( $\sim 10^3$  V/cm) is very small and can be treated as a perturbation. Fig. 8.5 shows the

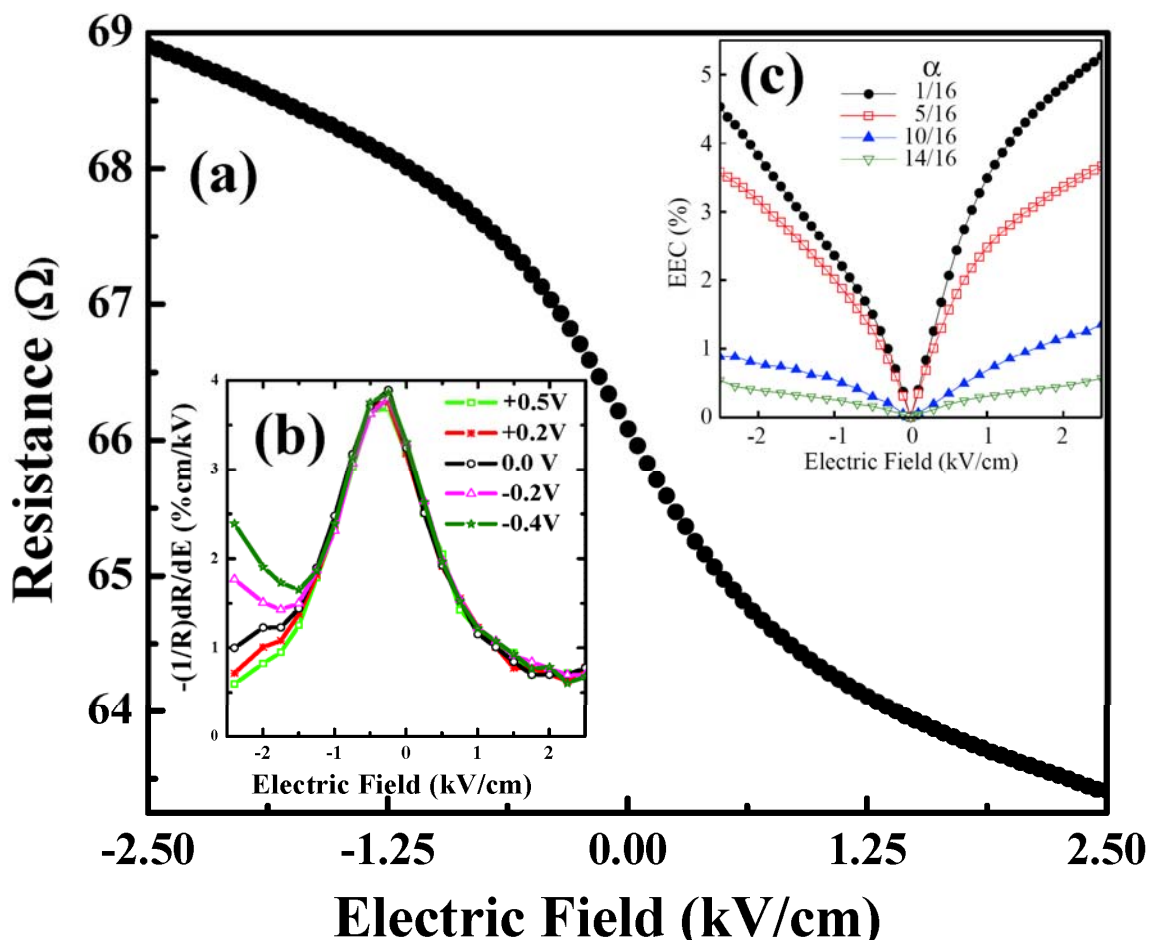


Figure. 8.5 Main panel (a) 4-point resistance of an EEC device measured with respect to an external electric field. Inset (b) shows the device sensitivity at the corresponding shunt biases. Panel (c)-EEC effects in four different devices with  $\alpha = 1/16$ ;  $5/16$ ;  $10/16$ ;  $14/16$ .

field effect of an EEC device under different shunt bias voltages from -0.4V to +0.5V denoted by symbols. For example, as the field increases from -2.5 kV/cm to +2.5 kV/cm, the sample conductance at zero shunt bias increases continuously from 16.97  $\Omega$  to 18.53  $\Omega$ . Thus the measured conductance is a figure of merit for electric field sensing.

We calculate the device sensitivity as the percentage change in sample conductance with respect to the field change, i.e.,  $1/G(dG/dE) \times 100\%$ . The optimum value is found to be independent of the shunt bias  $V_B$  and is an intrinsic property of the device. The inset of Fig. 8.5 shows the sensitivity of an EEC device with  $r_m = 100 \mu\text{m}$  and  $\alpha = 1/16$  under 5 different shunt biases. For  $E > -1 \text{ kV/cm}$ , the sensitivity of the device is independent of  $V_B$ . As a result, shunt lead 5 is optional for the optimized EEC sensors, and its removal will simplify the design and fabrication of EEC nano sensors and arrays by reducing 1/5 of the total pin outs and connecting circuits.

Our EEC devices are fundamentally different from a regular Schottky diode. For EEC devices, the Shunt metal forming the Schottky barrier does not need to be externally connected. On the other hand, a regular Schottky diode is a two terminal device, where the metal and the semiconductor are connected to external terminals.

Using the instrument precision values and the EEC device sensitivity, one can determine the sensor resolution or the smallest detectible field. For a typical 4-lead resistance test, the magnitude of the alternating current is 20  $\mu\text{A}$  with a precision of 1 nA. During the test, the lock-in amplifier provides a reading of 0.8982 mV with an accuracy of 0.1  $\mu\text{V}$ . Since the error propagates as  $|\Delta R/R| = \sqrt{(\Delta I/I)^2 + (\Delta V/V)^2}$ , the field

resolution can be expressed as  $\frac{|\Delta R/R|}{\text{sensitivity}} = 3.05V/cm$  at the sensitivity of 4%, or in other words, the smallest field that this EEC sensor can detect is 3.05V/cm.

Fig. 8.5(c) demonstrates the geometrical dependence of the EEC effect. Under +2.5kV/cm, a maximum 5.2% EEC effect is obtained in a device with  $r_m = 100\mu m$  and  $\alpha = 1/16$ . Comparing the 4 devices presented in Fig. 8.5(c), it is interesting to note that the smaller the geometrical parameter  $\alpha$ , the larger the effect. With the same mesa size, a device with a smaller  $\alpha$  has a smaller interfacial area, yet a larger ratio between the periphery and the area of the metal shunt disk, i.e.,  $2\pi/r_s$ . Along the edge of the metal disk, the local electric field at the MS interface is much larger than the interior due to an accumulation of surface charges. Under a uniform electric field, the region of high surface charge concentration is more sensitive to the applied field than the region of low charge concentration. Therefore, the EEC device with  $\alpha = 1/16$  exhibits the largest percentage change in conductance compared to other devices with larger  $\alpha$ . A 3D finite element simulation of the dynamic interfacial charge distribution is in progress to interpret the geometry dependence of the EEC effect quantitatively.

## 8.5 Analytical Modeling

### 8.5.1 Field Dependence of the Depletion Width

The potential in the semiconductor space charge region of a Schottky system can be described by the Poisson equation,

$$-\frac{d^2V}{dz^2} = \frac{\rho(z)}{\varepsilon_s}, [0 < z < W] \quad (8.9)$$

where  $\varepsilon_s$  is the permittivity of the GaAs,  $W$  is the depletion width and the  $z$  axis is shown in Fig. 8.7(a). For a typical MS system, a uniformly doped semiconductor and an abrupt change in space charge density at the depletion boundary are assumed. The internal electric field strength increases linearly with distance  $(W - z)$  from the depletion boundary and peaks at the MS interface. By solving the Poisson equation under the above boundary conditions, one can show that [27],

$$W = \sqrt{\frac{2\varepsilon_s}{qN_D} \left( V_{in} - V_B - \frac{kT}{q} \right)}, \quad (8.10)$$

where  $V_{in}$  is the built-in potential,  $V_B$  is the applied bias voltage and  $\varepsilon_s$  is the permittivity of the GaAs. At equilibrium or  $V_B = 0V$ , Eq. 8.10 yields  $W_0 = 31.5$  nm for EEC devices with  $V_{in} = 0.3V$ .

## 8.5.2 The 2-layer Model

Under a reverse bias, the depletion region expands and little current can flow across the MS interface. Therefore, the semiconductor is effectively separated from the metal by the depletion layer and can be modeled individually. The 4-lead resistance essentially consists of two GaAs thin film layers connected in parallel, a GaAs annulus of thickness  $W$  and a GaAs cylinder of thickness  $(t - W)$ , as shown in Fig. 8.7(a). The concentric hole on the top layer, with a radius of  $r_s$  and a thickness of  $W$ , corresponds to the depletion region.

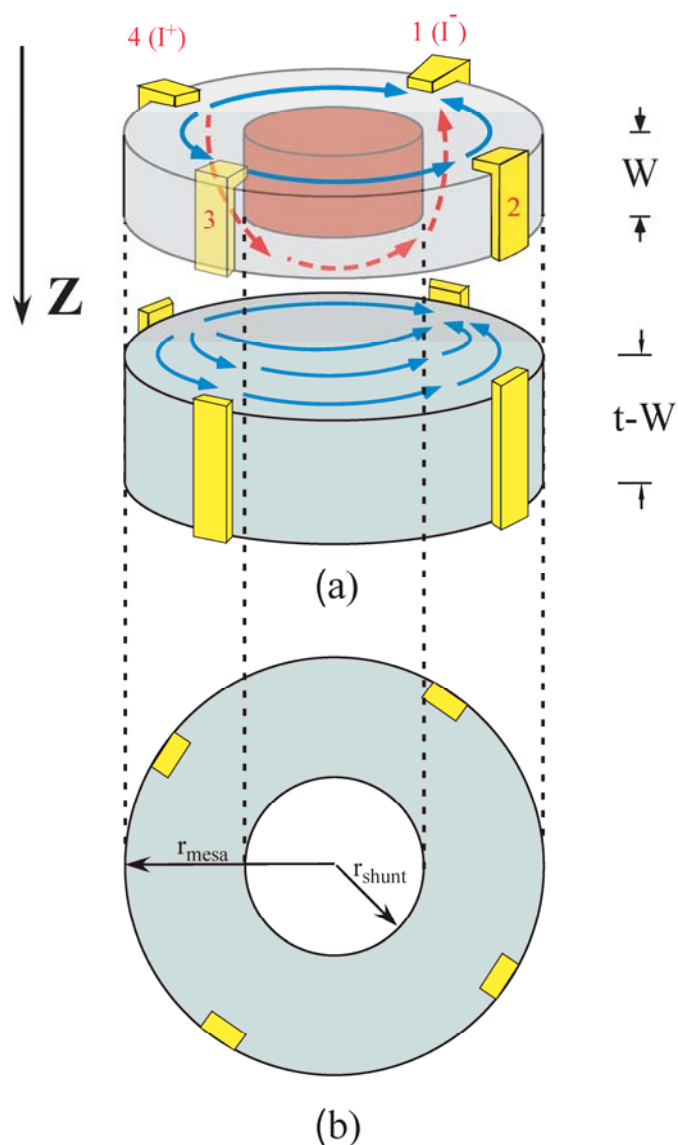


Figure. 8.6 (a) A 3D schematic of the 2 layer structure when the EEC device is under a reverse bias. The red cylinder in the top layer represents the depletion region. The blue arrows in both layers correspond to the in-plane current considered in calculating the resistance of the EEC device. The dashed red arrow in the top layer shows the non-laminar current that flows from the top annulus region to the bottom layer underneath the depletion region. Panel(b) The top view of the upper layer in the 2 layer model. The center inhomogeneity has the same radius as the metal shunt and the same thickness as the depletion width.

The apparent resistivity of a cylindrically symmetric Van der Pauw configuration of radius  $r = a$  with a conducting inhomogeneity of radius  $r = b$  is given by [28, 29]:

$$\rho_{app}(\alpha, \gamma) = \frac{1}{\sigma \ln 2} \sum_{n=1}^{\infty} \left[ \frac{2(1 - \gamma\alpha^{2n})}{1 + \gamma\alpha^{2n}} - \frac{(1 - \gamma\alpha^{4n})}{(1 + \gamma\alpha^{4n})} \right] \frac{1}{p} (-1)^{p+1}, \quad (8.11)$$

where

$$\gamma = \frac{(\sigma_0^2 - \sigma^2)}{(\sigma_0 + \sigma)^2} = \frac{\beta^2 - 1}{(\beta + 1)^2} \quad (8.12)$$

Here  $\alpha = b/a$  and  $\beta = \sigma_0/\sigma$ .  $\sigma$  and  $\sigma_0$  are the conductivity of the medium and the inhomogeneity respectively. In the 2-layer model,  $\alpha$  varies from 1/16 to 14/16 with  $b = r_s$  and  $a = r_m$  according to Eq. 8.1. The parameter represents  $\beta$  the accessibility of the current through the depletion region.  $\beta = 0$  represents a completely depleted inhomogeneity medium, i.e., no current owing through the inhomogeneity medium. On the other hand,  $\beta = 1$  corresponds to no depletion, i.e., the current transport is similar to the semiconductor region. To determine that value of  $\beta$  for our EEC devices, we have compared the experimentally measured 4-point resistance to the values calculated from the 2-layer model for different  $\beta$ s as shown in Fig. 8.7. The excellent agreement of the measured values to the values for  $\beta = 0$  suggests that negligible current is owing through the inhomogeneity region for our EEC devices. Hence we can safely assume that  $\sigma_0 = \sigma$  or  $\gamma \rightarrow -1$ . When  $n$  becomes fairly large,  $\alpha^{2n} \rightarrow 0$  as  $\alpha < 1$ . Thus the augment of the series converges to  $(-1)^{n+1}/n$  and the sum is calculated numerically.



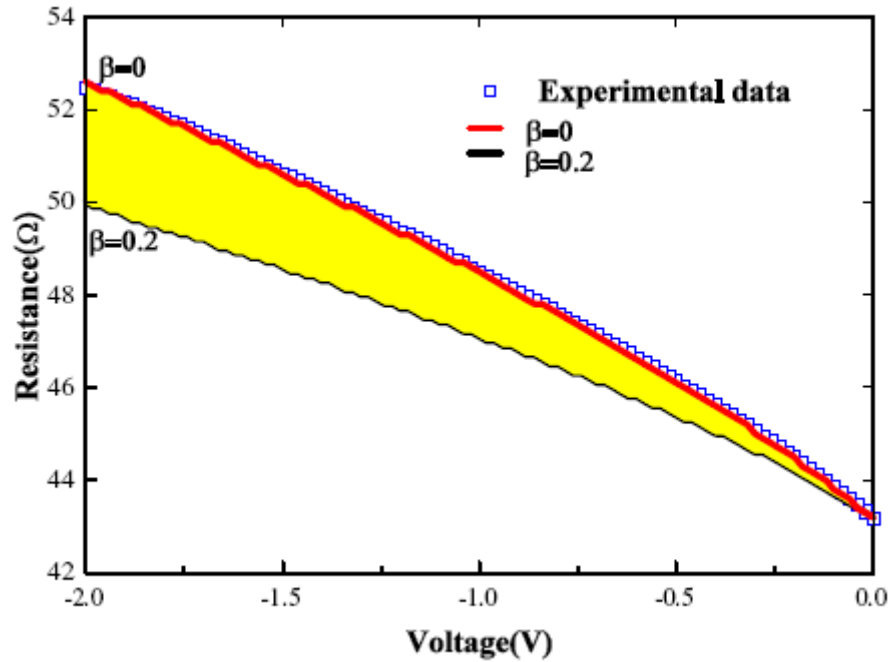


Figure 8.7 The comparison of the curvature between the measured 4-point resistance of the EEC device of  $\alpha = 7/16$  and the values calculated from the 2-layer analytical model for different  $\beta$ s. The shaded area corresponds to the lines for different values of  $\beta$  ranging from 0 (top) to 0.2 (bottom). We have added offset values of  $-12.02 \Omega$  and  $+1 \Omega$  from the measured resistance and  $\beta = 0.2$  lines, respectively, so that the plotted lines converge at the zero voltage ( $V = 0$ ).

For the bottom GaAs cylinder, the apparent resistivity  $\rho_{app}$  is simply the inverse of the medium conductivity ( $1/\sigma$ ), as  $\alpha = 0$  and  $\sum_{n=1}^{\infty} (-1)^{n+1}/n = \ln 2$ . The measured 4-lead resistance and the apparent resistivity are related by the Van der Pauw's expression [16]

$$\rho_{app} = \frac{\pi t}{\ln 2} \frac{V_{23}}{I_{14}}. \quad (8.13)$$

Based on the two-layer model, the total resistance  $R(\alpha, V)$  can be calculated as follows,

$$\frac{1}{R(\alpha, V)} = \frac{1}{R_{Top}(\alpha, V)} + \frac{1}{R_{Bottom}(\alpha, V)}, \quad (8.14)$$

where

$$R_{Top} = \frac{1}{\pi\sigma W} \sum_{n=1}^{\infty} \left[ \frac{2(1+\alpha^{2n})}{(1-\alpha^{2n})} - \frac{(1+\alpha^{4n})}{(1-\alpha^{4n})} \right] \frac{1}{n} (-1)^{n+1}, \quad (8.15)$$

and

$$R_{Bottom} = \frac{\ln 2}{\pi\sigma(t-W)}. \quad (8.16)$$

One interesting implication from Eqs. (8.11) and (8.13) is that the measured resistance does not depend on either the mesa radius or the shunt radius individually, but the radius ratio. If the model properly describes reality, EEC nano sensors with a fixed  $\alpha$  will have the same field sensitivity yet provide a much higher spatial resolution than the microscopic sensors studied in this paper.

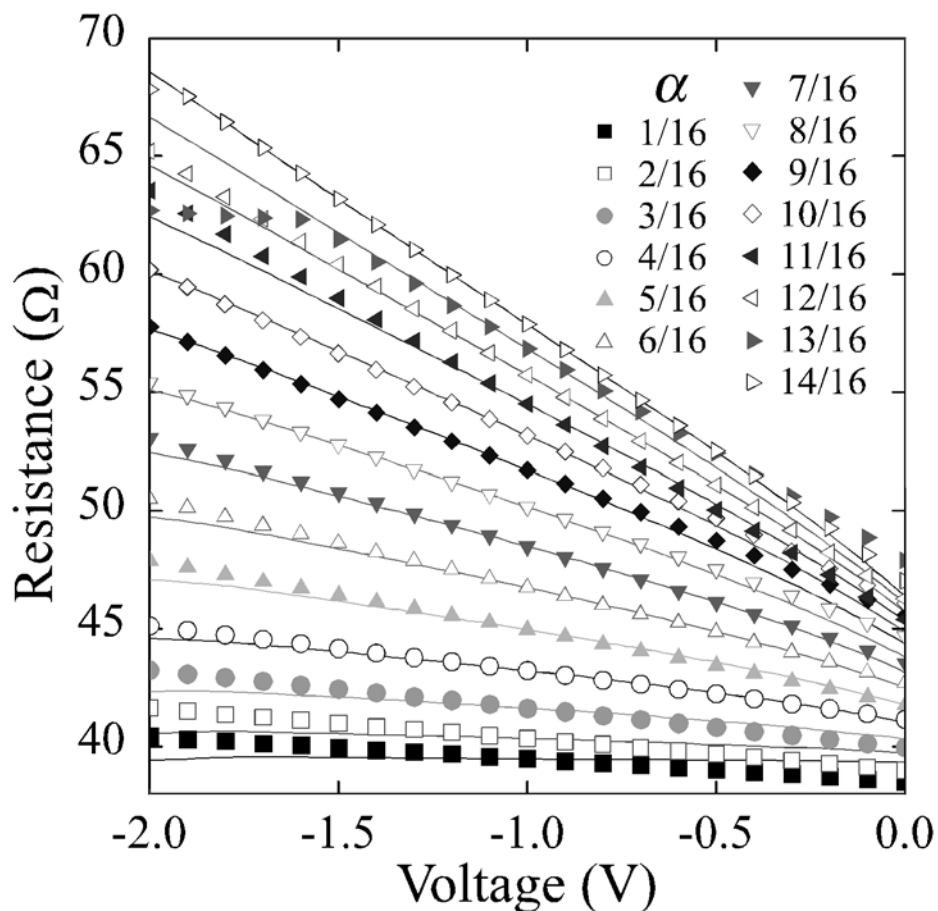


Fig. 8.8 The comparison between the 2-layer model (Eq. 8.13 in the text, solid lines) and experiment for samples with  $r_m = 60\mu\text{m}$  under an extended range of reverse bias. The symbols correspond to the observed resistances adjusted by  $R_c(\alpha)$  with  $[16\alpha, R_c(\alpha)] = (1, 9.285\Omega), \blacksquare; (2, 19.447\Omega), \square; (3, 10553\Omega), \bullet; (4, 68.01\Omega), \circ; (5, 10.002\Omega), \blacktriangle; (6, 13.491\Omega), \triangle; (7, 11.004\Omega), \blacktriangledown; (8, 10.136\Omega), \nabla; (9, 8.588\Omega), \blacklozenge; (10, 4.909\Omega), \diamond; (11, 12.165\Omega), \blacktriangleleft; (12, 6.423\Omega), \triangleleft; (13, 4.356\Omega), \blacktriangleright; (14, 9.38\Omega), \triangleright$ .

### 8.5.3 Theory and Experiment Comparison

Before comparing to the experiment, two approximations in the model need to be addressed. First, the voltage and current probes of an EEC device use surface contacts whereas the model assumes sidewall contacting. Thus, in the experiment, the current flow underneath the metal contact pads 1 and 4 is perpendicular to the mesa surface. And the electrons that reach the bottom layer, i.e., the cylindrical GaAs, must have passed through the top annulus GaAs layer. This non-laminar current flow introduces additional series resistance in the measurement compared to the sidewall-contacting model. Second, the current  $I_{14}$  inside the semiconductor layer has a 3D distribution and electrons from the top layer may take the route under the center inhomogeneity (depletion region) and flow through the bottom layer. In contrast, the model describes in-plane electron flow in parallel with no disruptions between layers.

The above two approximations suggest that the experimentally observed resistance will be consistently larger than the analytical prediction from Eq. 8.14. To account for this discrepancy, an adjustable parameter  $R_C(\alpha)$  is introduced,

$$R'(\alpha, V_B) = R(\alpha, V_B) + R_C(\alpha). \quad (8.17)$$

Here  $R'(\alpha, V_B)$  is the adjusted resistance predicted by the two layer model and  $V_B$  is the direct bias voltage applied across the leads 5 and 4.

For clarity of presentation, Fig. 8.8 compares the theory prediction  $R(\alpha, V_B)$  (Eq. 8.14, solid lines) and adjusted experimental results  $[R_{obs} - R_C(\alpha)]$  (Eqs. 8.7 and 8.17, symbols). The model provides a good fit to the data for various values of  $V_B$  and  $\alpha$ . The

values of  $R_c(\alpha)$  are given in the caption of Fig. 8.8. The quality of this one parameter fitting for  $\alpha$  in the middle range, i.e., from 4/16 to 10/16, is better than those for  $\alpha$  close to 0 or 1. When  $\alpha$  is small, the effect from the high charge density along the metal shunt edge becomes important and impacts the resistance response to the bias voltage. On the other hand, as  $\alpha$  approaches 1, the surface contact pads are so close to the metal shunt, which makes the current path more complicate in the real device than what the model predicts. We have fit the data only in the reverse bias direction with  $-2V < V_B < 0V$ . Under a forward bias, the depletion region is diminished and electrons flow through the MS interface. As electrons get access to the metal shunt, the 2-layer structure is inadequate for modeling the current transport within the MSH.

## 8.6 Comparison between EEC and JFET/MESFET

When a direct reverse bias is applied between leads 5 and 4 with no voltage across the capacitor plates, an EEC device behaves like a JFET [30] or a MESFET [20]. Under this operating mode, the fundamental difference between the two types of device comes from the geometry. In EEC devices, the metal shunt radius varies with the mesa radius fixed and the radius ratio  $\alpha$  changes from 1/16 to 14/16. The 4-lead resistance has a clear dependence on the geometrical parameter  $\alpha$  as shown in Fig. 8.8. In contrast, for most

JFETs and MESFETs, the metal gates have fixed sizes and thus the gate size dependence of the characteristic  $I_D$ - $V_D$  in FETs has never been studied.

Other than the geometry, the EEC effect distinguishes itself from the FETs by the forward field effect, as the JFETs and MESFETs are normally operated under reverse biases. For an EEC device, under a forward electric field, the depletion is thinned and the more thermally excited electrons tunnel through the barrier near the top from semiconductor to metal. The Ti and Au/Ge thin films act as both a Schottky gate and a current shunt. By providing an alternative route for electrons traveling from semiconductor to metal, current paths are not restricted to the conducting channels shaped by the depletion region. This contributes significantly to the geometry dependence of the EEC effect.

## 8.7 Summary

We have successfully designed, fabricated and modeled a new type of electric field sensor. A Van der Pauw disk of homogeneous GaAs with a concentric Au/Ti disk on top is found to exhibit room-temperature electroconductance of 5.2% at an electric field of 2.5kV/cm. With the current testing system, the sensor resolution is 3.05 V/cm. The 2-layer model successfully predicts the linear dependence between the reverse bias voltage and four-lead resistance and fits the measured resistance quite well. In a real life application, EEC sensors may be scaled down to the nano regime and assembled into sensor arrays. By measuring the local electric field intensity at very high spatial resolution, one might construct a charge distribution image on a cell surface in real time.

## **8.8 Acknowledgements**

We thank Dr. L. Ramdas Ram-Mohan for useful discussions. This work is supported by the US National Institute of Health under grant 1U54CA11934201 and by US National Science Foundation under grant ECCS-0725538. SAS is a cofounder of and has a financial interest in PixelEXX, Inc. a start-up company whose mission is to market EXX imaging arrays.

# Bibliography

- [1] R.S. Popovic, Hall Effect Device Adam Hilger, Bristol (1991).
- [2] S.A. Solin, D.R. Hines, T. Thio and J. Heremans, Science 289, 1530 (2000).
- [3] H. Sevincli, M. Topsakal, and S. Ciraci, Phys. Rev. B 78, 245402 (2008).
- [4] Ashkan Behnam, and Ant Ural, Phys. Rev. B 75, 125432 (2007).
- [5] A. Maziewski, V. Zablotskii, and M. Kisielewski, Phys.Rev. B 73, 134415 (2006).
- [6] T. Blomquist, H. Schanze, I. V. Zozoulenko, and H.-J. Stöckmann, Phys. Rev. E 66, 026217 (2002).
- [7] M.N. Baibich, J. M. Boroto, A. Fert F. Nguyen Van Dau F. Petroff. P. Eitenne G. Creuzet A. Friederich and J. Chazels, Phys. Rev. Lett. 61, 2472 (1988).
- [8] W.F. Egelhoﬀ, T. Ha, R.D.K. Misra, Y. Kadmon, J. Nir, C. J. Powell, M.D. Stiles, C.L. Lin, J. M. Sivertsen, J. H. Judy), K. Takano, A. E. Berkowitz, T. C Anthony, and J. A. Brug, J. App. Phys. 78, 273 (1995).
- [9] S. Jin, M. McCormack, T.H. Tiefel and R. Ramesh, J. App. Phys. 76, 6929 (1994).
- [10] S. A. Solin, D.R. Hines, J.S. Tsai, Yu.A. Peshkin, S. J. Chung, N. Goel and M.B. Santos, App. Phys. Lett. 80, 4012 (2002).
- [11] A.C.H. Rowe, D.R. Hines and S.A. Solin, App. Phys. Lett. 83, 1160 (2003).
- [12] A.C.H. Rowe, and S.A. Solin, Phys. Rev. B 71, 235323(2005).
- [13] K.W. Wieland, Yun Wang, L.R. Ram-Mohan, S.A. Solin, and A.M. Girgis, App.



- Phys. Lett. 88, 052105 (2006).
- [14] K.W. Wieland, Yun Wang, S.A. Solin, A.M. Girgis, and L.R. Ram-Mohan, Phys. Rev. B 73, 155305 (2006).
- [15] Yun Wang, A.K.M. Newaz, Jian Wu, S.A. Solin, V.R. Kavasseri, Niu Jin, I.S. Ahmed, and I. Adesida, App.Phys. Lett. 92, 262106 (2008).
- [16] L.J. van der Pauw Philips Res. Rept. 13, 1 (1958).
- [17] Keithley User's Manual Rev. B 5-2, (2005).
- [18] T.-Y. Choi, D. Poulidakos J. Tharian and U. Sennhauser, Nano Lett. 6, 1589 (2006).
- [19] A.G. Baca, and C.I.H. Ashby, Fabrication of GaAs Devices, -(EMIS processing series, Vol.6) Institution of Electrical Engineers (2005).
- [20] S.M. Sze, Physics of Semiconductor Devices, 2nd Ed. Wiley-Interscience (1981).
- [21] W. Schockley, and W.T. Read, Phys. Rev. 87, 835 (1952).
- [22] S. Chand, and J. Kumar, Semi. Sci. Technol. 12, 899 (1997).
- [23] K. Maeda, H. Ikoma, K. Sato, and T. Ishida, App. Phys.Lett. 62, 2560 (1993).
- [24] S.M. Sze, C.R. Crowell, and d. Kahng, J. App. Phys. 35, 2534 (1964).
- [25] P. Chattopadhyay, J. Phys. D 29, 823 (1996).
- [26] J.A. Ellis, and P.A. Barnes, App. Phys. Lett. 76, 124 (2000).
- [27] R.B. Pierret, Semiconductor Device Fundamentals , Addison Wesley; 2nd Ed (1991).
- [28] T. Zhou, S.A. Solin and D.R. Hines, J. Magn. Magn. Mater 226, 1976 (2001).
- [29] C. Wolfe, G. Stillman and J.A. Rossi, Sol. St. Sci. and Tech. 199, 2 (1972)
- [30] G.C. Dacey, and I.M. Ross, Proc. IRE 41, 970 (1953)

# Curriculum Vitae

## Jian Wu

### PERSONAL INFORMATION

*Address:* Department of Physics, Washington University in St Louis  
Campus Box 1105, One Brookings Drive,  
St Louis, MO 63130  
*Email:* [jianwu@physics.wustl.edu](mailto:jianwu@physics.wustl.edu)  
*Phone:* (314)580-9125  
*Nationality:* P. R. China  
*Date of Birth:* Sep. 1984

### EDUCATION

**Washington University in St. Louis (WUSTL), St. Louis, MO** 09/2005-  
*Ph.D. candidate in Physics, GPA 3.99/4.0*  
Advisor: Prof. S. A. Solin

**University of Science and Technology of China (USTC), Hefei, Anhui, P. R. China** 09/2001-07/2005  
*Bachelor of Science, GPA 3.60/4.3*  
Advisor: Prof. Bing Wang

### PROFESSIONAL EXPERIENCE

#### *Research*

- ◆ **Frustrated Magnetism in doped quasi triangular lattice materials ( WUSTL)**
  - Synthesized doped quasi triangular lattice materials  $\text{Cu}_{2(1-x)}\text{Zn}_{2x}(\text{OH})_3\text{NO}_3$  and their organic derivatives  $\text{Cu}_{2(1-x)}\text{Zn}_{2x}(\text{C}_7\text{H}_{15}\text{COO})_m\text{H}_2\text{O}$
  - Investigated the AC/DC susceptibility and structural properties of above materials
  - Designed and integrated a high pressure hydrothermal synthesis system
  - Built an AC susceptibility measurement tool working on PPMS platform
- ◆ **Extraordinary electrical conductance (EEC) devices (WUSTL)**
  - Characterized the Ti -GaAs Schottky Barrier
  - Built a 2-layer analytical model of the EEC effect in Ti-GaAs Metal semiconductor hybrid structure devices
- ◆ **Studied the transport properties of Quantum Dots (USTC, undergraduate)**

#### *Teaching*

- Teaching Assistant for undergraduate level introductory physics and electromagnetism.
- Teaching Assistant for graduate level statistical mechanics.

#### *Others*

- Selected to attend 2008 Boulder Summer School for Condensed Matter and Material Physics
- Attended 2007 Graduate Student Committee for Faculty Search (WUSTL)

### SKILLS

**Lab equipment:** Quantum Design PPMS, Rigaku UltraX18 diffractometer, Rigaku D-MAX diffractometer, Agilent 7500CE ICP-MS

**Languages:** English – Advanced fluency in speaking and writing; Chinese (Mandarin) – Native fluency

**Computer:** C/C++, Labview, Matlab, Mathematica, Origin, MDI Jade, Rietica (X-ray analysis)

### HONORS AND AWARDS

University fellowship and Hughes research fellowship (WUSTL)	2005-2006
Annual excellent undergraduate student scholarship (USTC)	2001-2005
Outstanding freshman fellowship (USTC)	Fall, 2001

### PUBLICATION LIST

- [1] **Jian Wu**, Julia S. Wildeboer, Fletcher Werner, Alexander Seidel, Z. Nussinov, and S. A. Solin, “Frustrated magnetism and Griffiths phases in distorted triangular lattice materials:  $\text{Cu}_{2(1-x)}\text{Zn}_{2x}(\text{OH})_3(\text{C}_7\text{H}_{15}\text{COO})\cdot\text{mH}_2\text{O}$ ,” in preparation for Physical Review.
- [2] **Jian Wu**, Julia S. Wildeboer, Fletcher Werner, Alexander Seidel, Z. Nussinov, and S. A. Solin, “Spin glassiness and power law scaling in anisotropic triangular spin-1/2 antiferromagnets”, submitted for Physical Review Letter.
- [3] **Jian Wu**, A. K. Gangopadhyay, P. Kanjanaboos and S. A. Solin, “Magnetic Properties of  $S = 1/2$  quasi-triangular lattice materials:  $\text{Cu}_{2(1-x)}\text{Zn}_{2x}(\text{OH})_3(\text{C}_7\text{H}_{15}\text{COO})\cdot\text{mH}_2\text{O}$ ,” **J.Phys.:Condens. Matter.** 22, 334211 (2010).
- [4] A. K. M. Newaz, Yun Wang, **Jian Wu**, S. A. Solin, V. R. Kavasseri, I. S. Ahmad, and I. Adesida, “Experimental Measurements and Analytical Modeling of Extraordinary Electroconductance,” **Phys. Rev. B** 79, 195308-1 - 195308-8 (2009).
- [5] Yun Wang, A. K. M. Newaz, **Jian Wu**, S. A. Solin, V. R. Kavasseri, N. Jin, I. S. Ahmed, and I. Adesida, “Extraordinary Electroconductance In Metal-Semiconductor Hybrid Structures,” **Applied Physics Letters** 92, 262106 (2008).
- [6] Yun Wang, A. K. M. Newaz, **Jian Wu**, and S. A. Solin, “Geometry Driven Extraordinary Electroconductance (EEC) in Ti-GaAs Metal-Semiconductor Hybrid Structures,” **Proceedings of the 29th International Conference on the Physics of Semiconductors**, Rio de Janeiro, Brazil, August, 2008, in press.

### CONFERENCES AND PRESENTATIONS

- [1] **Jian Wu**, Fletcher Werner, A. K. Gangopadhyay and S. A. Solin, “Frustrated magnetism in doped quasi-triangular materials:  $\text{Cu}_{2(1-x)}\text{Zn}_{2x}(\text{OH})_3\text{NO}_3/(\text{C}_7\text{H}_{15}\text{COO})\cdot\text{mH}_2\text{O}$ ,” American Physics society (APS) March Meeting 2010, Portland, USA
- [2] **Jian Wu**, A. K. Gangopadhyay and S. A. Solin, “Magnetic properties of a doped quasi-triangular lattice material,  $\text{Cu}_{2(1-x)}\text{Zn}_{2x}(\text{OH})_3\text{NO}_3/(\text{C}_7\text{H}_{15}\text{COO})\cdot\text{mH}_2\text{O}$ ,” APS March Meeting 2009, Pittsburg, USA
- [3] Yun Wang, A. K. M. Newaz, **Jian Wu**, S. A. Solin, V. R. Kavasseri, N. Jin, I. S. Ahmed, and I. Adesida, “Extraordinary Electroconductance in Ti-GaAs hybrid thin film structures,” APS March Meeting 2008, New Orleans, USA